Bioinspired Ceramic Composites:
Enhancing Performance through Hierarchical Structural Design

Ehsan Azad

A Thesis

in

The Department

of

Mechanical, Industrial and Aerospace Engineering

Presented in Partial Fulfillment of the Requirements

for the Degree of

Doctor of Philosophy Mechanical Engineering at

Concordia University

Montreal, Quebec, Canada

September 2025

CONCORDIA UNIVERSITY

School of Graduate Studies

This is to certify that the thesis prepared

By:	Ehsan Azad
Entitled:	Bioinspired Ceramic Composites: Enhancing Performance through Hierarchical Structural Design

and submitted in partial fulfillment of the requirements for the degree of

Doctor Of Philosophy (Mechanical Engineering)

complies with the regulations of the University and meets the accepted standards with respect to originality and quality.

Signed by the final Examining Committee:

Chair	**Dr. Muthukumaran Packirisamy**
External Examiner	**Dr. Gobinda Saha**
External to Program	**Dr. Ahmed Soliman**
Examiner	**Dr. Martin D. Pugh**
Examiner	**Dr. Christian Moreau**
Supervisor	**Dr. Mehdi Hojjati**
Supervisor	**Dr. Farjad Shadmehri**
Chair of Department or Graduate Program Director	**Dr. Ramin Sedaghati**
Dean, Faculty of Engineering and Computer Science	**Dr. Mourad Debbabi**
Date of Defence	**September 19, 2025**

Abstract

Bioinspired Ceramic Composites: Enhancing Performance through Hierarchical Structural Design

Ehsan Azad, Ph.D.

Concordia University, 2025

Ceramics have strong potential for advanced applications because of their high strength and hardness. However, their brittleness and low energy absorption limit broader use. Nature provides useful design strategies to overcome these limitations. Biological armors such as nacre and abalone shells achieve high toughness through hierarchical structures. Inspired by these systems, a programmable laser micromachining platform using ultra-short picosecond pulses was developed to create precise multiscale bioinspired surface architectures on alumina tiles. The laser-engraved tiles were then laminated with Surlyn® to produce bioinspired ceramic composites. Their mechanical behavior, including energy absorption, stiffness, and strength, was systematically evaluated under static and dynamic loading.

Increasing the Surlyn® content promotes plastic deformation while maintaining adhesive failure at the interface. Introducing micro-patterns, similar to those found in natural armors, improves interfacial performance by creating mechanical interlocking and modifying stress distribution. As a result, the failure mode shifts from adhesive to cohesive, increasing interfacial shear strength by 64% and energy absorption by 107%. Additional tests under static and cyclic flexural loading show that laser-engraved macro-patterns and optimized stacking sequences increase energy dissipation by 85%, mainly through crack deflection and localized plastic deformation. Combining hexagonal macro-patterns with diagonal micro-grooves further improves interfacial adhesion and impact resistance, nearly doubling energy absorption and deformation capacity. X-ray radiography confirms reduced delamination and a smaller damage area in the integrated design.

This study combines bioinspired design, advanced materials, and laser-based fabrication to develop ceramic composites with tunable mechanical behavior for applications such as protective equipment, aerospace structures, and biomedical devices.

Acknowledgments

I would like to express my deepest gratitude to my supervisors for their invaluable guidance, support, and encouragement throughout my PhD journey. I am sincerely thankful to Dr. Mehdi Hojjati and Dr. Farjad Shadmehri at Concordia University for their mentorship, constructive feedback, and continuous support that helped shape this work. I am equally grateful to Dr. Behnam Ashrafi and Dr. Hamidreza Yazdani Sarvestani at the National Research Council Canada (NRC-CNRC) for their insightful supervision, technical expertise, and generous support throughout the collaborative phases of this research. Their combined mentorship has been instrumental in the successful completion of this thesis, and I am truly honored to have worked under their guidance.

Financial support from National Research Council Canada (NRC) and Natural Sciences and Engineering Research Council of Canada (NSERC) is gratefully acknowledged.

I am particularly grateful the support of my colleagues and friends Azam, Meisam, Sepanta, Marjan, Mina, Parinaz, Farshad, Hafez, Arsalan, Emad, Ali, Arash, Farid, Farzad, Allyson, and Lorenz throughout this journey.

List of journal papers and conference presentations

Journal Papers

[1] E. Azad, H. Yazdani Sarvestani, B. Ashrafi, F. Shadmehri, and M. Hojjati, From Nature to Engineering: Mortar Volume and Interfacial Mechanics in Bioinspired Ceramics. Available at SSRN 4767755.

[2] E. Azad, H.Y. Sarvestani, B. Ashrafi, F. Shadmehri, and M. Hojjati, From macro to micro: bioinspired designs for tougher ceramics. Journal of Materials Research and Technology. 31 (2024) 3310-3319.

[3] E. Azad, H. Yazdani Sarvestani, B. Ashrafi, F. Shadmehri, and M. Hojjati, Enhancing Ceramic Structural and Interfacial Properties via Micro-Patterning and Macro-Architectural Integration. Advanced Materials Technologies. (2025) 2401439.

[4] E. Azad, H. Yazdani Sarvestani, B. Ashrafi, F. Shadmehri, and M. Hojjati, Bioinspired Programmable Multi-scale Surface Architectures for Toughening Ceramic–Polymer Composites, Material Horizons (under review)

Conference Papers / Presentations

[1] E. Azad, H. Yazdani Sarvestani, B. Ashrafi, F. Shadmehri, and M. Hojjati, Secrets of Nature to Make an Armor, ASM 2022

[2] E. Azad, H. Yazdani Sarvestani, B. Ashrafi, F. Shadmehri, and M. Hojjati, Learning from Nature, ASM 2023

[3] E. Azad, H. Yazdani Sarvestani, B. Ashrafi, F. Shadmehri, and M. Hojjati, Enhancing Bioinspired Ceramics with Nature's Micro-Patterns, CASI 2023

[4] E. Azad, H. Yazdani Sarvestani, B. Ashrafi, F. Shadmehri, and M. Hojjati, Learning from Nature, CREPEC 2024

[5] E. Azad, H. Yazdani Sarvestani, B. Ashrafi, F. Shadmehri, and M. Hojjati, Bioinspired Ceramics: Harnessing Nature's Strategiesfor ImprovingInterfacial Strengthand Energy Absorption, CANCOM 2024

[6] E. Azad, H. Yazdani Sarvestani, B. Ashrafi, F. Shadmehri, and M. Hojjati, Biomimetic Architected Ceramics: Enhancing Interfacial Properties and Energy Absorption through Surlyn-Alumina Composites, ECCM21, 2024

[7] E. Azad, H. Yazdani Sarvestani, B. Ashrafi, F. Shadmehri, and M. Hojjati, mimicking nature: improving ceramic composite performance with micro-patterned interfaces, CSME-CFDSC-CSR 2025

Table of Contents

List of Figures

List of Tables

Chapter 1:

Introduction and Motivations

1.1 Introduction

Ceramics are widely used across industries due to their excellent thermal stability, hardness, and durability. However, their brittleness significantly limits their damage tolerance. While approaches like nanoparticle reinforcement and microstructural tuning have been explored, major gains in toughness and impact resistance remain limited [1–5].

Nature offers valuable inspiration for overcoming ceramic brittleness. Biological materials like fish scales, tooth enamel, and nacre feature microstructures, such as cross-ply, lamellar, and brick-and-mortar arrangements, that improve toughness through mechanisms like crack deflection and bridging. These natural architectures combine high strength, stiffness, and wear resistance, making them suitable for applications like dental implants [6–9].

For instance, nacre toughens through energy dissipation in localized deformation zones, while beetle cuticles use helicoidal fiber arrangements to achieve lightweight, tough structures. Emulating such features in ceramics has led to the development of bioinspired composites with improved mechanical properties. Techniques like freeze-casting, 3D printing, and layer-by-layer assembly have been used to replicate these architectures, though they often struggle with precision and scalability [10–14].

To address these challenges, a programmable manufacturing platform was developed to accurately design and fabricate multiscale, bioinspired ceramic architectures. Precise control over macro- and micro-structural features is allowed by this system, enabling the scalable production of complex geometries. Using this method, laminated ceramic composites with hard and soft interfaces were created, and their mechanical performance was experimentally examined under different patterns and stacking sequences. This strategy enables the design of tough, energy-absorbing ceramics with tailored properties for advanced applications.

1.2 Research Motivations and Objectives

The NRC's Aerospace Manufacturing Technologies Centre (AMTC) has been developing bioinspired architected ceramics to improve mechanical performance [7,10,12,15]. Laser-cut hexagonal tiles combined with Surlyn interlayers show notable enhancements in multi-impact

scenarios, with energy absorption increasing by up to 220% and stiffness by 80% compared to plain ceramics.

Despite these gains, weak interfacial bonding between alumina and the polymer remains a major limitation. Observed delamination, interfacial sliding, and brittle failure under flexural and impact loading indicate poor load transfer and limited plastic deformation at the interface. As a result, the composite is unable to fully leverage the intrinsic ductility and energy-absorbing capability of Surlyn®, significantly reducing the overall toughness and damage tolerance of the system. These interfacial shortcomings not only restrict energy dissipation but also compromise the structural integrity and long-term performance of the composite. However, weak interfacial bonding between alumina and polymers continues to limit plastic deformation capability (Figure 1.1).

Figure 1.1. Weak bonding between Surlyn and Alumina in the bioinspired ceramics developed by AMTC

In the subsequent phase of this study, we build upon prior advancements in bioinspired ceramics developed at AMTC, with a focused investigation into the interfacial properties between alumina tiles and the polymer matrix. Drawing inspiration from the 5% mortar volume fraction observed in nacre, we examine the role of soft-phase volume fraction in enhancing mechanical performance, with particular emphasis on improving the interfacial bonding between alumina and Surlyn. To this end, advanced laser machining techniques are employed to engrave precise

micropatterns onto the surface of alumina tiles. These microstructures are designed to establish mechanical interlocking at the ceramic–polymer interface, thereby emulating the energy dissipation mechanisms characteristic of natural nacre. Complementing this effort, a digital manufacturing platform has been developed, offering high-resolution control over three-dimensional architecture, including micro and macro-scale cell geometry. This programmable tool addresses the limitations of conventional fabrication techniques by enabling the scalable and accurate production of complex, bioinspired ceramic architectures.

Using this platform, we fabricate multilayered ceramic composites comprised of bioinspired hard building blocks supplemented with soft interlayers. The mechanical behavior of these composites, under both static and cyclic loading conditions, is systematically evaluated, considering the presence or absence of macro- and micro-patterns as well as variations in stacking sequence. The overarching goal of this research is to design and manufacture architected ceramics with enhanced energy absorption, improved plastic deformation capacity, and robust interfacial bonding. To achieve this, the following sub-objectives are pursued:

1. Investigating the influence of the soft phase (Surlyn) volume fraction on interfacial properties
2. Fabrication of precise micro-patterns on alumina surfaces using laser micromachining
3. Exploring the impact of various micro-patterns on interfacial properties
4. Selecting the micro-pattern that yields desirable results with minimal impact on the decrease of Alumina strength
5. Investigating the impact of macro-architectures and stacking sequences on failure behavior
6. Integrating micro-patterns and hexagonal tiles to examine their combined effect on the energy absorption of bioinspired ceramics

1.3 Thesis Layout

The present thesis followed the Concordia manuscript-based thesis guidelines, structuring the details of this study into seven chapters as follows:

Chapter 2: Background and a comprehensive review of previous research on natural armors and their influence on the design, fabrication, and mechanical performance of bioinspired ceramic composites.

Chapter 3: This chapter aims to address a significant knowledge gap concerning the influence of the polymer phase on interfacial mechanics in bioinspired ceramic–polymer composites, with particular emphasis on the effect of mortar volume fraction on interfacial sliding behavior. A comprehensive methodology combining experimental characterization and finite element analysis (FEA) is employed to investigate elastic response, plastic deformation, and damage evolution at the ceramic–polymer interface.

Chapter 4: In this chapter, we take a deep look into the microstructure of natural armors and identify the presence of diverse interfacial micro-patterns that contribute to strong and reliable bonding between ceramic and biopolymer phases—an essential feature often overlooked in most bioinspired designs. Our findings reveal that achieving desirable interfacial properties involves more than optimizing the volume fraction of the polymeric adhesive, as discussed in Chapter 3. Building on this insight, we introduce a series of micro-patterns onto alumina tiles using laser micro-machining and evaluate their impact on interfacial mechanical performance. The objective is to determine the optimal micro-pattern that enhances interfacial properties without significantly compromising the structural integrity of the ceramic components. The chapter further explores the synergistic effects of combining micro-patterning with hexagonal macro-architectures, analyzing their influence on the mechanical behavior of bioinspired ceramic composite beams.

Chapter 5: Building on the previous chapter, where optimal micro- and macro-patterns were identified to enhance mechanical performance, this work chapter focuses on the development of nacre-like ceramic–polymer laminates and evaluates their behavior under both static and cyclic loading conditions. The introduction of laser-engraved micro-patterns and hexagonal macro-patterns into ceramic tiles introduces new challenges related to stacking sequence and layer orientation, both of which significantly influence the resulting cell geometry. Accordingly, this chapter includes the fabrication of composite laminates by stacking patterned ceramic tiles with varying cut depths, geometries, and configurations to systematically assess their impact on mechanical performance.

Chapter 6: Drawing from the structural principles of natural hierarchical materials, and integrating the insights gained from previous chapters, this chapter focuses on the development of a programmable material system and manufacturing approach for fabricating multilayered alumina-based ceramic composites with tunable mechanical properties. To enhance interfacial adhesion and

optimize stress distribution, full-depth hexagonal macro-patterns are combined with shallow diagonal micro-grooves. Low-velocity impact tests at 20 J are conducted to investigate initial failure mechanisms, while repeated impacts at 2 J assess progressive damage accumulation and delamination resistance.

Chapter 7: Finally, the conclusions of this research, along with a discussion of potential future work have been presented.

Chapter 2:

Literature Review

2.1 Ceramic material

The development of novel materials is accelerating across a broad range of industries, including aerospace, marine, energy, construction, defense, and biotechnology, in response to the growing demand for materials with superior mechanical performance. Key design objectives in these fields include minimizing weight while maximizing toughness and strength. In this context, ceramics have gained increasing attention due to their unique combination of properties. Ceramics are compounds formed between metallic and non-metallic elements, characterized by predominantly ionic bonds with partial covalent character. The term "ceramic" originates from the Greek word kerameikos, meaning "burnt stuff," which reflects the high-temperature processing required to achieve their desirable properties. These materials typically exhibit low density, high compressive strength, excellent thermal stability, and strong resistance to oxidation and corrosion. Hardness is among the most valued mechanical properties of ceramics. For instance, the hardest known materials such as diamond belong to this group. Common ceramics include oxides, nitrides, and carbides, such as aluminum oxide (Al_2O_3), silicon dioxide (SiO_2), silicon carbide (SiC), and silicon nitride (Si_3N_4).

Alumina (Al_2O_3) is one of the most widely used advanced ceramics due to its exceptional combination of mechanical, thermal, and chemical properties. It exhibits high hardness, excellent wear resistance, and a relatively low density, making it an ideal candidate for structural applications under extreme conditions. Alumina also has outstanding thermal stability, with a melting point above 2000°C, and maintains its strength at elevated temperatures, which is essential for aerospace, defense, and energy applications. In addition, its high electrical insulation and corrosion resistance make it suitable for electronic substrates and biomedical components. The material is available in various purities and microstructures, which can be tailored to specific performance requirements [16].

In this study, alumina was selected over other ceramics such as silicon carbide (SiC) based on a combination of performance characteristics, processing advantages, and alignment with the project's goals. While SiC and other ceramics offer excellent mechanical properties, they are generally more expensive, more difficult to machine, and in some cases less compatible with laser-based micromachining. Alumina, by contrast, is cost-effective, readily available, and has favorable thermal and optical properties that make it suitable for precision laser processing. Its widespread

industrial adoption also provides a robust foundation of existing data, which supports the validation of the bioinspired ceramic structures developed in this research. Therefore, dense, high-purity alumina was chosen as the primary material for this work, offering a balance of performance, processability, and practicality for experimental investigation.

Despite their advantages, ceramics suffer from inherent brittleness and low tensile strength, limiting their structural applications in scenarios where reliability and toughness are essential. To address these limitations, researchers increasingly look to biological systems for inspiration. Natural structural materials often achieve exceptional mechanical performance through hierarchical architectures that balance strength and toughness. For instance, enamel and seashells are ceramic-like biological composites that overcome brittleness by combining hard, stiff building blocks with weak, energy-dissipating interfaces. A closer examination of natural armors, such as those of armadillos, pangolins, nacre, reveals a recurring structural strategy: hard mineral-based blocks are interspersed with a small volume fraction of soft, organic material at the interfaces. This design enables energy dissipation through interfacial mechanisms while preserving structural integrity. Enamel, for example, consists of rigid rods and crystallites embedded in a protein matrix. Although proteins account for only about 1% of the enamel's mass, their removal results in a 40% reduction in fracture toughness, highlighting their critical role in enhancing toughness [17].

Figure 2.1 illustrates a typical force-displacement response comparing a brittle monolithic material with a bioinspired architectured material made from the same base components. In architectured materials, individual blocks undergo minimal deformation; instead, energy dissipation arises from the relative motion of blocks, analogous to grain boundary sliding in polycrystalline metals [9]. This behavior involves a complex interplay of fracture mechanics, contact mechanics, friction, and plastic deformation at interfaces, producing a nonlinear force-displacement response that enhances toughness through controlled energy dissipation.

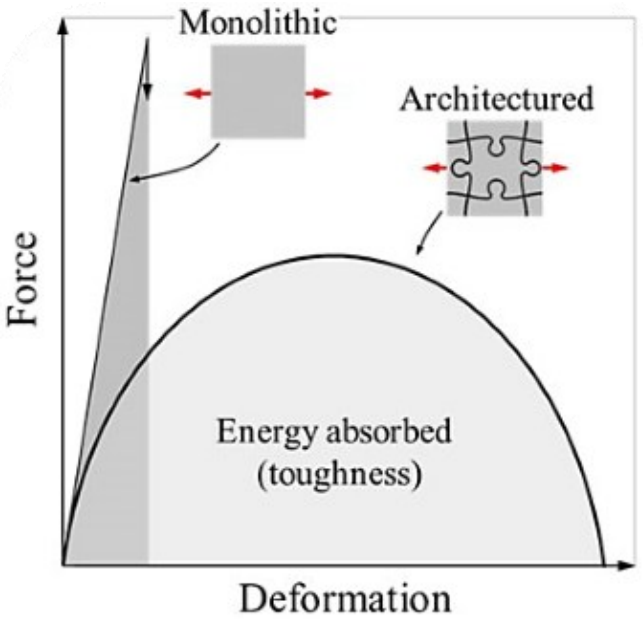

Figure 2.1. Schematic comparison of the force-displacement curve between monolithic and architectured material [9].

2.2 Natural Armors

Nature has a significant advantage over engineering when it comes to the design of architectured materials. Through millions of years of evolution, natural materials have developed highly optimized micro-architectures that result in exceptional structural performance. Remarkably, biological materials such as bone, teeth, and mollusk shells exhibit outstanding mechanical properties despite being composed of relatively weak constituents. These materials can achieve a rare combination of stiffness and toughness, which is difficult to replicate in synthetic systems. The following section highlights examples of natural materials composed of rigid, well-defined building blocks embedded within a softer, more flexible matrix, demonstrating nature's ingenuity in structural design.

2.2.1 Nacre

Nacre, commonly found in the protective shells of mollusks such as oysters, mussels, and abalone, serves as a natural armor. It consists of microscopic, polygonal tablets of aragonite, a common crystalline form of calcium carbonate ($CaCO_3$), typically measuring 5 to 15 µm in diameter and about 0.5 µm in thickness. These tablets are arranged in a three-dimensional brick-

wall structure (Figure 2.2) and are bonded by thin, soft protein interfaces. Also, the tablets contain nano/micro patterns, these patterns significantly enhance the interfacial bonding of the hard ceramic tablets with the soft organic protein layer. The organic interfaces, around 50 nm thick and accounting for roughly 5 percent of the total volume, play a key role in nacre's toughness. While the mineral content provides stiffness and hardness, nacre's ability to absorb significant deformation and energy under external forces is due to tablet sliding along the flexible interfaces. This structural mechanism results in a failure strain nearly twice that of monolithic aragonite [9].

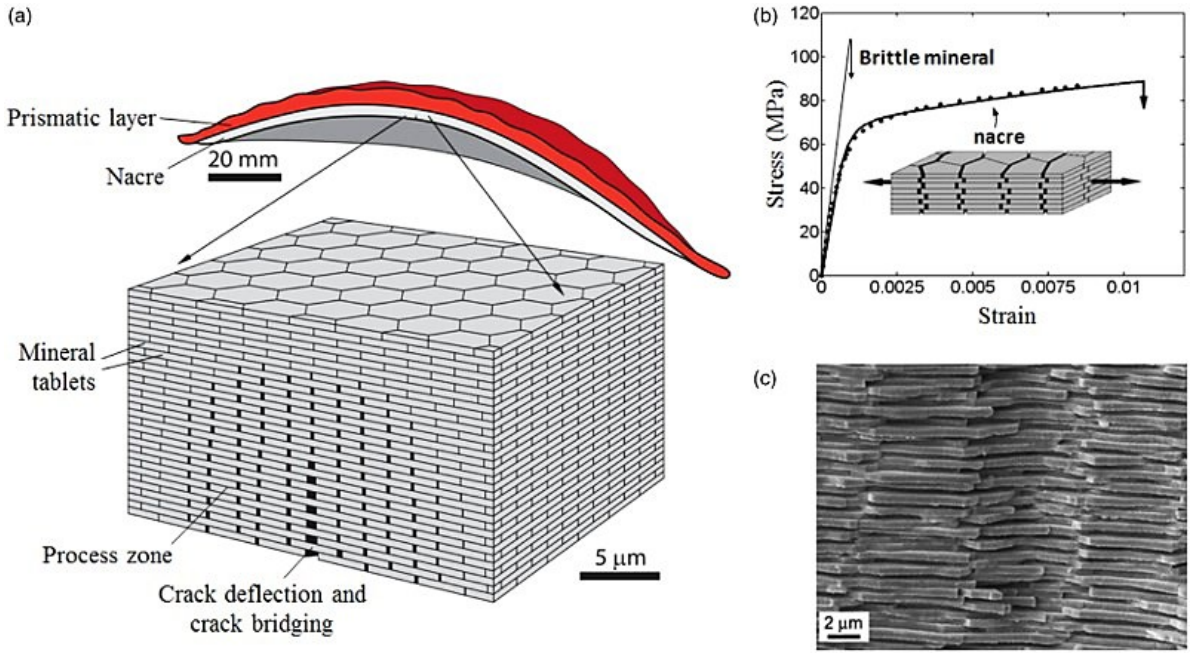

Figure 2.2. (a) The schematic microstructure of nacre; (b) tensile stress-strain curves for nacre and pure aragonite; (c) SEM of a fracture surface in nacre [9].

2.2.2 Conch shell

The conch shell, capable of withstanding the sharp-toothed attacks of predators, is recognized as one of the toughest natural body armors. Its exceptional mechanical performance arises from a three-level hierarchical structure that promotes crack deflection during propagation. As illustrated in Figure 2.3, the conch shell features a lamellar architecture composed of outer (O), middle (M), and inner (I) layers. These layers are made of crisscrossed sheets of calcium carbonate, each separated by thin protein interfaces, with successive sheets oriented perpendicularly to one another. The primary toughening mechanism involves crack deflection along these oriented interfaces,

where the deviation of interfacial channels between layers effectively dissipates mechanical energy. Experimental studies have shown that the work of fracture in conch shells is approximately 1000 times greater than that of their mineral constituents and ten times higher than that of nacre. These remarkable properties make the conch shell an important model for biomimetic design strategies aimed at developing advanced, damage-tolerant materials [18,19].

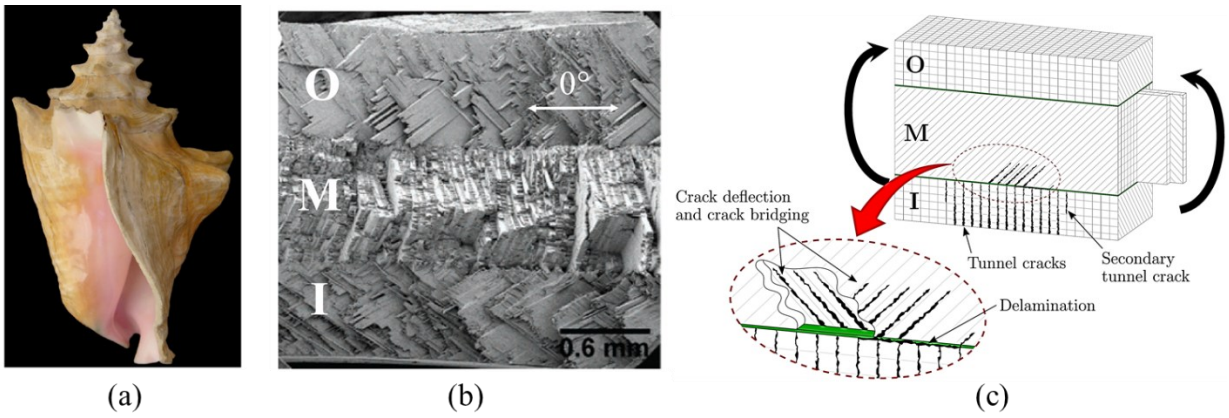

Figure 2.3. (a) Strombus gigas (conch) shell; (b) SEM of a fracture surface of the shell showing a crossed-lamellar microstructure; (c) The main toughening mechanisms [18,19].

2.2.3 Mantis Shrimp

Mantis shrimps are known for their powerful dactyl clubs, which deliver high-velocity strikes during hunting and combat. These clubs can generate forces up to 1,500 N by accelerating at ~10,000g and reaching speeds of 23 m/s, well beyond the tolerance of hard mollusk shells [20]. To withstand such repeated impacts, the dactyl club has evolved a complex multiscale architecture comprising an impact surface, impact region, and periodic region (Figure 2.4). The outer impact surface features a nanoparticulated coating composed of ~65 nm hydroxyapatite particles embedded in an organic matrix, forming a flexible layer that dissipates energy through particle motion and stress redistribution [17,20,21]. This strategy, also seen in other biological materials like chiton teeth, prevents stress concentration and enhances durability under high strain rates (~10^4 s^{-1}) [20]. Despite extensive research, recent discoveries in this region highlight that additional energy absorption mechanisms remain to be uncovered, offering further potential for bioinspired material design. Beneath the surface, the impact region features a herringbone arrangement of ~50 nm mineralized chitin fibers, forming a sinusoidal architecture that facilitates crack deflection and

twisting, thereby enhancing energy dissipation [20,21]. These fibers, aligned with a gradual angular step, create anisotropic properties and induce modulus mismatch at the organic–inorganic interface, guiding crack propagation along weaker paths [22]. Deeper within the club, the periodic region contains a helicoidal arrangement of chitin-protein nanofiber layers. This structure forces propagating cracks to twist along predefined channels in the matrix, significantly increasing fracture resistance while preserving fiber integrity [23]. Together, these hierarchical toughening mechanisms make the mantis shrimp's dactyl club a model system for developing next-generation architectured ceramics.

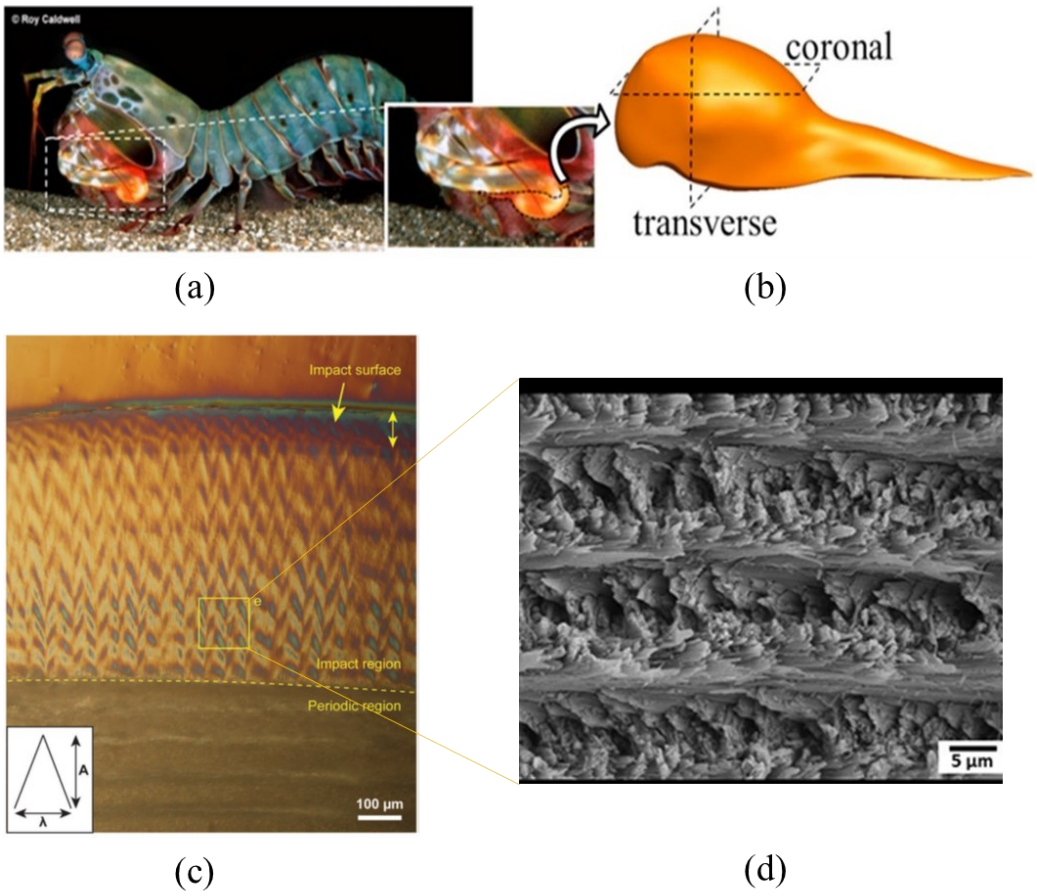

Figure 2.4. (a) Mantis shrimp indicating the dactyl club; (b) 3D rendering from CT scan; (c) transverse section of dactyl club showing impact surface, impact region, and periodic region; (d) SEM of the transverse section of the impact region [23–25].

2.3 Overview of Engineering Approaches to Bioinspiration

A substantial body of research has been devoted to investigating the structure–property relationships in biological materials and the significant challenges associated with their synthetic replication. This section presents an overview of recent advancements in manufacturing techniques for the development of bioinspired materials, followed by an in-depth critical analysis of the laser engraving method as a promising fabrication approach.

2.3.1 Additive Manufacturing

Additive manufacturing (AM) offers a powerful platform for realizing bioinspired designs, enabling the fabrication of complex structures from a wide range of materials. As a rapid and versatile technique, AM allows for the efficient evaluation of different design strategies by highlighting their strengths and limitations within a short development cycle. Unlike traditional subtractive processes, AM builds structures layer by layer, significantly reducing material waste. Common AM techniques include stereolithography (SLA), selective laser sintering (SLS), selective laser melting (SLM), electron beam melting (EBM), laminated object manufacturing (LOM), and fused deposition modeling (FDM) [17].

2.3.2 Magnetically Assisted Additive Manufacturing

Recent advancements have demonstrated the use of this method for fabricating anisotropic composites with tailored properties. By applying ultralow magnetic fields, researchers have achieved controlled three-dimensional orientation and distribution of reinforcing microparticles coated with superparamagnetic nanoparticles. This approach enables the creation of synthetic composites with localized microstructural features that were previously attainable only in naturally grown biological materials [17].

2.3.3 Freeze Casting

Freeze-casting enables the fabrication of unidirectional lamellar scaffolds through ice-templating of aqueous ceramic suspensions, followed by cold pressing to form brick-like structures. These scaffolds are then infiltrated with a compliant polymeric or metallic phase, serving as the "mortar" component. While this technique is capable of producing bulk materials

with bioinspired architectures, it presents limitations in terms of material selection and is generally constrained to ceramic volume fractions below 80% [17].

2.3.4 Lamination

Lamination is a widely used manufacturing technique for producing fiber-reinforced composite materials and has proven effective for implementing various biomimetic designs. Notably, helicoidal lamination sequences inspired by Bouligand architectures have been extensively studied in recent years. These structures have demonstrated improved damage tolerance under through-the-thickness loading, particularly in glass fiber-reinforced composites and, more commonly, carbon fiber-reinforced plastics (CFRPs). The lamination process typically involves fiber lay-up, resin infusion or injection, and subsequent curing [26].

2.3.5 Laser Engraving

The primary design principle behind high-strength, tough natural armor lies in its microstructure, which consists of hard building blocks interconnected by soft interfaces. This concept has inspired the use of laser engraving as a novel technique to introduce controlled surface patterns in ceramics, creating predefined crack paths that guide damage under impact. In this approach, not only are crack trajectories directed along engraved kerfs, but the resulting fragmented ceramic sections can function as discrete building blocks. When these kerfs are filled with a tough polymer, the structure mimics the toughening mechanisms observed in natural armor systems.

Given the central role of lasers in this process, a foundational understanding of laser technology is essential. The term "laser" stands for Light Amplification by Stimulated Emission of Radiation, referring to a coherent, monochromatic beam of electromagnetic radiation that propagates with minimal divergence and can span a wide range of wavelengths and power levels. Lasers are commonly classified based on five main criteria, which are outlined in the following section.

i. Gain medium

A laser medium, also called gain medium describes the material used to generate laser emission (stimulated emission). Lasers are classified into five main types based on their gain medium including Gas laser, Solid-state laser, Fiber laser, Liquid laser (dye laser), and Semiconductor laser (diode laser) [27–31].

ii. Mode of operation

All types of lasers, based on their mode of operation, can be classified into continuous or pulsed wave lasers. Continuous-wave lasers may seem more powerful than pulsed lasers because their advertised laser power is typically much higher, but this can be misleading. This is because lasers are named according to their average laser power, and the average power of pulsed lasers is usually lower even if they reach higher peaks of power. For ceramic micromachining, high energy must be delivered in a very short time to avoid heat accumulation that can cause melting and reduce engraving quality. Pulsed lasers, with their high peak power and ultra-short pulse duration, minimize thermal damage and are therefore ideal for precise, high-quality ceramic processing. [27–31].

iii. Pulse Duration

Pulsed lasers are divided into several categories based on the duration of their pulses. The shorter the pulse, the higher the energy peaks. The most common units used to express pulse duration are Millisecond, Microsecond, Nanosecond, and Picosecond. Picosecond lasers offer the most precise results and have the lowest heat-affected zones which prevent undesirable melting and allow for very precise engravings [27–31].

iv. Wavelength

Wavelength is considered one of the most important properties of an electromagnetic wave including lasers. Lasers can operate in the infrared, near-infrared, visible, ultraviolet, and X-ray spectrums. The first step to start a laser-matter interaction is finding the proper wavelength to process. Because different types of material have different degrees of absorbance in a specific wavelength [27–31].

In all types of laser-based material processing, the interaction time between the laser and the material is a critical parameter that significantly influences the outcome. For pulsed lasers, the total interaction time (T_{pulsed}) is determined by the cumulative duration of individual pulses over the course of the process. In contrast, for continuous-wave (CW) lasers, the interaction time (T_{CW}) is calculated based on the relative speed of the laser spot across the material surface and the size of the laser beam spot [27–31].

$$T_{pulsed} = \text{Pulses number} * \text{Pulse duration} \qquad \text{Equation 2.1}$$

$$T_{CW} = \frac{\text{diameter of laser spot}}{\text{velocity}} \qquad \text{Equation 2.2}$$

The energy delivered by a laser beam per unit time and per unit area is defined as the power density, a key parameter in laser-material interactions. Along with interaction time, power density determines the suitability of a laser for specific processing applications. The relationship between laser power and interaction time defines the operational domain for various laser-based techniques. As illustrated in Figure 2.5, laser material processing methods are generally categorized into three main regimes: heating, melting, and vaporization, each corresponding to distinct power density and interaction time ranges.

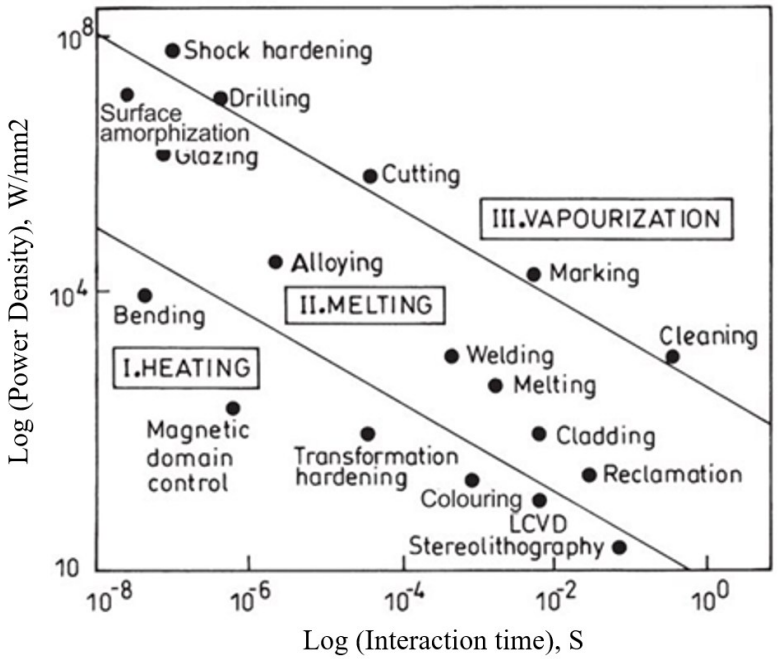

Figure 2.5. laser-assisted Process map [27]

According to the process map for laser-assisted techniques, there is a defined range of power density and interaction time. This provides a general framework for designing laser engraving processes, which fall under the vaporization category. However, processing a specific material requires considering additional parameters, as explained below.

2.3.6 Laser Machining of Alumina Ceramic

Beausoleil et al. [32] conducted a practical investigation of the laser engraving process to achieve high-quality cuts on alumina (Al_2O_3) surfaces. Using ultrafast laser micromachining, they demonstrated deep and precise cuts with reduced manufacturing time. Their optimized laser machining process enabled control over cut depth and improved cut quality in terms of kerf width, kerf taper, surface cleanness, and crack prevention. By adjusting wobble amplitude, number of passes, focal position, and linear speed, they enhanced both material removal rate and cut quality. The experiments were performed on industrial, nonporous 96% alumina tiles with thicknesses of 635 and 1270 μm, a density of 3875 kg/m³, and 0% porosity. The laser used was a Ytterbium picosecond fiber laser with a maximum average power of 50 W, emitting a Gaussian-profile beam with 3 ps, 25 μJ pulses at a wavelength of 1030 nm (near-infrared) and a repetition rate up to 1.83 MHz. Key micromachining parameters included linear speed, power, pulse width, pulse frequency, and wobble. The study also examined the effect of four different wobble patterns on cut quality: line, circle, figure eight, and infinity, as shown in Figure 2.6.

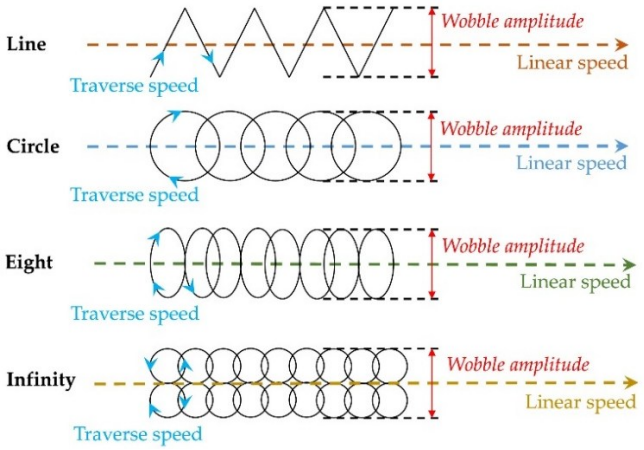

Figure 2.6. Different wobble pattern shapes and their parameters [32].

Their results demonstrated that, along with interaction time and laser power, the wobble pattern and focal position have a significant influence on kerf geometry, surface cleanness, and crack formation. As shown in Figure 2.7, the highlighted region indicates the optimal zone for cutting and material removal, where the focal offset from the reference point yields the best results. The optimal focal position is defined as zero. High-quality cuts, characterized by minimal kerf width and maximum cut depth, were achieved within a focal range of -0.8 mm to 0.5 mm. This

suggests that, for effective engraving of this ceramic material, the distance between the laser head and the material surface must be precisely adjusted within this range, allowing for a maximum tolerance as indicated. Also, Figure 2.8 presents 3D laser scanning microscopy images and surface topography of ceramics machined at various focal positions. In certain cases, prominent signs of melting and an extensive heat-affected zone are clearly visible.

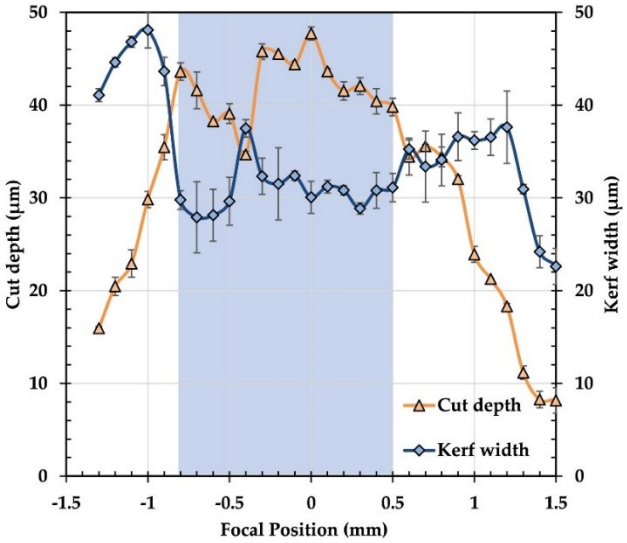

Figure 2.7. The cut depth and kerf width versus focal position after 10 passes with the speed of 1000 mm/s [32].

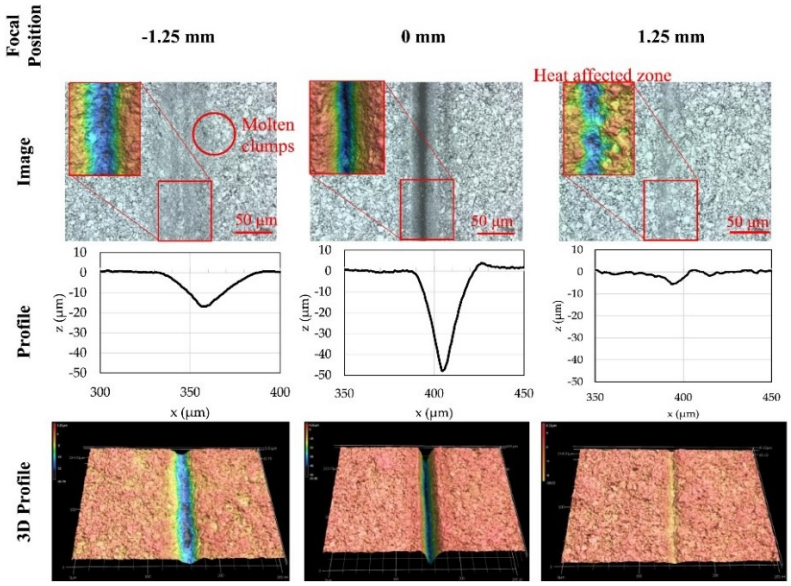

Figure 2.8. 3D laser scanning microscopy images and topography of ceramics for various focal positions [32].

The influence of the wobble pattern is illustrated in Figure 2.9. The line pattern, applied at a speed of 20 mm/s, operates in the melting regime, leading to material resolidification along the kerf edges and resulting in poor cut quality. In contrast, the eight, infinity, and circle patterns produced comparable cut depths with similar quality, showing no evident signs of thermal stress. Among these, the circle pattern was recommended due to its superior surface smoothness [32].

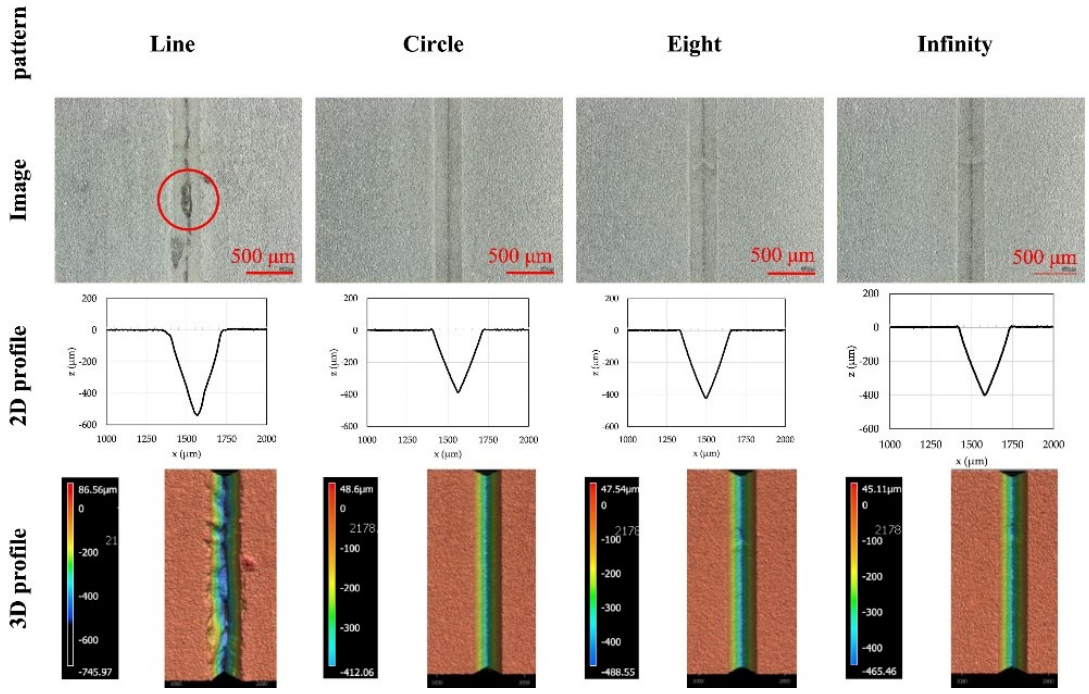

Figure 2.9. 3D laser scanning microscopy topography of ceramics for the linear speed of 20 mm/s [32].

2.3. Concluding Remarks

This chapter provides a foundation for the study by first presenting a literature review on ceramic materials, with particular emphasis on Alumina, which is selected as the primary material in this work due to its widespread industrial use, high thermal stability, and mechanical strength. Following this, the chapter examines some of the most prominent examples of natural armors, focusing on their unique hierarchical structures and damage-resistance mechanisms. These biological systems exhibit remarkable mechanical performance, often attributed to their multiscale architecture and energy dissipation strategies. While the number of such natural armors is extensive and new discoveries are continuously being made, this study focuses on the most up-to-date and practically applicable structural designs that can be translated into engineering solutions for ceramic materials.

The successful implementation of these bioinspired architectures into synthetic ceramics requires more than just conceptual adaptation; it demands an in-depth understanding of and access to advanced manufacturing technologies capable of replicating complex microstructures with precision. As a result, this chapter also surveys the most recent developments in advanced manufacturing processes. Among the investigated techniques, laser engraving was selected for this study due to its high precision, flexibility, and ability to process brittle materials like ceramics with minimal thermal damage when optimized correctly. Therefore, a more detailed investigation is dedicated to laser-based processes, including the fundamental principles of laser-material interaction, types of lasers commonly used in ceramic micromachining, and the key parameters influencing cut quality, material removal rate, and microstructural integrity. Parameters such as power, pulse duration, focal position, scanning speed, and wobble patterns are discussed in depth to establish a robust understanding of how to tailor laser processes for bioinspired applications.

Although this chapter primarily serves as a contextual and technical introduction, it lays the groundwork for the core objective of this research. The translation of natural structural principles into high-performance ceramic systems remains a significant challenge due to the intrinsic brittleness of ceramics and the complexity of biological architectures. In the subsequent chapters, we will present our approach to addressing some of these challenges by integrating nature-inspired design with precision laser micromachining, aiming to contribute novel insights and practical advancements to this evolving field.

Chapter 3:

From Nature to Engineering: Mortar Volume and Interfacial Mechanics in Bioinspired Ceramics

Bioinspired architected ceramics are composite materials that leverage the combined properties of hard ceramic phases and soft polymer components. The interfacial region between these phases plays a critical role in mechanical performance, as effective load transfer depends on strong interfacial bonding. After identifying interfacial bonding as a bottleneck in the structural performance of bioinspired ceramics, we focused on evaluating the effect of increasing the volume fraction of the polymeric adhesive. While most biological systems contain only about 5% of the soft phase (mortar), some studies have shown that a higher adhesive content can enhance interfacial strength in engineered composites. This knowledge gap motivated us to investigate the Impact of Mortar Volume on Interfacial Properties of Bioinspired Ceramics through both experimental and finite element methods.

This work has been published in:

Azad, E., Yazdani Sarvestani, H., Ashrafi, B., Shadmehri, F. and Hojjati, M. (2025), From Nature to Engineering: Mortar Volume and Interfacial Mechanics in Bioinspired Ceramics. Adv. Eng. Mater. 2500297. https://doi.org/10.1002/adem.202500297

3.1 Abstract

Natural armors such as nacre inspire the development of bioinspired ceramics due to their exceptional toughness and damage tolerance. This study examines the influence of mortar volume fraction on the interfacial mechanics of bioinspired ceramic composites using single lap joint (SLJ) specimens with varying soft-layer (mortar) volumes: low mortar volume (LMV, 3%), medium mortar volume (MMV, 6%), and high mortar volume (HMV, 9%). These fractions reflect natural nacre's mortar content and were precisely controlled during specimen fabrication. Experimental results demonstrated adhesive failure as the dominant mode, with increased mortar content enhancing maximum elongation without altering ultimate shear strength. Finite element analysis (FEA) using ABAQUS and a cohesive zone model revealed mortar volume's significant effect on interfacial sliding behavior and strain energy release rate (SERR). Specifically, compared to MMV, LMV exhibited a 5% increase in interfacial stiffness and a 26% reduction in SERR, while HMV showed a 4% stiffness decrease and a 29% increase in SERR. The increased mortar content delayed crack initiation and extended the plastic deformation phase, thereby enhancing energy dissipation capabilities. These findings inform the development of tougher, damage-resistant ceramic composites for engineering by optimizing mortar volume in bioinspired ceramics.

3.2 Introduction

Nature's evolution produces unique architectured materials with superior structural performance honed over millions of years. Biological materials like bone, teeth, and mollusk shells showcase exceptional mechanical properties, despite being composed of seemingly weak constituent elements [6,33,34]. Intriguingly, these biological systems often achieve a unique co-existence of stiffness and toughness, a characteristic synergy that is typically challenging to realize in engineered materials [9,19,35]. Nacre, found in various mollusks, exhibits remarkable mechanical properties due to its brick-and-mortar structure and the role of soft protein interfaces [16,18,34,36]. Similarly, the conch shell's toughness arises from a hierarchical three-layer structure and crack deflection across oriented interfaces [37,38]. The soft interfaces in nacre and conch shells enhance their mechanical properties, providing remarkable stiffness, hardness, energy absorption,

and damage tolerance. These natural structures are inspiring biomimetic models for creating tougher synthetic materials [17,37,39].

In various industries, the demand for superior mechanical properties has led to the development of novel materials, with ceramics becoming popular due to their desirable traits like hardness, low density, high compressive strength, thermal stability, and resistance to oxidation and corrosion [40]. Ceramics, compounds between metallic and nonmetallic elements, exhibit exceptional hardness, with the diamond being a prominent example. Common ceramic materials include alumina, silica, silicon carbide, and silicon nitride [41]. Drawing from the resilience of natural materials, novel strategies have been developed to enhance the toughness of inherently brittle ceramics, mitigating their brittle fracture behavior [25,42–45]. Bio-inspired architectured materials draw inspiration from the use of weak interfaces in ancient lamellar armors and constructions, marking a notable advancement in material design by combining strength and toughness [46–50]. This approach also mimics natural armors such as fish scales and shark skeletons, allowing for the activation of energy dissipative mechanisms like crack deflection, sliding friction, and delamination, thereby further enhancing toughness [12,51–54]. These bioinspired approaches offer the potential to design ceramic-based materials with adjustable thermo-mechanical properties, including strength, stiffness, toughness, and thermal properties [11,14,55–59].

Extensive research has confirmed the crucial role of interfacial interaction between ceramic tiles in facilitating enhanced energy dissipation and damage tolerance in bioinspired ceramics [60–62]. This mechanism is particularly prominent during the initial phase of damage, where load transmission between the tiles occurs through shear forces at the interfacial boundaries, supported by a compliant 'mortar' matrix that accommodates elastic deformation [63]. As the external load intensifies, the mortar undergoes plastic deformation, marking the initiation of damage and leading to significant energy dissipation [13,56]. Several studies have examined the sliding mechanism and key parameters, such as mortar material properties and tablet aspect ratio, to optimize the modulus, strength, and toughness of bio-inspired materials [64,65]. Additionally, modifying the mortar material has shown potential for further enhancing the mechanical properties of these materials [63,66].

The role of a soft component as a mortar in natural armors has been substantiated, particularly when its volume fraction is a minor proportion of the overall structure [67]. Predominantly

composed of minerals, these shells account for at least 95% of their total volume, with organic materials comprising a minor fraction of no more than 5% [68]. Eliminating the organic soft component from nacre enhances its strength but significantly diminishes its toughness. Similar to natural nacre, studies have shown that increasing the mortar volume fraction in nacreous structured materials made through freeze casting leads to increased energy absorption, even though strength decreases [13]. While previous computational studies have examined the mechanical behavior of bioinspired composites by analyzing how the properties and arrangement of constituent phases (e.g., "bricks" and "mortar") influence stiffness, strength, and energy absorption [69,70], there remains a need for a deeper understanding of the interfacial behavior between these phases. Specifically, the role of mortar volume in governing energy dissipation mechanisms and its impact on interfacial properties has not been thoroughly explored. Investigating these relationships is key to uncovering nature's strategies for optimizing the balance between stiffness, strength, and toughness in bioinspired materials.

This study investigates the sliding mechanisms at bioinspired ceramic composite interfaces, which play a critical role in energy absorption. Both experimental analyses and finite element analysis (FEA) are employed to assess elastic, plastic, and damage progression at the interface. To explore the effect of mortar volume fraction, single lap joint (SLJ) specimens with varying mortar volumes- low (3% vol.), medium (6% vol.), and high (9% vol.)- were fabricated. The damage progression of these specimens was meticulously analyzed, and a model was developed that showed excellent agreement with experimental results. Additionally, a 3D ABAQUS model was used to simulate reaction force and damage dissipation energy (DDE), providing valuable insights into the behavior of the interface across different mortar volume fractions.

3.3 Materials and Methods

3.3.1 Material and sample preparation

In order to mimic the sliding mechanisms of ceramic composites, square ceramic tiles (high-tolerance nonporous alumina ceramic with 96-99.8% material composition, 3875 kg/m³ density, and fired fabrication, McMaster-Carr, No. 8462 K45) with 1.5 mm thickness were used as the hard component. The Surlyn thermoplastic, which has been reported to exhibit similarities to biopolymers, was used as a soft polymer interface between the ceramic tiles. Additionally, due to

the brittle nature of the ceramic tiles, which makes them unable to withstand the compression load from the tension machine fixture during tightening, a glass fiber composite sheet (ultra-high-temperature impact-resistant Garolite sheet, McMaster-Carr No. 3909N22) was utilized as structural support for the ceramic tiles and as end tabs for the SLJ specimens. This ensured that the ceramic tiles would be adequately supported during testing and prevented premature failure due to compression loading.

Ceramic panels were fabricated by laminating ceramic tiles, a Surlyn interlayer, and composite sheets together using a vacuum bag technique (see Figure 3.1d). The resulting panels were subjected to a 5-hour heat treatment at 146 °C to ensure proper bonding between the materials. To evaluate the interfacial mechanical properties of the ceramic panel, the panel was cut into four bars using a diamond saw to fabricate single lap joint (SLJ) specimens (see Figure 3.1). This process allowed for the creation of individual test specimens that could be used to examine the mechanical behavior of the brick-and-mortar interface.

To systematically investigate the effect of mortar content variations, three distinct mortar volume fractions were selected:

- LMV (3%) – Represents a lower-than-natural mortar fraction to evaluate the effects of reduced interfacial plasticity.
- MMV (6%) – Chosen as a benchmark reference, slightly exceeding the 5% natural composition of nacre.
- HMV (9%) – Extends beyond the natural range to assess the influence of increased mortar content on interfacial strength and energy dissipation.

These values were selected to provide a controlled deviation from the natural benchmark (5%), enabling a detailed analysis of how changes in mortar fraction affect interfacial mechanics, damage evolution, and crack propagation in bioinspired ceramics.

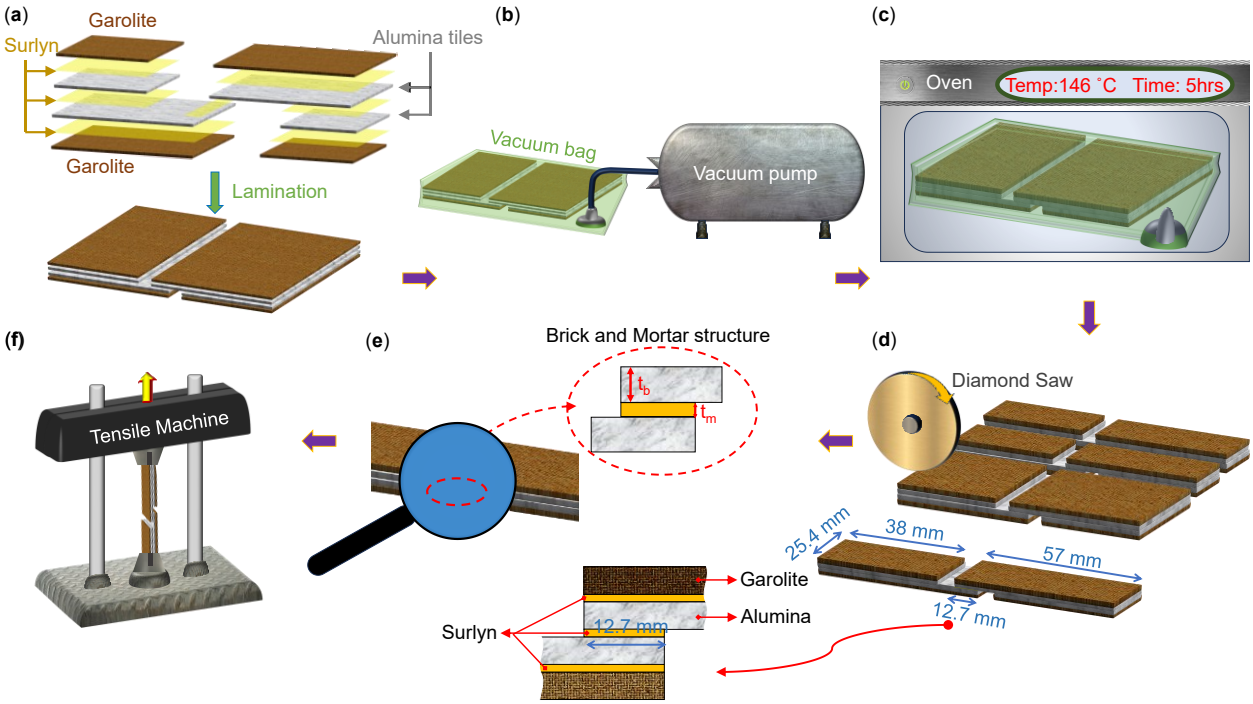

Figure 3.1. Experimental process for creating single lap joint (SLJ) specimens: (**a**) Lamination of ceramic panels with Surlyn interlayers, (**b**) Placement in vacuum bag for consolidation, (**c**) Curing in oven for material bonding, (**d**) Cutting with diamond saw to produce SLJ specimens, along with a 2D Schematic of SLJ specimens, (**e**) Measurement of specimen dimensions, and (**f**) Tensile testing using MTS machine to evaluate mechanical properties.

3.3.2 Single lap joint test

Following the fabrication process, microscopic inspection (see Figure 3.2) was employed to precisely determine the thickness of the Surlyn and alumina layers, ensuring the accurate proportion of brick-and-mortar components. Subsequently, the quasi-static loading tests were performed on SLJ specimens. The SLJ setup configuration and boundary conditions were designed as illustrated in Figure 3.2d. All tests were conducted using the MTS universal machine, following ASTM D3165 guideline, with a loading velocity of 1.27 mm/min [71].

3.3.3 Finite element analysis (FEA)

To analyze the load-displacement behavior and study the sliding mechanisms at the bioinspired interface in SLJ specimens, the FEA package ABAQUS was employed to investigate the effect of

mortar volume fraction on damage evolution. It has been established that 3D finite element models provide more accurate stress distribution predictions compared to simplified 2D approaches [72–75]. As a result, three SLJ specimen types (LMV, MMV, HMV) were simulated using detailed 3D models. The models' boundary conditions are shown in Figure 3.3a, where one end of the joint was fully constrained, while the other end was allowed to move solely in the axial direction, enabling tensile loading under displacement control. Importantly, FEA results demonstrated that shear stress and strain at the Garolite-alumina interface were minimal compared to the overlap region, where the bioinspired interface was located. This confirms that the Garolite sheet functioned primarily as a structural support and did not significantly affect interfacial behavior or the measured mechanical properties of the SLJ specimens. Furthermore, experimental observations verified that no failure or delamination occurred at the Garolite-alumina interface, further corroborating the FEA predictions and ensuring the accuracy of the numerical model. To achieve strong agreement between experimental and numerical results, the force-displacement behavior from SLJ tests was used to calibrate the Cohesive Zone Model (CZM) parameters. The cohesive element was specifically implemented at the alumina-mortar interface, ensuring an accurate representation of interfacial mechanics, energy dissipation, and failure behavior.

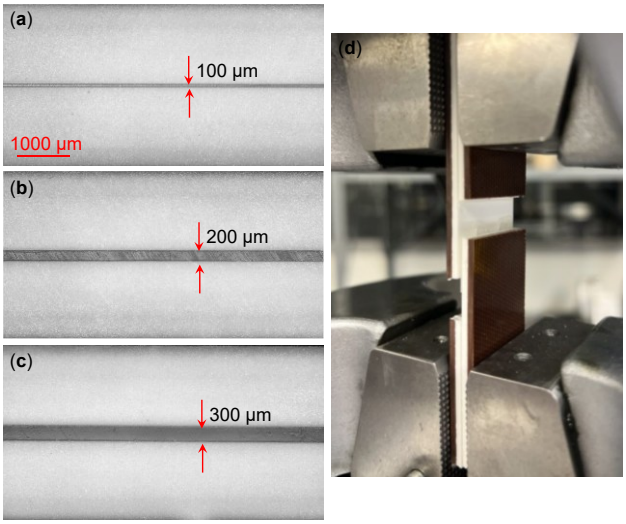

Figure 3.2. The microscopic images showing brick and mortar ratio of (**a**) Low mortar volume (LMV) with Surlyn thickness of 100 µm, (**b**) Medium mortar volume (MMV) with Surlyn thickness of 200 µm, (**c**) High mortar volume (HMV) with Surlyn thickness of 300 µm, and (**d**) Configuration and boundary condition of SLJ test.

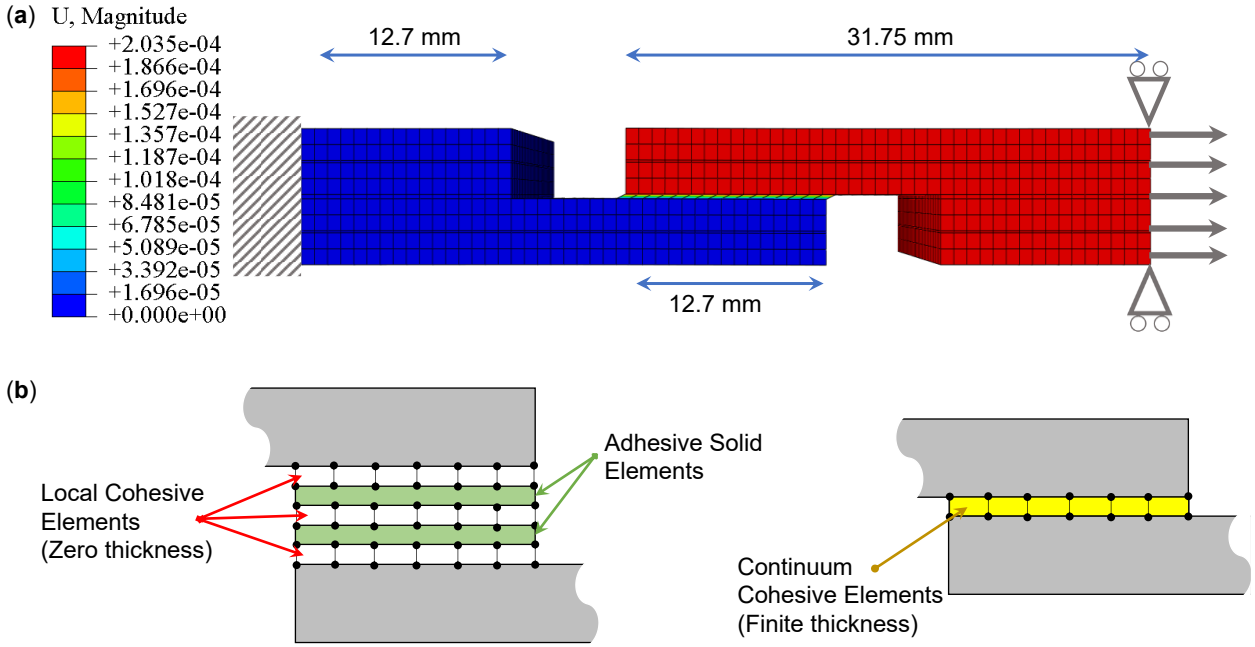

Figure 3.3. (a) 3D Model and boundary conditions used for single lap joint (SLJ) test, and (b) Schematics of local and continuum Cohesive Zone Modeling (CZM) methods.

The adherents' mesh is comprised of reduced integration eight-node linear brick element (C3D8R), while the adhesive's mesh is made up of a single layer of eight node three dimensional cohesive elements (COH3D8) that are compatible with C3D8R. One of the key benefits of using CZM over other FE methods is that its strength prediction is not affected by the size and quantity of the mesh used [69]. This is due to the damage growth being defined over an area, instead of taking values from a single point. CZM provides a robust framework for simulating failure mechanisms by incorporating an intrinsic length scale through the cohesive law, thereby ensuring size-independent strength predictions. Unlike classical FE approaches, which can exhibit mesh sensitivity and stress singularities, CZM allows for a more consistent and physically realistic representation of damage and crack propagation.

There are two distinct approaches to CZM: the local approach and the continuum approach. When dealing with adhesive joints, the local approach employs cohesive elements to link stacked nodes of elements, creating a zero-thickness interface. Meanwhile, in the continuum approach which is, cohesive elements simulate the entire adhesive bond, which has a finite thickness, linking the two adherents. The contrasts between these two methods are shown in Figure 3b. In the local approach, cohesive elements only simulate damage growth between the connected elements, with the plastic properties of the adhesive modeled using solid finite elements. In contrast, in the

continuum approach, the stiffness of CZM elements represents the adhesive layer stiffness in each mode of loading [76]. The critical parameters of the cohesive law, such as critical strain energy release rate (G_{Ic} or G_{IIc}), cohesive strength, and cohesive stiffness, play a crucial role in the simulation and prediction of damage initiation and progression in CZM. A variety of cohesive laws, including triangular, linear-parabolic, polynomial, exponential, and trapezoidal shapes can be utilized to determine the properties of the cohesive element, with a traction separation law being employed for this purpose within CZM [76].

The double cantilever beam (DCB) and end-notched flexure (ENF) tests are widely used to determine the energy release rate (ERR) in mode I and II for both adhesive bonds and laminate delamination [72]. While some of these methods have been standardized and data reduction techniques for extracting ERR have been published, they have a significant limitation in their inability to handle the bending moment created in adherents during testing. Specifically, they cannot be utilized for brittle adherents with insufficient flexural strength, such as most ceramics and glasses. To address this, the current study employed force and displacement data obtained from the SLJ test to define the mechanical properties of cohesive elements. Based on the high stiffness and brittleness of the ceramic relative to Surlyn, all elongation of SLJ samples during the test was considered as the displacement of Surlyn. The displacement data obtained from the tension machine was thus utilized as the displacement of the cohesive element in the simulation. However, to determine the material properties of the cohesive elements, it was essential to establish traction with respect to displacement. To accomplish this, another assumption was needed, whereby the average shear stress (Equation 3.1) was assumed to be a good representative of shear traction in the interface, despite the non-constant distribution of shearing stress and exitance of normal stress in the edges of SLJ specimens [72]:

$$\tau = \frac{F}{A} \qquad \text{Equation 3.1}$$

Equation 3.1 defines the average shear stress in the interface (τ) as the shear traction, where F is the force measured during the SLJ test and A is the area of the interface, which is equal to 12.7×25.4 mm². Building on the insights from previous studies on interface failure criteria, this work utilizes the Quadratic Nominal Stress Criterion (QUADS) to model damage initiation [73]:

$$\left(\frac{T_n}{T_n^0}\right)^2 + \left(\frac{T_s}{T_s^0}\right)^2 + \left(\frac{T_t}{T_t^0}\right)^2 = 1 \qquad \text{Equation 3.2}$$

where T_n represents the normal traction in mode I, T_s and T_t represent shearing and tearing tractions in mode II and III respectively. T_n^0, T_s^0, and T_t^0 denote their corresponding maximum values. While numerous studies have successfully captured the peak failure load through various damage initiation and evolution criteria, accurately simulating the entire damage progression remains a key challenge for advancing CZM. The main cause of the difference between experimental results and model predictions was believed to be plastic deformations in the thermoplastic interlayer. Morais [73] with suggestion of the tetra-linear traction-separation law tried to model the hardening phenomenon related to high plastic deformation in the interlayer of carbon epoxy composite before the crack initiation. While promising, the approach requires a more complex parametric study to match experimental delamination data. This can lead to increased complexity and computational costs.

This section describes a methodology for developing the cohesive law of a given material system and test configuration. The approach involves utilizing the force-displacement graph obtained from an experiment to define the damage variable as a function of relative displacement beyond the linear region of the graph where plasticity and damage begin. Specifically, the force-displacement graph obtained from the SLJ test is used to derive the traction-separation graph, which is subsequently utilized to determine the damage variable parameter (D) for simulating the propagation of damage in the interface:

$$\mathrm{D} = 1 - \frac{\mathrm{T}}{\mathrm{K}.\delta} \qquad \text{Equation 3.3}$$

where T represents the traction, which in the case of the SLJ test, is equivalent to the average shear stress calculated using Eq. 1. The K denotes the bonding's stiffness, determined by the slope of the linear portion of the traction-separation graph. The δ represents the displacement beyond the linear region of the graph. According to this fact that no failure was seen in the alumina and Garolite, only their elastic properties shown in Table 3.1 have been used in the FE simulation. The Garolite sheet was utilized as a support for the Alumina tiles and served as the end tab for the SLJ specimens. As the simulation results show, the shear stress or strain at the Garolite-alumina interface is minimal compared to that in the overlap area (see Figure 3.3a). Therefore, in the simulations, the

properties of the Surlyn interlayer were applied as a cohesive element between the alumina and Garolite.

Table 3.1. Material properties including Young's modulus, Poisson's ratio, shear strength, and stiffness used in FEA.

Alumina ceramic (Solid element)	**Surlyn interlayer (Cohesive element)**	**Garolite G-14 (Solid element)**
Young's Modulus = 303 GPa Poisson's ratio = 0.21	Stiffness (K) = 83 MPa/mm Normal strength = 10 MPa Shear strength = 5 MPa	Young's Modulus = 13 GPa Poisson's ratio: 0.35

3.4 Results and Discussion

3.4.1 Experimental study

The average force-displacement curves for all three types of specimens are presented in Figure 3.4Figure 3.4. (a) Experimental force-displacement curves for LMV, MMV, and HMV specimens under single lap joint (SLJ) test, and (b) Image of the SLJ specimen interface after the test, indicating an adhesive failure mode.a. We found that the ultimate force for all three types of specimens was identical. However, an increase in the volume fraction of Surlyn resulted in a significant increase in the maximum elongation exhibited by the ceramic panels. Figure 4a demonstrates a linear elastic segment (yellow zone) for all specimens, implying a limited impact of soft component volume fraction on initial interfacial shear stiffness. Stiffness increases slightly with decreasing soft component volume fraction: LMV exhibits about a 5% increase over MMV, while HMV shows a nearly 4% decrease compared to LMV. Beyond 0.06 mm, plasticity occurs, resulting in hardening and an ultimate force of approximately 2.5 kN for all specimens (shaded zones). However, the maximum displacements during the hardening phase differ, indicating the influence of the mortar volume fraction on plastic deformation in the interface. The LMV specimen exhibits hardening behavior until about 0.3 mm, while the MMV and HMV specimens reach plateaus near 0.4 mm and 0.5 mm, respectively, suggesting delayed crack initiation with higher mortar volume fractions. The variation in mortar volume also plays a critical role in crack propagation behavior. In the LMV specimen, the reduced interfacial plasticity results in earlier crack initiation and faster crack propagation due to the limited energy dissipation capability at the

interface. As the mortar volume increases, the interface becomes more capable of sustaining plastic deformation, leading to a delay in crack initiation and a more gradual crack propagation process. In the HMV specimen, this effect is most pronounced, where the increased plastic deformation at the interface contributes to energy absorption before complete separation, effectively slowing down crack progression. However, accurately pinpointing the precise point at which maximum elongation occurs before the initiation of softening necessitates a comprehensive and meticulous investigation. In this regard, leveraging FEA can offer invaluable insights and a deeper understanding of the underlying mechanisms governing the observed behavior. Furthermore, the presence of a higher mortar volume fraction at the interface of ceramics leads to significant changes in the softening behavior and increased maximum elongation until complete separation, highlighting the strong dependence of damage evolution on the volume fraction of the soft component. This delay in damage propagation contributes to enhanced energy absorption until failure occurs. Upon examining the interface surface of the ceramics post-separation, it was discovered that the failure mode was adhesive, and this remained consistent regardless of the volume fraction of Surlyn (see Figure 3.4b). This phenomenon highlights that the weak point in the interface of the ceramics studied in this work is in the bonding between Surlyn and ceramic. The damage was initiated and propagated in the bonding surface between Surlyn and ceramic. As a result, the ultimate shear strength in the interface remained constant, regardless of the volume fraction of Surlyn.

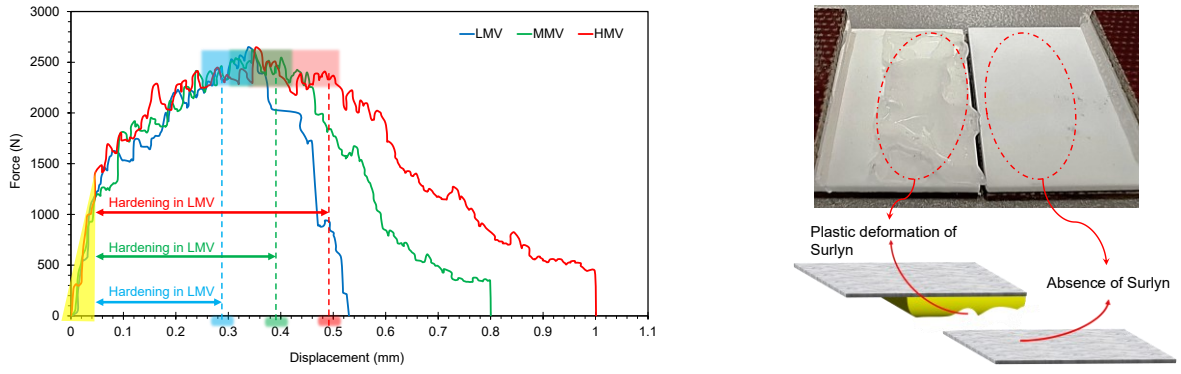

(a) (b)

Figure 3.4. (a) Experimental force-displacement curves for LMV, MMV, and HMV specimens under single lap joint (SLJ) test, and (b) Image of the SLJ specimen interface after the test, indicating an adhesive failure mode.

3.4.2 Finite element study

The key parameters under investigation include interfacial stiffness, shear strength, maximum displacement, hardening and softening behavior, and DDE. Figure 3.5a presents a comparison between finite element method (FEM) results and experimental (EXP) load-displacement curves, demonstrating a strong correlation between them. This close agreement validates the accuracy of the simulation approach and confirms the reliability of the underlying assumptions used in the model. Consequently, this robust FEA framework provides deeper insights into the effect of soft constituent volume fraction on the interfacial mechanics of bioinspired ceramics. In this context, DDE offers a valuable means of understanding interfacial failure mechanisms by quantifying the relationship between damage accumulation and displacement. DDE is calculated as the area enclosed by the irreversible portion of the force-displacement curve. Figure 3.5b reveals distinct trends in DDE evolution across different deformation zones. In the elastic zone, DDE remains at zero, indicating the absence of damage in the bonding region. As plastic deformation progresses in the hardening zone, DDE gradually increases, reflecting the energy dissipated due to plastic deformation. However, beyond the peak force, DDE exhibits a sharp rise, indicating the significant contribution of crack propagation mechanisms alongside plasticity in the subsequent failure stages. To experimentally extract these interfacial mechanical properties, interfacial stiffness was determined from the initial slope of the experimental force-displacement curve, while shear strength was calculated as the peak force divided by the bonded area. Maximum elongation was directly measured from the recorded displacement at failure in SLJ tests. Given the high stiffness and brittleness of the ceramic compared to Surlyn, all observed elongation in SLJ specimens was attributed to Surlyn's deformation, rather than the ceramic components. The force-displacement graph (see Figure 3.5a) highlights an initial linear elastic region, reflecting the variation in interfacial shear stiffness across different mortar volume fractions. The LMV specimen exhibits the highest stiffness, followed by MMV, while HMV shows the lowest stiffness. This trend aligns with the hypothesis that higher mortar volume fractions reduce interfacial stiffness while increasing plastic deformation capacity. Beyond this linear elastic region, plastic deformation initiates, leading to a hardening phase. The force-displacement curves for all three specimens show similar peak force values, which can be attributed to the consistent adhesive failure mechanism observed in experiments. However, the key difference arises in the softening phase, where variations in mortar volume significantly influence maximum displacement and energy dissipation. To further

validate these experimental findings, FEA results confirmed that shear stress and strain at the Garolite-alumina interface were negligible, reinforcing that the experimental response is primarily dictated by the bioinspired interface rather than external constraints. The FEA model was calibrated using force-displacement data from SLJ tests, ensuring that the cohesive parameters used in the simulation accurately captured the experimental interfacial behavior. Since shear stress distribution is non-uniform, an assumption was made that average shear stress serves as a representative measure of shear traction at the interface. The strong agreement between experimental and FEA force-displacement curves (see Figure 3.5a) verifies the accuracy of the extracted mechanical properties and demonstrates that the FEA model effectively captures the interfacial mechanics of bioinspired ceramics.

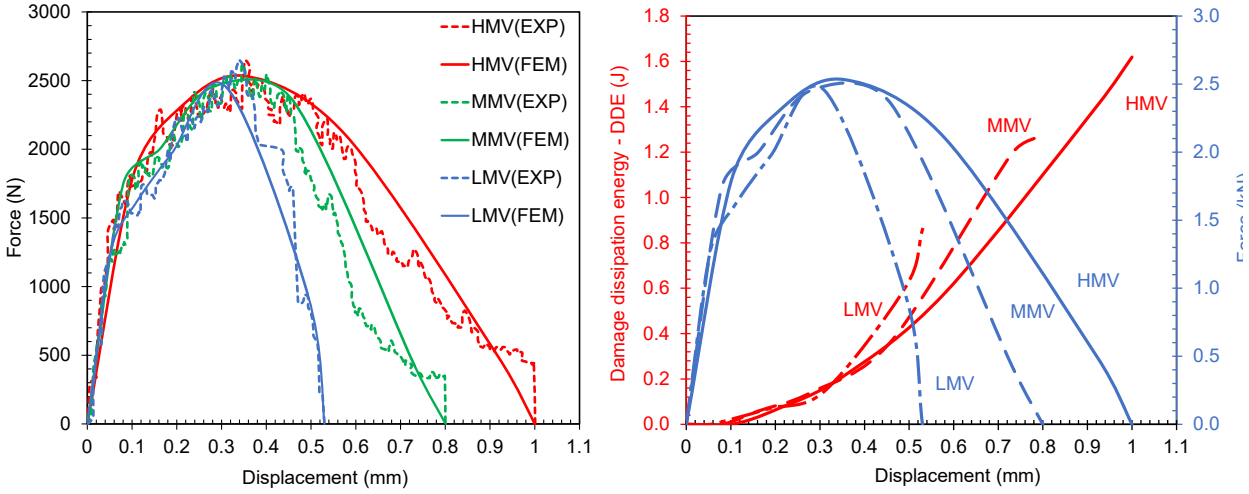

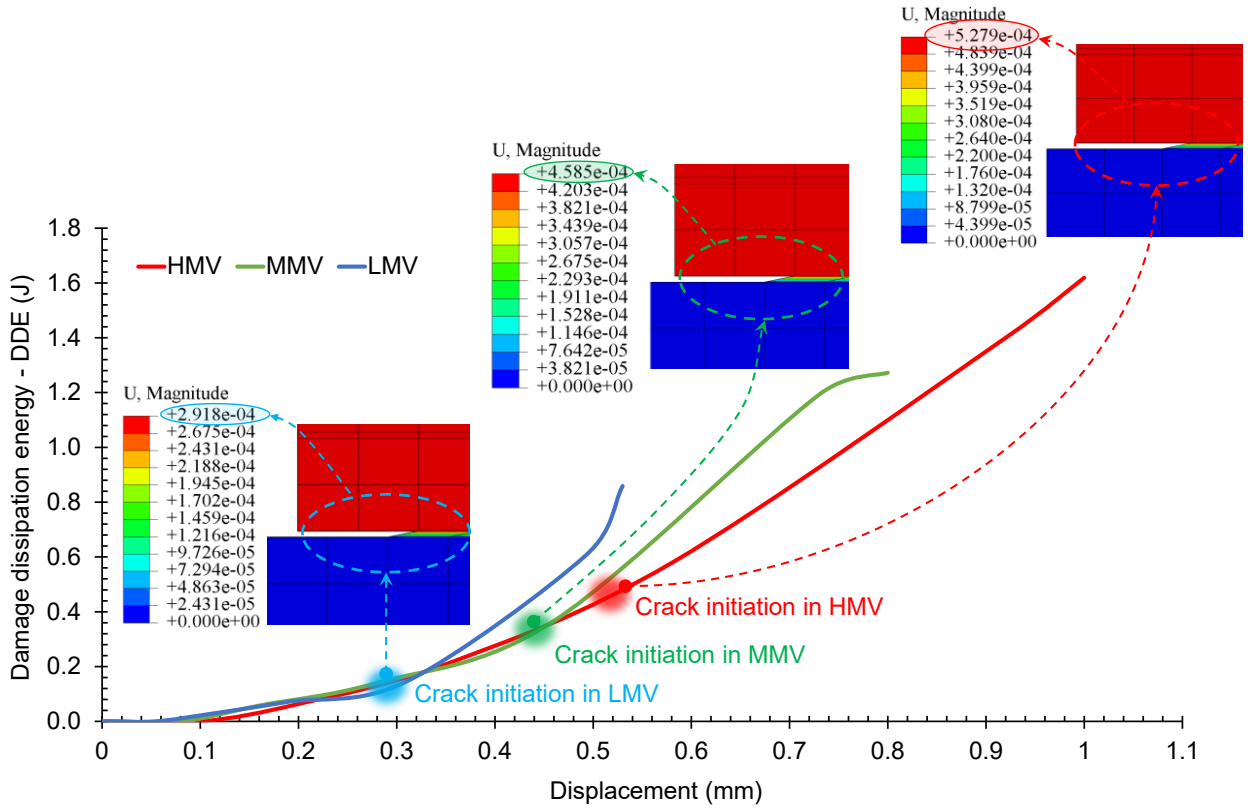

(**c**)

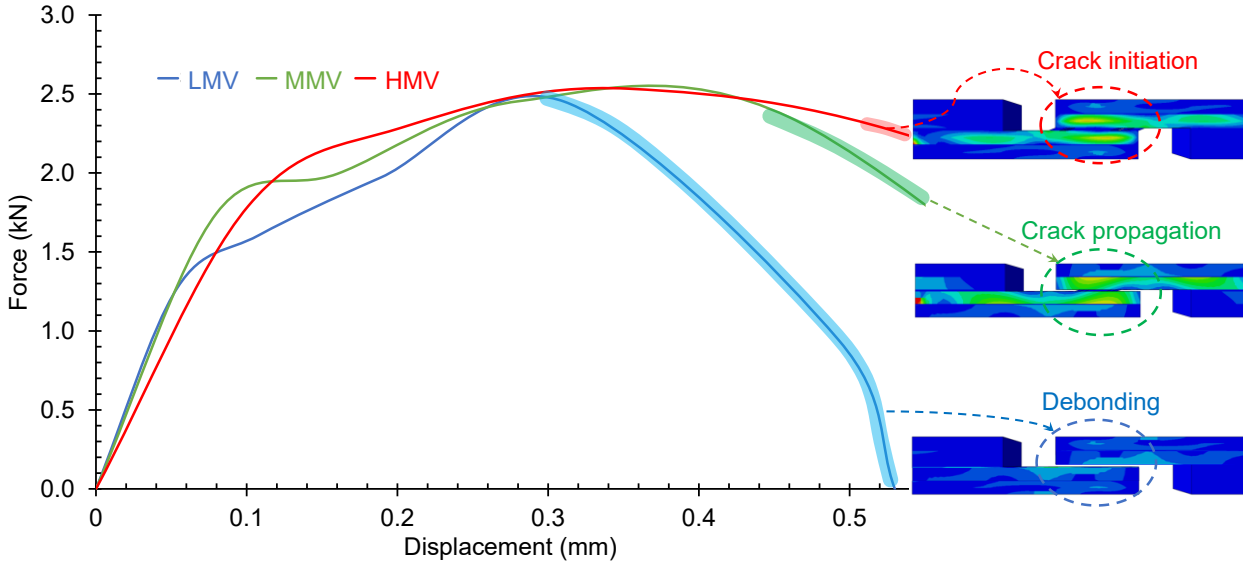

(**d**)

Figure 3.5. (a) Comparison of experimental and FE force-displacement results for LMV, MMV, and HMV specimens, (b) DDE force-displacement graph for the specimens, showing distinct energy dissipation behaviors, (c) DDE-displacement comparison among low, medium, and high mortar volume fractions, and (d) Simulated damage progression using element deletion technique.

The DDE graphs with respect to displacement depicted in Figure 3.5b exhibit a consistent trend across all specimens. However, a comparative analysis of these graphs, as illustrated in Figure 3.5c, enables an understanding of the distinct energy dissipation behaviors exhibited by each specimen. The analysis of the DDE graph elucidates key findings regarding the role of plasticity and crack propagation. A lower slope in the DDE graph corresponds to plastic deformation, while a steeper increase indicates the involvement of crack propagation. Figure 3.5c provides valuable insights into the energy dissipation characteristics among the specimens with varying mortar volume fractions. Notably, the LMV exhibits the highest rate of energy dissipation, reflecting a pronounced crack propagation rate and limited plastic deformation within the bonding area. Conversely, the HMV demonstrates the lowest rate of energy dissipation, indicative of a slower crack propagation rate and significant plastic deformation within the bonding area. In contrast, MMV exhibits an intermediate response in terms of energy dissipation. Furthermore, to visually simulate crack initiation, the element deletion technique is implemented. This method removes elements when their damage parameter reaches a critical value of 0.98. Analysis of displacement magnitudes reveals that crack initiation commences at 0.29 mm for the LMV specimen, subsequent to the dissipation of 0.14 J of energy accompanied by plastic deformation. In contrast, the MMV and HMV specimens require 0.33 J and 0.51 J of plastic dissipation energy at 0.46 mm and 0.53 mm, respectively, indicating a discernible delay in crack initiation with higher mortar volume fractions. These findings shed light on the distinct behaviors and energy dissipative treatments of the specimens, highlighting the complex interplay between crack propagation and plasticity. By employing element deletion techniques, the simulation enables the visualization of damage progression, offering valuable insights into the distinct stages of crack propagation within the samples. This sheds light on the intricate interplay between bonding conditions and displacement.

Figure 3.5d provides an illustration of the bonding conditions observed in the three samples under investigation. The results indicate that, at a displacement of 0.53 mm, the LMV sample undergoes complete debonding, while the MMV sample displays crack initiation from the edge of the overlap. In contrast, the HMV sample completes the hardening phase, ultimately leading to crack initiation. The experimental findings, along with the FEA results, demonstrate a robust and statistically significant correlation. This compelling correlation substantiates the validity of the two assumptions employed in the simulation. Consequently, it can be confidently inferred that the force-displacement data allows for the extraction of the traction-separation (TS) graph pertaining

to the specimens. The determination of the critical strain energy release rate in mode II (SERR) can be facilitated by evaluating the area enclosed by the TS graph.

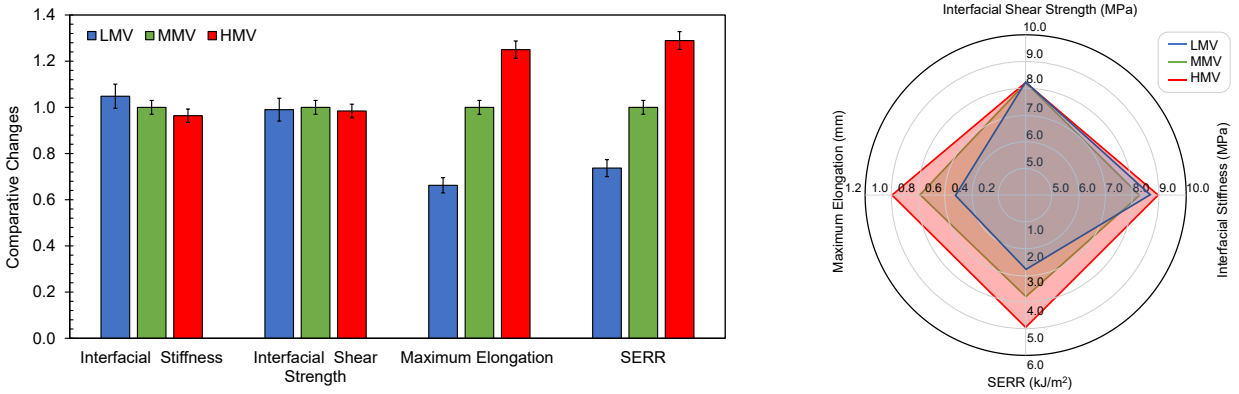

(**a**) (**b**)

Figure 3.6. (a) Comparative changes in mechanical properties (interfacial stiffness, interfacial shear strength, maximum elongation, and strain energy release rate in mode II) for LMV and HMV specimens with respect to MMV and (b) Absolute mechanical properties for the same specimens, illustrating the impact of varying mortar volume fractions.

Figure 3.6 presents a comprehensive and comparative analysis of the investigated parameters (interfacial stiffness, interfacial shear strength, maximum elongation, and SERR in mode II). Increasing the Surlyn content reduces interfacial stiffness without significantly affecting interfacial strength (see Figure 3.6). Higher mortar volume fractions in bioinspired ceramics promote greater tile sliding before separation, leading to a higher SERR. Compared to MMV sample, which resembles the composition of natural armors, the LMV and HMV specimens exhibit contrasting behaviors. The LMV sample displays 5% stiffer interfacial bonding but suffers from a 34% reduction in maximum elongation and a 27% decrease in SERR. Conversely, the HMV sample experiences a 4% decrease in interfacial stiffness, but demonstrates a commendable 25% increase in elongation capacity, leading to a significant enhancement of SERR by 28%. Intriguingly, interfacial strength remained statistically independent of mortar volume fraction, suggesting that increased Surlyn content solely promotes plastic deformation evident in adhesive failure. This implies that Surlyn's potential for enhanced load-bearing capacity and high-stress plasticity remains unutilized.

3.5 Conclusion

This study used both experimental and FE methods to explore the effect of mortar volume fraction on the interfacial properties of bioinspired ceramics. The results showed that increasing mortar volume enhances pre-debonding plastic deformation, while lower mortar volumes increase interfacial stiffness. Adhesive failure was the main fracture mode, with no significant effect of mortar volume on interfacial strength. To further validate the findings, a 3D model based on CZM was employed. The Quadratic Nominal Stress criterion captured damage initiation, while challenges in modeling damage propagation were addressed by appropriate assumptions. A suitable traction-separation law, derived from SLJ test data, was used to better capture the behavior at the interface. The correlation between experimental and FE results confirmed the validity of these assumptions and enabled the determination of critical interfacial parameters, including shear strength and mode II SERR. The study shows that mortar volume is a key factor in the design of bioinspired ceramics. Variations from the natural mortar volume (~5%) affect energy absorption capabilities. Lower mortar volumes reduce plastic deformation, leading to earlier crack initiation, while higher volumes reduce interfacial stiffness without altering bonding strength, which may affect the composite's structural integrity. These findings highlight the crucial role of interfacial properties in dictating energy dissipation mechanisms in ceramics. Furthermore, they suggest that nature employs alternative strategies to optimize interfacial bonding strength. Future research should focus on unraveling these strategies to enhance interfacial plastic deformation and crack deviation mechanisms. Exploring the optimization of mortar volume in other bioinspired architectures, such as hierarchical designs or multilayered structures, could provide further insights into improving the performance of these materials in applications requiring a balance of stiffness and energy dissipation.

Chapter 4:

Enhancing Ceramic Structural and Interfacial Properties via Micro-Patterning and Macro-Architectural Integration

In our previous study, presented in Chapter 3, we demonstrated that increasing the mortar volume fraction led to greater interfacial energy dissipation. However, fractographic and finite element analysis of the failed samples revealed that the adhesive failure mechanism remained largely unaffected by mortar volume. The observed increase in strain energy prior to failure was primarily attributed to enhanced plastic deformation within the polymer phase. This indicates that the interface between the ceramic and polymer remains a weak point, limiting the polymer's ability to absorb more energy through plastic deformation and crack propagation before detaching from the ceramic. To address this issue, we turned again to nature for inspiration. In many biological composites, particularly natural armors, ceramic components exhibit micro- and nano-scale surface patterns. These surface features act as a natural form of surface treatment, enhancing mechanical interlocking and modifying stress distribution at the interface. This critical design element had been absent from our initial bioinspired structures.

With this new insight, we proposed a novel strategy: Enhancing the Structural and Interfacial Properties of Ceramics via Micro-Patterning. By incorporating biologically inspired micro-patterns onto ceramic surfaces, and subsequently combining them with various macro-architectures, we aim to achieve greater control over the design and performance of bioinspired architected ceramic composites.

This work has been published in:

E. Azad, H. Yazdani Sarvestani, B. Ashrafi, F. Shadmehri, M. Hojjati, Enhancing Ceramic Structural and Interfacial Properties via Micro-Patterning and Macro-Architectural Integration. Adv. Mater. Technol. 2025, 2401439. https://doi.org/10.1002/admt.202401439

4.1 Abstract

This study investigates a dual-scale strategy combining micro-patterning with macro-architectural features to enhance the mechanical and interfacial properties of bioinspired ceramic composites. High-tolerance alumina tiles were precisely laser-micromachined with unidirectional (0°, 90°, and 45°) and bidirectional ((0°, 90°) and ±45°) patterns, then laminated with thermoplastic Surlyn® layers through vacuum bagging and heat treatment to achieve optimal bonding. Double lap joint (DLJ) and three-point bending (3PB) tests were performed to evaluate interfacial bonding, flexural behavior, and energy absorption. DLJ results indicated significant enhancement in interfacial bonding, with the ±45° pattern achieving a 107% increase in interfacial damage dissipation energy compared to plain specimens, attributed to mechanical interlocking and crack deflection. In 3PB tests, unidirectional patterns showed minimal impact on flexural properties, whereas bidirectional patterns reduced stiffness and strength. However, integrating micro-patterns with hexagonal macro-architectures notably improved energy absorption by 60% in laminated ceramic beams. This synergistic dual-scale approach represents a substantial advancement over conventional ceramics, enabling superior post-failure performance and energy absorption, with potential for resilient materials in aerospace and other high-performance applications.

4.2 Introduction

Advanced ceramic materials are renowned for their exceptional properties, including high hardness, excellent wear resistance, superior thermal stability, and chemical inertness, making them indispensable in applications such as aerospace components, biomedical implants, and protective equipment [77,78]. Despite these advantages, many ceramics are hindered by inherent brittleness, low energy absorption, and complex manufacturing processes that limit their broader use [9,15]. Among advanced ceramics, alumina stands out as a key material due to its outstanding mechanical strength, thermal stability, and corrosion resistance. These unique features not only facilitate the formation of robust composites but also address some of the challenges faced by other ceramic systems [79].

Recent advancements in materials science have focused on developing bioinspired ceramics that mimic intricate structures found in nature [7,18,40,60,80]. A particularly promising approach involves drawing inspiration from the brick-and-mortar architecture of nacre (mother-of-pearl), abalone shells, and other marine organisms [19,26,81,82]. These natural materials exhibit

exceptional mechanical properties due to their unique layered structures, which combine hard, brittle ceramics with flexible organic layers to enhance toughness and resilience. By emulating these natural designs, researchers aim to create advanced ceramics with improved impact resistance and energy absorption [25,36,56,83].

However, integrating these materials can lead to challenges such as delamination and debonding between ceramic and polymer layers [40,59,80,84]. These issues arise from differences in thermal expansion, mechanical properties, and adhesion characteristics between the materials, creating stress concentrations at the interfaces that compromise the integrity and performance of the composite [54,61,65]. Delamination and debonding compromise the overall integrity and performance of the ceramic composite, limiting its effectiveness in practical applications [10,12,85]. Addressing these challenges requires advancements in adhesive technologies and design strategies to improve bonding and stability between ceramic and polymer components [77,78,86].

Numerous studies have investigated the impact of interface geometry on toughening mechanisms and damage progression [55,83,87–94]. Analysis of microstructures in natural armors has identified rough and undulating morphologies at the interfaces between soft and hard components (see Figure 4.1) [14,95–97]. These nano- and micro-scale patterns promote plastic deformation and deflect interfacial cracks, leading to enhanced energy absorption [87,95,98].

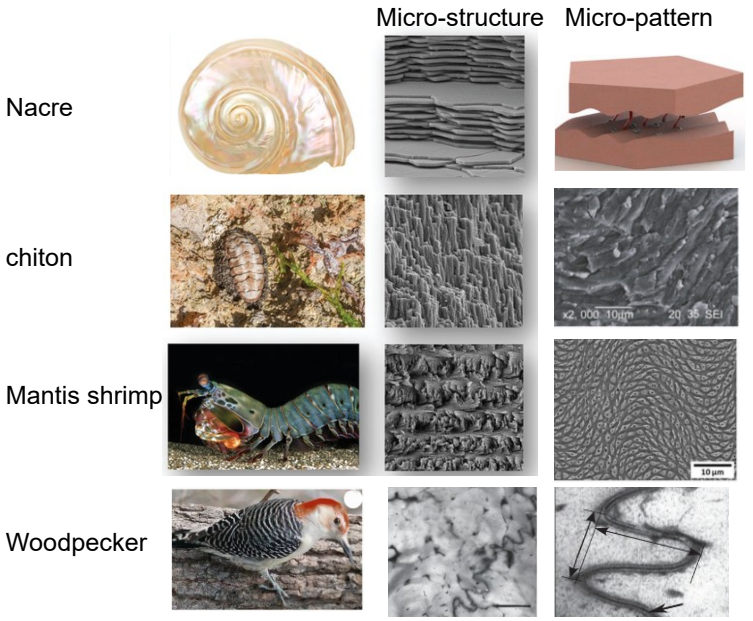

Figure 4.1. Interfacial micro-patterns observed in natural structures and armors [83,90–92,94].

Recent studies have shown that micro-patterns significantly affect the mechanical properties of bioinspired materials. For example, tablet waviness in nacreous composites improves load-sharing and energy absorption, with larger tablet inclinations further increasing energy capacity [35]. Other studies have investigated novel design and manufacturing processes for bioinspired materials [17]. For instance, bio-inspired surface textures in selective laser melting have enhanced shear strength in stainless steel joints by up to 70% [99], while integrating microgrooves with phosphoric acid anodizing on aluminum alloys increased shear strength by 42.24% [100]. Additionally, conical holes inspired by gecko feet have improved mechanical interlocking in bonded joints, enhancing displacement and resistance by nearly 100% and reducing stress peaks by 18.11% [101].

This study investigates the impact of micro-patterns and integrated hexagonal macro-architectures on the mechanical performance of bioinspired ceramic composites. High-tolerance alumina tiles were laser-micromachined with unidirectional (0°, 45°, 90°) and bidirectional (0°/90° and ±45°) patterns, then laminated with Surlyn® films using vacuum bagging and heat treatment. The composites were evaluated via DLJ and 3PB tests to assess interfacial bonding and flexural strength. While prior research showed that micro-patterns improve interfacial properties in soft materials, applying them to brittle ceramics is challenging due to the risk of crack propagation [86]. We addressed this by optimizing laser parameters to maintain structural integrity. Our analysis reveals that the 45° pattern notably enhances interfacial damage dissipation and toughness, and its integration with hexagonal macro-architectures further improves stress distribution and energy absorption. Four designs were explored: a pure one-layer ceramic with micro-patterns, a laminated ceramic with Surlyn® layers, a two-row hexagonal ceramic laminated with Surlyn® (focusing on cut depth and stacking direction), and a hexagonal ceramic with an additional 45° micro-pattern.

4.3 Materials and Methods

4.3.1 Design and Manufacturing

This study utilizes square, high-tolerance alumina ceramic tiles (96-99.8% Al_2O_3, density of 3875 kg/m^3), sourced from McMaster-Carr (No. 8462 K45), as the primary hard component. Alumina was chosen for its exceptional hardness, thermal stability, and wear resistance, making it an ideal candidate for structural applications where durability and resistance to extreme

environments are critical. The tiles have a thickness of 635 μm, providing a balance between mechanical strength and processability. For the soft polymer interface, a 100 μm thick Surlyn® thermoplastic skin film is employed. Surlyn® was selected for its excellent impact resistance, flexibility, and ability to bond with ceramics, which are essential properties for enhancing the toughness and energy absorption. Given the brittle nature of alumina, which is prone to fracture under compressive loads during assembly, an ultra-high-temperature impact-resistant glass fiber composite sheet (Garolite, McMaster-Carr, No. 3909 N22) is utilized as a supporting layer. This choice prevents premature failure during the manufacturing process and contributes to the overall structural integrity of the composite.

The process, depicted in Figure 4.2, involves placing the ceramic tiles and Surlyn® layers within a vacuum bag, followed by the application of a 5-hour heat treatment at temperatures up to 146 °C. This step is crucial for achieving optimal bonding between the ceramic and polymer layers, ensuring a robust interface that can withstand mechanical testing. Prior to lamination, the ceramic tiles are precision-cut into beams using a circular diamond saw.

Micro- and macro-patterns are applied to the ceramic beams using an Ytterbium picosecond fiber laser (YLPP-25-3-50-R, IPG Photonics, USA), a high-precision tool capable of creating intricate patterns with minimal thermal damage to the ceramic material. The laser micromachining process is conducted within a controlled environment equipped with an electronic XY linear stage (Aerotech) for precise positioning and a manual Z stage for depth control, as shown in Figure 4.2a. A Keyence IL-300 laser displacement sensor ensures accurate Z stage height measurements, enabling precise depth control, while a compressed conical air nozzle disperses fumes and provides localized cooling during machining, maintaining the integrity and precision of the laser patterns. To achieve high-quality micro-patterns, a detailed parametric analysis was conducted to identify the optimal laser parameters, building upon previous research [47, 48]. Post-machining analyses were conducted using confocal microscopy to evaluate the quality of the laser-induced micro-patterns. The analysis confirmed that the optimized laser parameters produced well-defined micro-patterns with consistent geometries and minimal surface irregularities.

Finally, the study examines four distinct design types:

1. **Design 1: Pure Single-Layer Ceramic**– This design serves as the baseline, consisting of a single layer of alumina ceramic with five different micro-patterns (0°, 90°, 45°, (0°, 90°) and ±45°) as well as a plain, un-patterned variant (see Figure 4.3a).

2. **Design 2: Laminated Ceramic**– This configuration includes a single layer of ceramic as the core, laminated with two layers of Surlyn® on the top and bottom surfaces. The same set of micro-patterns and a plain variant are applied to evaluate the impact of lamination on mechanical properties (see Figure 3b).
3. **Design 3: Hexagonal Ceramic Core with Surlyn Laminate**– This design introduces a hexagonal macro-architecture in the ceramic core, laminated with Surlyn® on both sides. Variations in cut depth and stacking direction are explored, including fully cut and partially cut configurations in both upward and downward stacking directions (see Figure 4.3c).
4. **Design 4: Hexagonal Core with Micro-Patterned Surface**– This design combines the hexagonal macro-architecture with the 45° micro-pattern, aiming to synergistically enhance the interfacial bonding and mechanical performance of the composite. It is worth mentioning that at least four samples are fabricated and tested for each design type (see Figure 4.3d).

4.3.2 Experimental Test Configuration

Two types of experimental tests are conducted: the double lap joint (DLJ) and the three-point bending (3PB) tests. DLJ specimens, featuring a lap joint length of 10 mm, are subjected to a displacement-controlled load condition of 1.3 mm/min using a tensile MTS universal testing machine. Displacement is monitored until complete separation occurs, indicating sliding at the interface of the lap joint. For the 3PB test, a fixed span length of 80 mm and a load condition of 1.3 mm/min (up to predetermined deflection of 12 mm) are used to assess the impact of micro-patterns on the strength reduction of alumina ceramic.

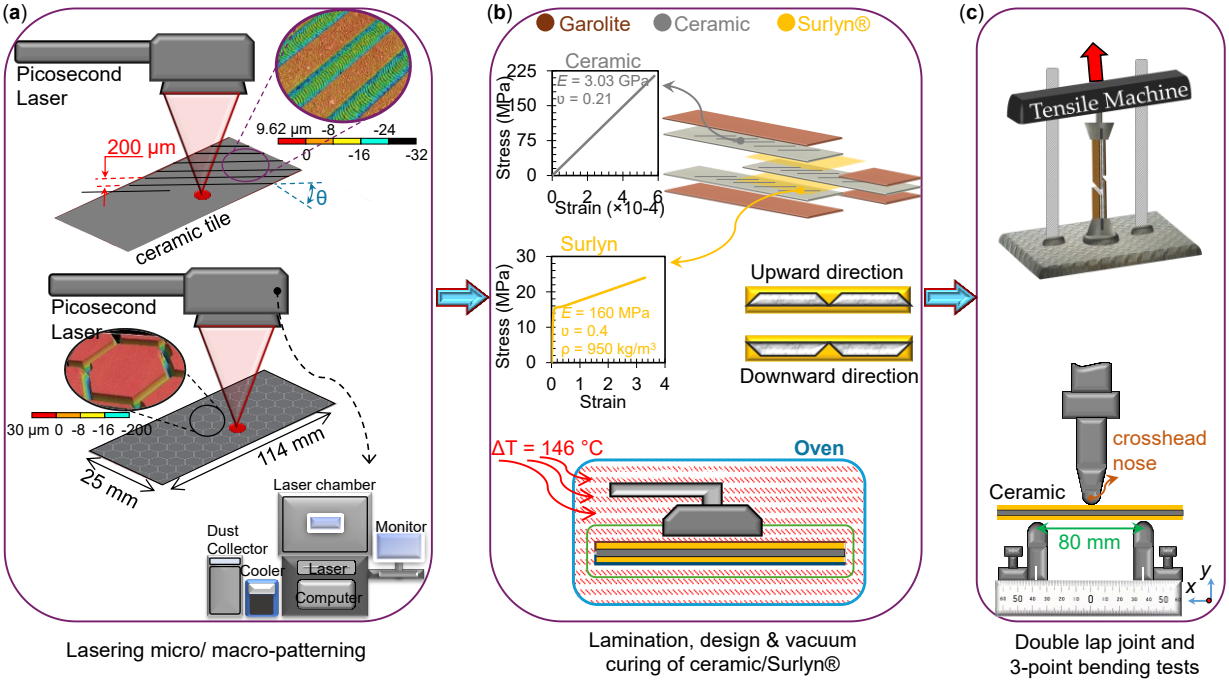

Figure 4.2. The manufacturing process of the architectural ceramic composite beams: (a) Macro and micro-patterning of ceramic tiles using subtractive manufacturing platform based on a picosecond laser, (b) Lamination of ceramic tiles with commercial monomer Surlyn®, followed by vacuum bagging and curing of the ceramic composites, and (c) Configurations for double lap joint and three-point bending tests.

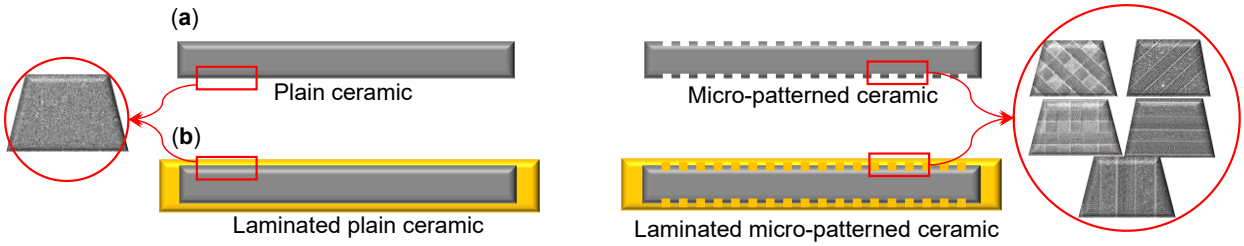

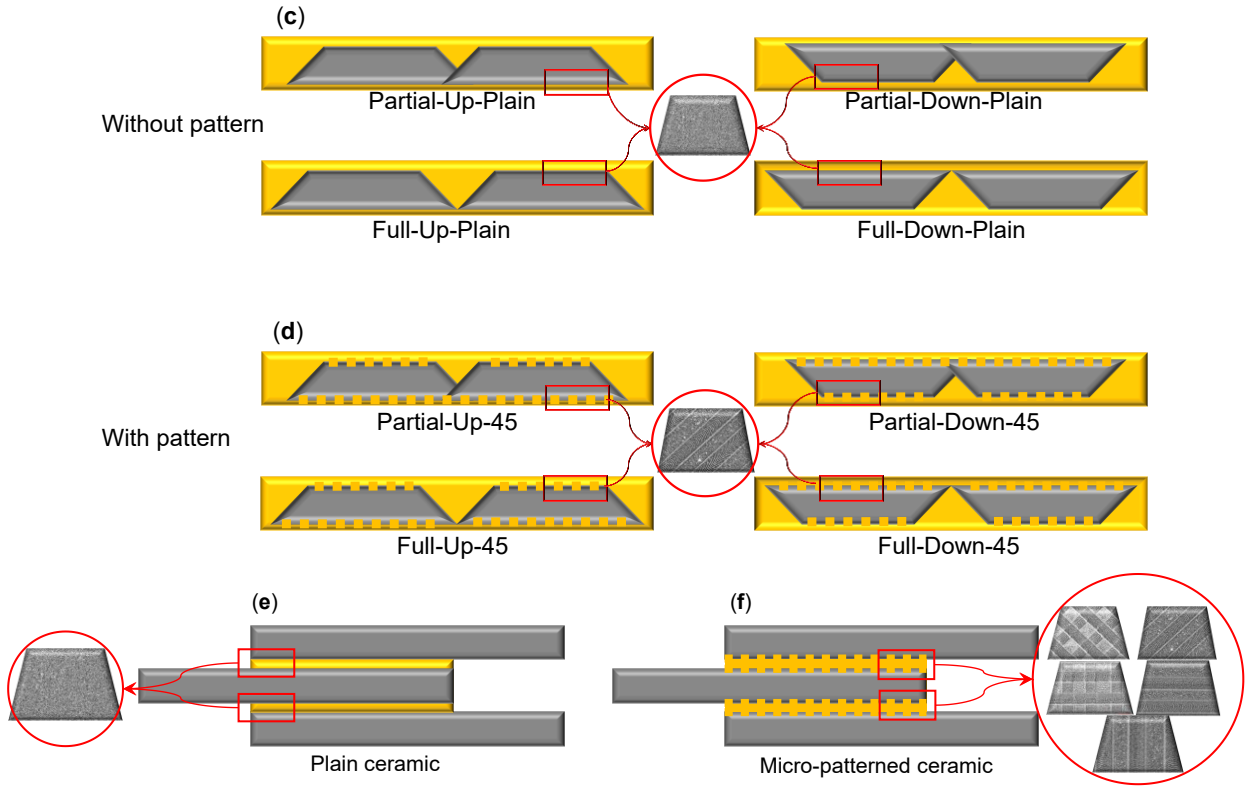

Figure 4.3. Design types: (a) Pure single-layer ceramic, (b) Laminated ceramic, (c) Hexagonal ceramic core with Surlyn® laminate, (d) Hexagonal core with the micro-patterned surface, (e) DLJ test without the lasered patterns, and (f) DLJ test with the lasered patterns.

4.4 Results and Discussion

This section presents the experimental findings on bioinspired ceramic composites featuring various micro-patterns and integrated designs. Four distinct designs were investigated. Design 1 involves pure one-layer ceramic with different micro-patterns (*Section 4.3.2i*), Design 2 comprises laminated ceramic incorporating Surlyn® layers (*Section 4.3.2ii*), Design 3 examines a two-row hexagonal ceramic laminated with Surlyn® layers with a focus on cut depth and stacking direction (*Section 4.3.3i*), and Design 4 features ceramic composites that integrate a 45º micro-pattern with the hexagonal design (*Section 4.3.3ii*). The performance of these designs was evaluated through DLJ tests for interfacial bonding and 3PB tests for flexural properties.

4.4.1 Investigation of the Role of Micro-patterns on Interfacial Properties

i. Analysis of the micro-patterns engraving

In the initial phase, laser micromachining parameters were carefully optimized to achieve high-quality micro-patterns on the ceramic surfaces. A targeted engraving depth of 20 µm and a kerf width of 200 µm were obtained, as summarized in Table 1. Figure 4.4 shows 3D laser scanning microscopy images that confirm the quality of the engraving. Two main types of patterns were applied. Unidirectional patterns were implemented in 0º, 90º, and 45º orientations, each producing distinct surface characteristics that are critical for optimizing interfacial properties. In contrast, cross patterns, applied in (0º, 90º) and ±45º configurations, offered alternative surface features that could influence the mechanical bonding and overall performance of the composite.

Table 4.1. Key parameters for laser micromachining.

Laser power (W)	Linear speed (mm/s)	Number of passes	Pulse frequency (Hz)	Wobble pattern shape	Wobble amplitude (mm)	Wobble frequency (Hz)
24	20	1	1000	Circle	0.2	800

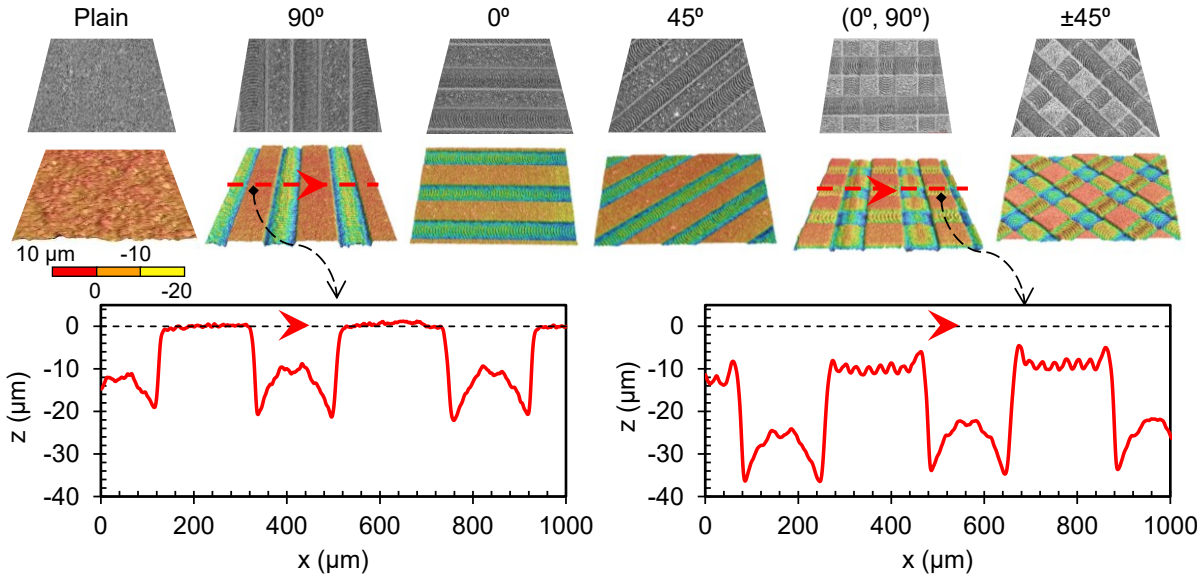

Figure 4.4. Microscopic analysis of micro-pattern engraving.

ii. Double lap joint shear test

Figure 4.5Figure 3.5 presents the force-displacement curves from the DLJ tests. The initial elastic segment, up to ~0.06 mm of displacement, exhibits a similar slope for all specimens, indicating that the micro-patterns have minimal influence on the initial elastic behavior. However, in the plastic region, the curves diverge markedly, revealing that the micro-patterns significantly affect stress distribution and plastic deformation within the adhesive layer. Plain ceramic specimens show a force plateau at about 5.5 kN, which indicates progressive damage at the interface. In contrast, micro-patterned specimens demonstrate higher ultimate forces and greater plastic deformation prior to failure. For instance, the 90º pattern reaches an ultimate load 7 kN with a maximum displacement of 0.45 mm, while the 0º pattern attains 8 kN at a displacement of 0.6 mm. Both the 45º and ±45º patterns exhibit superior performance with ultimate forces exceeding 9 kN and the ±45º configuration showing the highest deformation (~0.64 mm). Additionally, a shift in failure mode is observed; plain ceramics display purely adhesive failure, whereas patterned surfaces exhibit a combination of adhesive and cohesive failure, with interfacial cracks deflecting along the patterned interfaces. As further detailed in *Section 4.3.4*, the observed increase in energy dissipation can be attributed to enhanced crack deflection and mechanical interlocking mechanisms predicted by fracture mechanics theories.

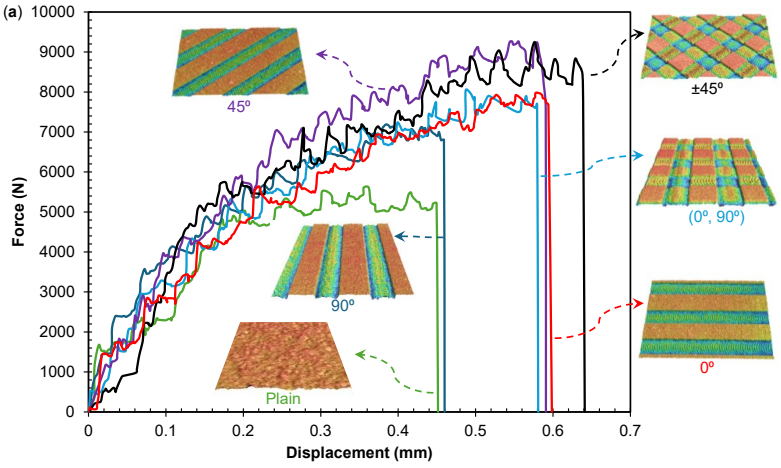

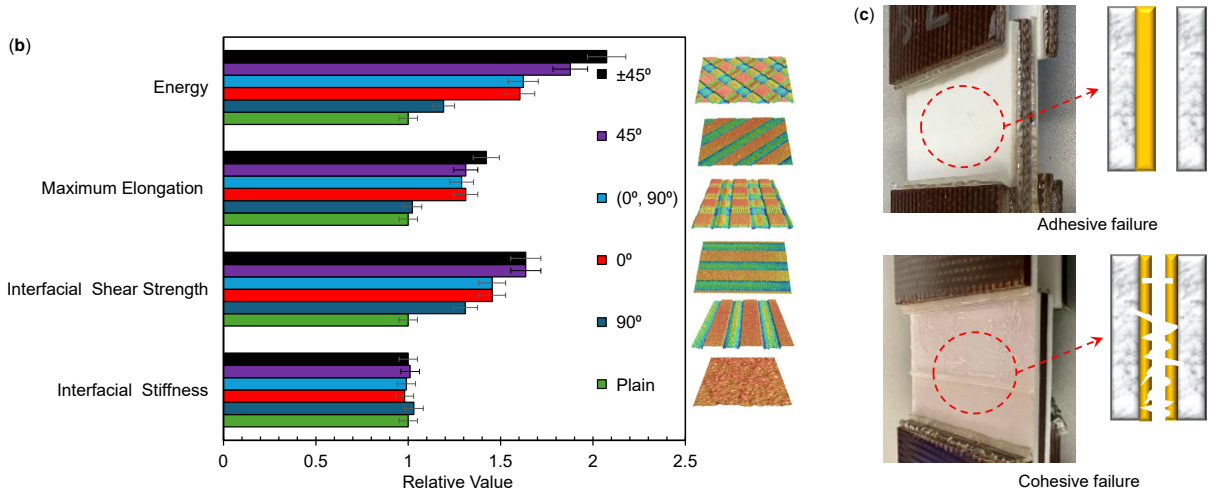

Figure 4.5. Double lap joint shear test results and fractography: (**a**) Force-displacement graph from the DLJ test, (**b**) Relative values of different mechanical properties, and (**c**) Fractography after complete debonding, illustrating various failure modes.

4.4.2 Effects of Micro-Patterns on the Flexural Behavior of Pure and Laminated Ceramic

Micro-patterns in this study involve minimal material removal yet can create localized stress concentrations that may affect ceramic strength. Additionally, laminating brittle ceramic with a ductile polymer yields composites with enhanced energy absorption and deflection, as the polymer distributes stresses and delays crack initiation. Effective interfacial bonding is essential for load transfer, and the presence of micro-patterns can significantly influence these properties and the overall flexural behavior of the composite beams. Various samples were fabricated to explore these effects, and Figure 4.6 shows the 3PB test setup for both pure and laminated ceramics, with and without micro-patterns. The following sections detail the results of this investigation.

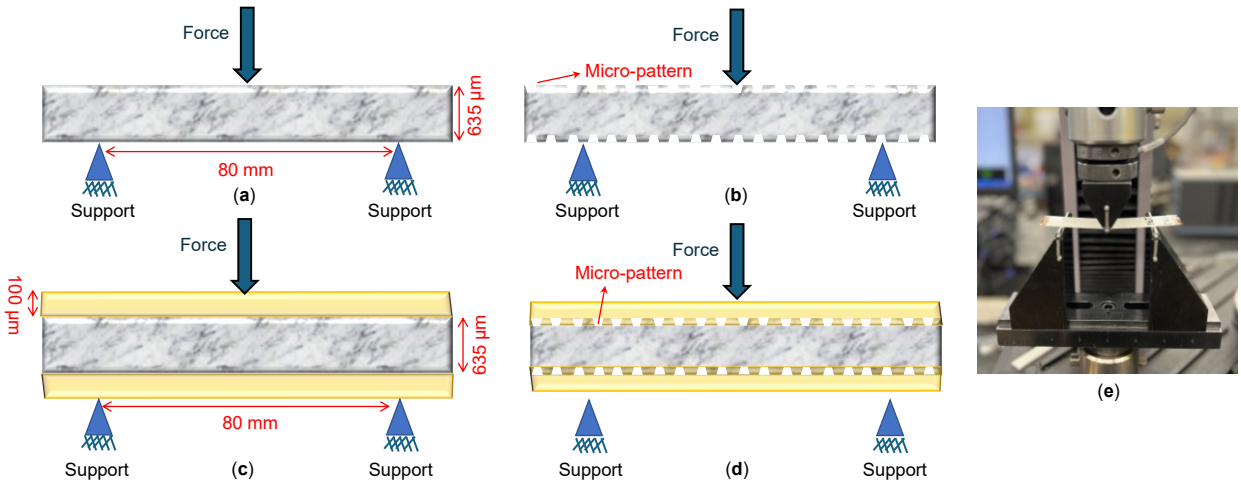
Force
635 µm
80 mm
Support
(a)
Support
Force
Micro-pattern
Support
(b)
Support
Force
100 µm
635 µm
80 mm
Support
(c)
Support
Force
Micro-pattern
Support
(d)
Support
(e)

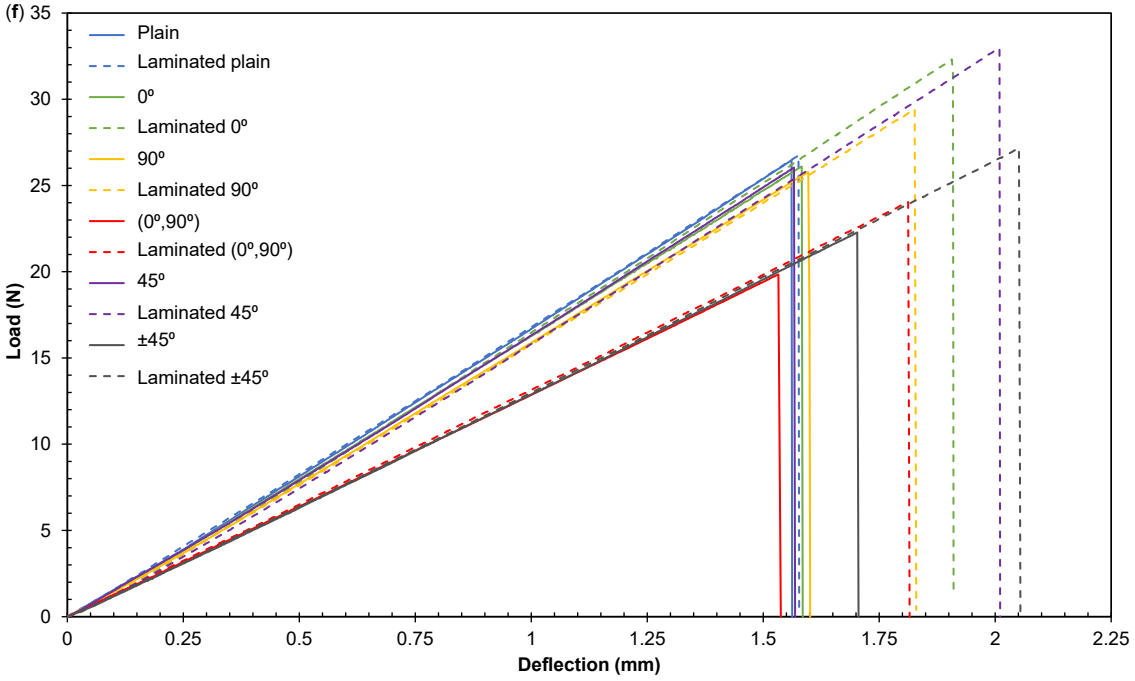
(f)
Plain
Laminated plain
0º
Laminated 0º
90º
Laminated 90º
(0º,90º)
Laminated (0º,90º)
45º
Laminated 45º
±45º
Laminated ±45º
Load (N)
Deflection (mm)
0
5
10
15
20
25
30
35
0
0.25
0.5
0.75
1
1.25
1.5
1.75
2
2.25

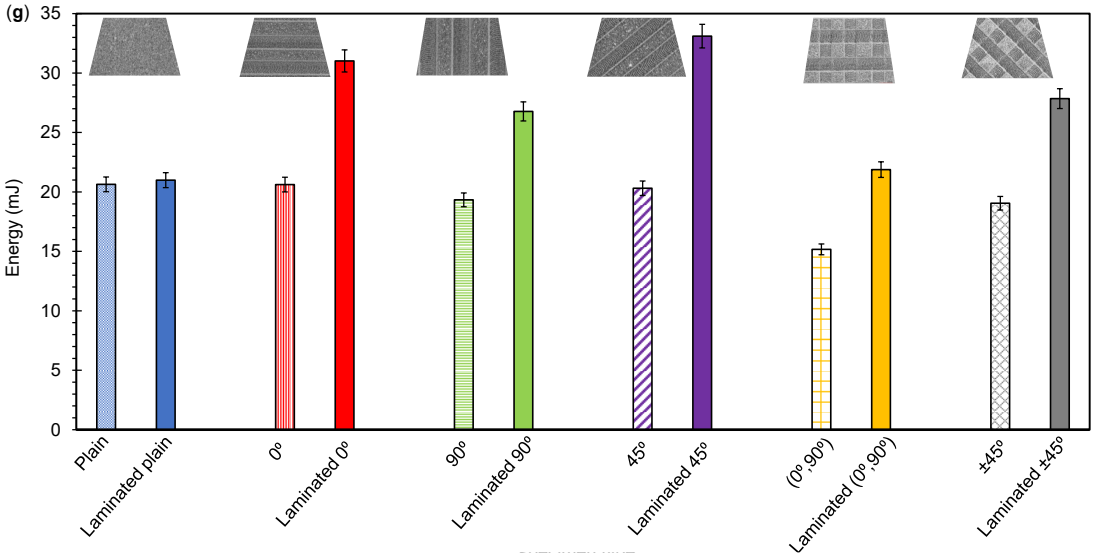
(g)
Energy (mJ)
0
5
10
15
20
25
30
35
Plain
Laminated plain
0º
Laminated 0º
90º
Laminated 90º
45º
Laminated 45º
(0º,90º)
Laminated (0º,90º)
±45º
Laminated ±45º

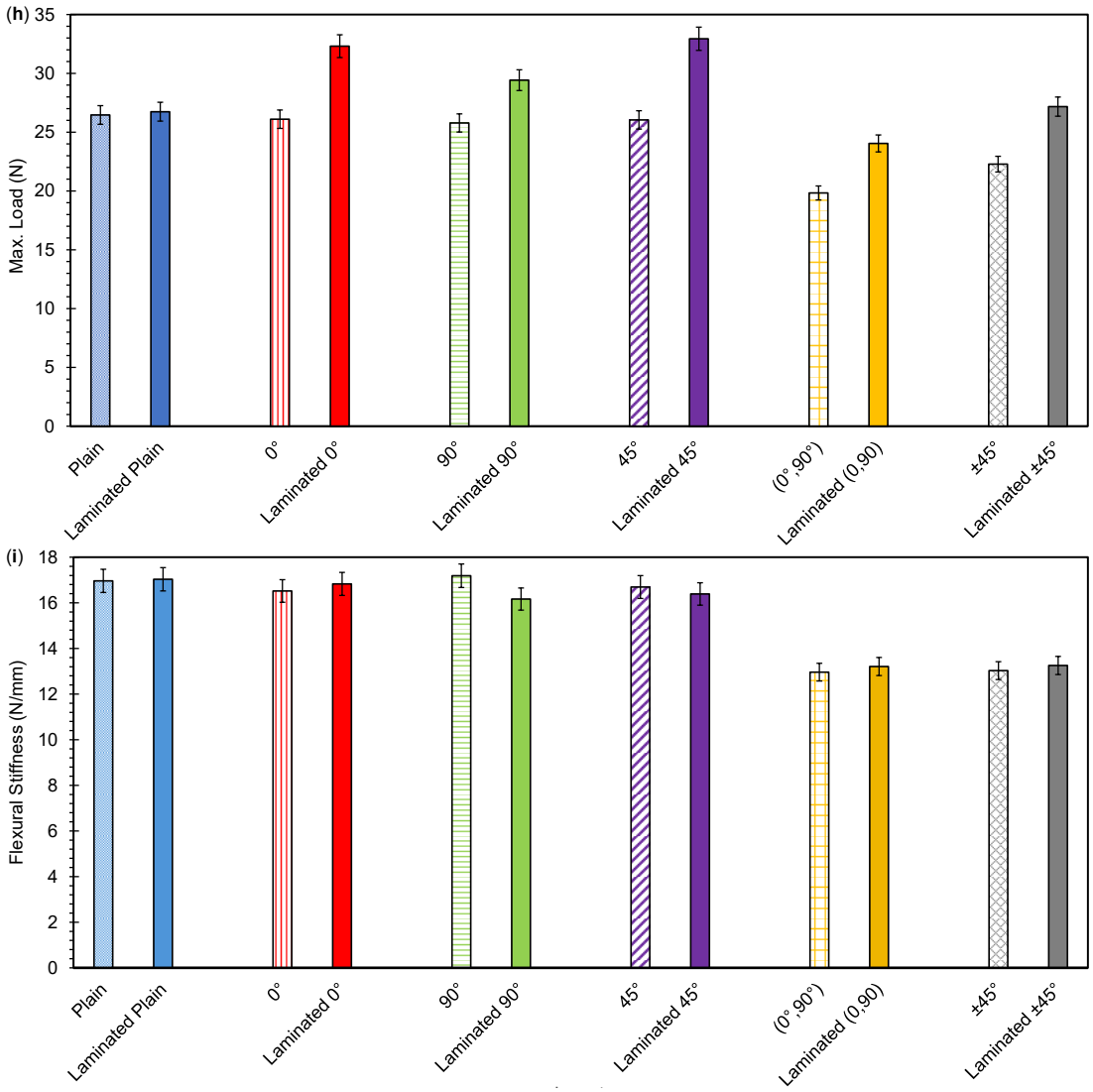

Figure 4.6. Three-point bending test of pure and laminated ceramic: (a) Schematic of pure plain ceramic beams, (b) Pure micro-patterned ceramic beams (0º, 90º, 45º, (0º, 90º) and ±45º), (c) Laminated plain ceramic beams, (d) Laminated micro-patterned ceramic beams (0º, 90º, 45º, (0º, 90º) and ±45º), (e) 3PB test setup, (f) Load-deflection graph, (g) Comparison of energy absorption, (h) Comparison of maximum load capacity, and (i) Comparison of flexural stiffness across different designs.

i. Impact of laser machining on the mechanical properties of pure plain ceramic

In this experiment, laser machining was used to create five distinct micro-pattern designs on alumina ceramic beams, each measuring 114 mm in length and 25 mm in width. The micro-patterns included orientations of 0º, 90º, 45º, (0º, 90º) and ±45º, and were applied to both sides of the beams. 3PB tests were conducted to assess and compare the flexural behavior of these patterned beams with that of plain ceramic beams.

- **Unidirectional Patterns:** The unidirectional micro-patterns (0º, 90º and 45º), involving around 6% material removal, did not lead to significant changes in the flexural properties of the beams. These patterns maintained structural integrity while providing surface texturing.
- **Bidirectional Patterns:** The bidirectional patterns (0º, 90º) and ±45º created regions with depths of ~35 μm, removing over 10% of the thickness in these regions. This substantial material removal likely weakened the mechanical properties of the alumina tiles, leading to a 23% decrease in flexural stiffness and a reduction in failure load by 25% for the (0º, 90º) design and 16% for the ±45º design. The degradation was primarily due to the reduced thickness and increased stress concentrations in the deeply patterned regions.

The results indicate that unidirectional micro-patterns are advantageous for applications requiring surface texturing without significantly impacting the structural integrity of the ceramic material. Conversely, bidirectional micro-patterns pose a significant challenge due to their adverse effects on mechanical performance.

ii. Role of Micro-Patterned Interfaces on the Flexural Properties of Laminated Ceramic

In this section, we examine the influence of micro-patterned interfaces on the flexural performance of laminated ceramic composites. Alumina beams were centrally laminated between single Surlyn® layers on both top and bottom surfaces. According to Figure 4.6, the overall flexural stiffness remains largely constant due to the alumina layer's high modulus and thickness compared to the Surlyn® layers. However, the micro-patterned samples exhibited a significant increase in failure load under 3PB tests. This enhanced load-bearing capability stems from improved bonding between Surlyn® and alumina, resulting in more uniform stress distribution and reduced local stress concentrations-common initiation points for cracks in brittle ceramics. In contrast, plain laminated samples experienced localized delamination due to weaker bonding, creating regions prone to crack initiation. The presence of micro-patterns effectively mitigates these effects by promoting stronger interfacial adhesion, which prevents early delamination and subsequent crack propagation. Surlyn® layers further contribute to the overall toughness by absorbing applied mechanical energy through elastic and plastic deformation mechanisms, such as bond rotation and polymer chain deformation. This energy absorption minimizes the transmitted energy to the ceramic, reducing fracture risks. The effectiveness of these toughening mechanisms directly correlates with the quality of interfacial adhesion, notably enhanced in micro-patterned configurations. Among the micro-patterns studied, the 45º orientation was most effective, achieving an ~88% increase in interfacial damage dissipation energy compared to plain samples,

as discussed in *Section 3.1.2*. This improvement translates directly into enhanced flexural performance, with a corresponding 60% increase in energy absorption for the 45º-patterned laminates during 3PB tests, as highlighted in Figure 4.6.

4.4.3 Comparing Roles of Micro-patterns and Macro-architecture

The results from the 3PB tests were consistent with those obtained from the DLJ tests, reinforcing the effectiveness of the 45º micro-pattern in enhancing the bond between the Surlyn® layer and alumina tile. Consequently, the 45º micro-pattern was selected for application to hexagonal tiles to create a bioinspired ceramic with integrated patterns. In this experiment, ceramic beams were designed with two layers of Surlyn® and one layer of alumina with integrated patterns sandwiched between them. These beams were subjected to 3PB tests to evaluate their performance. Two rows of hexagonal patterns were incorporated into the center of these beams (see Figure 4.7). Additionally, the 45º micro-pattern was applied to the surface of the hexagonal tiles in another set of samples to investigate the combined effects of integrating the micro-pattern with the macro-pattern (see Figure 4.7). Previous studies have highlighted that the cutting depth of hexagonal patterns significantly influences the energy absorption of bioinspired ceramic composites under impact testing [25]. Furthermore, research has demonstrated that stacking directions and orientations in layered architected ceramics affect their flexural properties [27]. To gain a comprehensive understanding of the role of each pattern, this study will first examine the impact of integrating micro-patterns with different cut depths of the hexagonal patterns. Subsequently, the effects of integrating the micro-pattern with the stacking direction of the hexagonal patterns will be investigated.

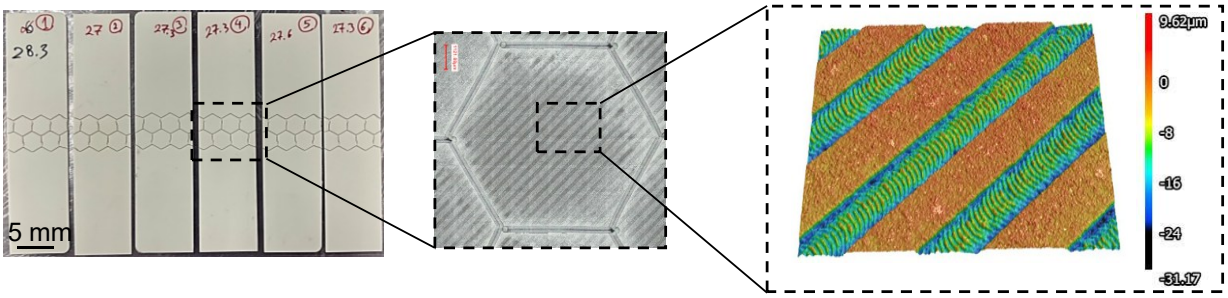

(**a**)

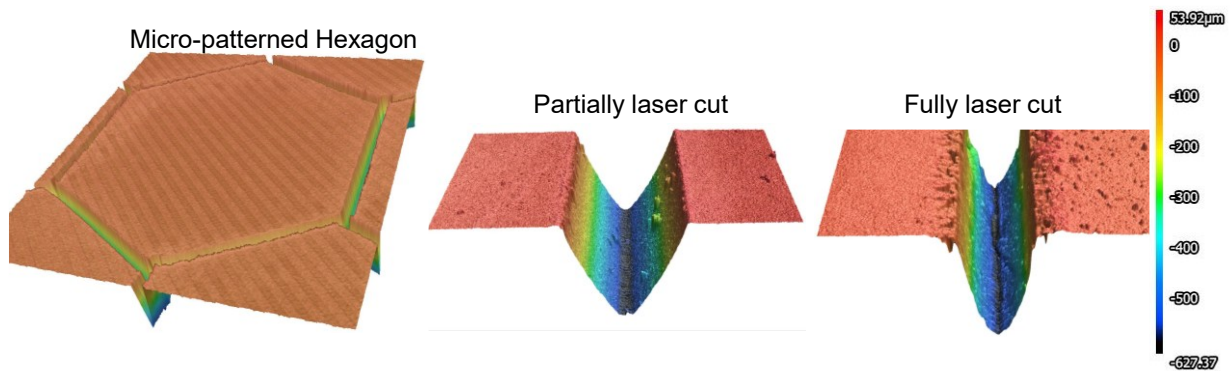

(**b**)

(**c**)

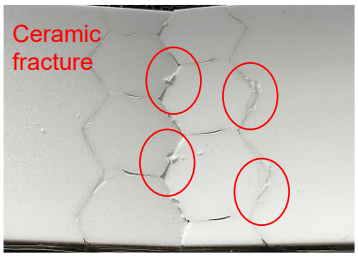

(**d**)

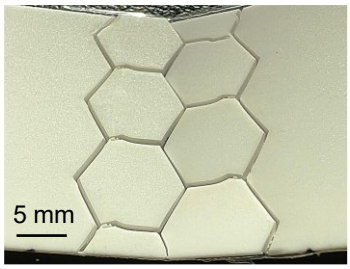

(**e**)

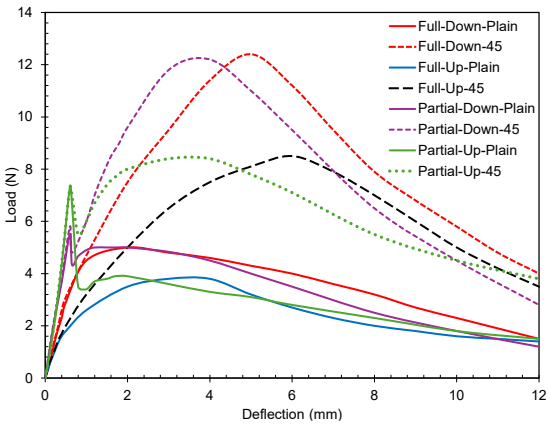

(**f**)

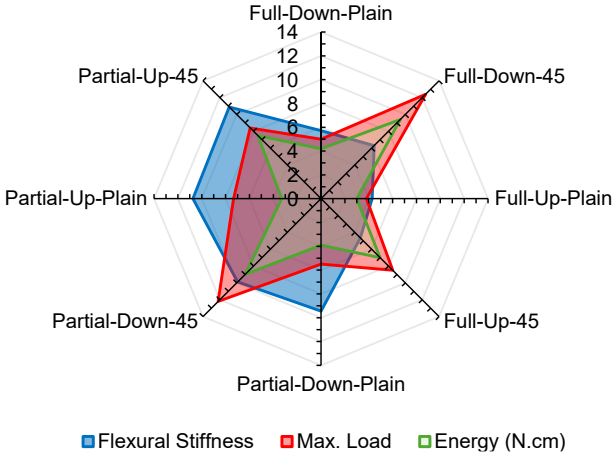

(**g**)

Figure 4.7. Integration of micro-pattern and macro-architectures: (a) Integration of macro-architecture with micro-pattern in the two-row hexagonal samples, (b) Confocal microscopy of micro-patterned hexagons in partially and fully cut samples, (c) Test setup of two-row hexagonal samples under 3PB, (d) Fractography showing ceramic fracture as the first failure mechanism in partially cut samples, (e) Rigid body movement of hexagonal tiles after bending in fully cut samples, (f) Load-deflection graph of eight different designs under 3PB load conditions, and (g) Radial graph comparing flexural stiffness, maximum load and energy absorption.

i. Role of cutting depth vs. stacking direction of hexagonal patterns

To investigate the influence of alumina, Surlyn®, and stacking direction on the flexural behavior of bioinspired ceramic composite beams, samples were fabricated in fully cut and partially cut configurations. In fully cut samples, hexagonal patterns were engraved completely through the 635 μm thickness of the alumina sheet, creating individual hexagonal blocks resembling a brick-and-mortar structure. In partially cut samples, 15% of the ceramic thickness remained at the base between hexagons, facilitating load transfer. Both configurations were laminated with Surlyn® thermoplastic layers on their top and bottom surfaces. The hexagonal design was selected for its bioinspired structural advantages, including enhanced stress redistribution and energy absorption. Laser micromachining was employed to achieve precise control over the pattern geometry and cutting depth. The fully cut configuration was hypothesized to provide flexibility and enhanced energy dissipation, while partially cut samples were expected to maintain higher stiffness due to the residual ceramic bridges. The samples were tested using 3PB in two stacking orientations: upward (hexagonal apex outward) and downward (hexagonal flat sides aligned with laminate surface). The partially cut configuration demonstrated higher flexural stiffness compared to fully cut samples, with 150% and 66% increases for upward and downward stacking directions, respectively. The upward orientation showed 14% higher stiffness than downward in partially cut samples, attributed to the kerf closing under load, whereas in fully cut samples, the downward direction exhibited 24% greater stiffness due to better stress redistribution. Energy absorption was significantly higher for fully cut samples, especially in the downward stacking direction, due to greater deformation and effective stress redistribution facilitated by the flat sides of hexagonal tiles engaging more effectively with the Surlyn® layers. Fractographic analyses indicated distinct failure behaviors: fully cut samples experienced progressive cracking and delamination with rigid tile movements, whereas partially cut samples exhibited localized fracture initiation within ceramic bridges. Damage initiation also varied by configuration and stacking direction. Partially cut samples initiated damage via fracture of ceramic bridges, with downward-oriented samples exhibiting 25% lower fracture loads due to kerf opening. Upward-oriented samples maintained higher loads post-fracture due to the interaction between tile edges in compression. Fully cut samples exhibited maximum loads at smaller deflections, with plastic deformation occurring predominantly in the Surlyn® layers. Overall, downward stacking directions in both configurations supported higher loads during damage progression, attributable to effective ceramic tile interaction

under compressive stress. At high deflections, sharp edges of hexagonal tiles penetrated Surlyn®, causing near-separation. These findings highlight the critical roles of cutting depth and stacking direction in optimizing the structural performance and failure characteristics of bioinspired ceramic composites.

ii. Role of micro-pattern vs. hexagonal pattern

In this section, the 45º micro-pattern was applied to the four specimen types discussed in *Section 3.3.1*, and their flexural behavior was evaluated using 3PB tests, compared to plain, unpatterned samples. Results indicate that the micro-pattern does not significantly influence the elastic behavior, with flexural stiffness primarily determined by the hexagonal macro-architecture. The DLJ tests confirmed that the stress distribution at the interface in the elastic regime remains unaffected by micro-patterning, reinforcing the dominant role of the hexagonal design at this stage. However, significant improvements were observed in the post-elastic behavior of micro-patterned samples. Partially cut specimens with the 45º micro-pattern exhibited pronounced hardening after initial failure, attributable to substantial plastic deformation within the Surlyn® layer. This plastic deformation allowed Surlyn® to absorb more energy before debonding from the alumina, resulting in an ~120% increase in maximum load for the downward stacking configuration. Similarly, fully cut specimens with the micro-pattern showed notable enhancements, with maximum failure loads increasing by approximately 150% in the downward and 120% in the upward stacking directions, confirming the critical role of micro-patterns in enhancing interfacial properties. Energy absorption was significantly higher in micro-patterned samples compared to plain counterparts, particularly in the downward stacking direction for both fully and partially cut configurations. In partially cut samples, energy absorption began with ceramic fracture, followed by plastic deformation of Surlyn® and interactions among neighboring hexagonal tiles. In fully cut samples, energy absorption initiated with rigid tile movement, plastic deformation in Surlyn®, and frictional interactions between neighboring tiles. Overall, the combined micro- and macro-scale designs led to more than a 200% improvement in energy absorption, underscoring the critical role of dual-scale optimization for enhanced mechanical performance.

4.5 Conclusion

This study introduces a dual-scale design strategy that synergistically combines micro-patterning and bioinspired macro-architectural features to significantly enhance the mechanical and interfacial properties of ceramic composites. Precision laser micromachining was employed to integrate high-tolerance alumina ceramic tiles with Surlyn® thermoplastic films, effectively improving interfacial adhesion and energy absorption. The ±45º micro-pattern notably achieved a 107% increase in interfacial damage dissipation energy, promoting effective mechanical interlocking and crack deflection. Furthermore, this micro-pattern improved energy absorption by approximately 60% in laminated ceramic beams during flexural loading, indicating a substantial increase in toughness. The integration of micro-patterns with hexagonal macro-architectures demonstrated complementary roles: hexagonal patterns optimized elastic stress distribution and load transfer, while micro-patterns significantly enhanced post-elastic energy dissipation and mitigated damage progression. Experimental results suggest that partially cut hexagonal configurations provide higher flexural stiffness ideal for load-bearing applications, whereas fully cut designs excel in energy dissipation, beneficial for impact-resistant uses. The practical implications of these findings are significant, highlighting their potential use in advanced structural applications. Enhanced mechanical properties, particularly improved energy absorption and interfacial bonding, translate directly to increased reliability and durability in high-performance environments. Aerospace components can benefit from reduced maintenance requirements and prolonged service life, automotive applications gain improved crashworthiness, while robotics and personal protective equipment can achieve superior resilience under extreme conditions. This integration of scalable laser micromachining and bioinspired designs thus represents a meaningful advancement, paving the way for the development of next-generation ceramic composites tailored to demanding applications.

Chapter 5:

From Macro to Micro: Bioinspired Designs for Tougher Ceramics

Building on the successful outcomes of our previous study, we found that incorporating micro-patterns significantly enhanced both the interfacial and structural properties of the composites, especially when combined with a hexagonal macro-pattern. With this foundation, we now turn our focus to the development of bioinspired laminated ceramics. During our earlier experimental investigations, we observed that the hexagonal macro-pattern imparts bimodular behavior to the ceramic tiles, resulting in distinct mechanical responses on the top and bottom surfaces. This finding opens the door to various laminate designs by altering the stacking sequence and orientation of the hexagonal patterns. We hypothesize that these different configurations, driven by changes in cell geometry, play a crucial role in defining the mechanical properties of the bioinspired ceramic laminates, much like the role of geometry in the microstructure of natural armors. By integrating micro-patterns, macro-patterns, and tailored stacking sequences, we aim to create a new class of programmable materials with tunable mechanical properties. In this study, we investigate the performance of these laminates under both static and cyclic loading conditions to better understand their behavior and potential applications.

This work has been published in:

E. Azad, H. Yazdani Sarvestani, B. Ashrafi, F. Shadmehri, M. Hojjati, From macro to micro: Bioinspired designs for tougher ceramics, Journal of Materials Research and Technology, Volume 31, 2024, Pages 3310-3319, ISSN 2238-7854, https://doi.org/10.1016/j.jmrt.2024.07.019.

E. Azad, H. Yazdani Sarvestani, B. Ashrafi, F. Shadmehri, and M. Hojjati, Bioinspired Ceramics: Harnessing Nature's Strategiesfor ImprovingInterfacial Strengthand Energy Absorption, CANCOM 2024

E. Azad, H. Yazdani Sarvestani, B. Ashrafi, F. Shadmehri, and M. Hojjati, Biomimetic Architected Ceramics: Enhancing Interfacial Properties and Energy Absorption through Surlyn-Alumina Composites, ECCM21, 2024

5.1 Abstract

Ceramic materials, while strong, often lack flexibility and energy absorption. Inspired by tough natural structures like nacre, toughening strategies have shown significant potential in ceramic materials. This study investigates the static and cyclic flexural properties (i.e., energy absorption, stiffness, and strength) of the bioinspired ceramic-polymer composites, particularly concerning the influence of macro and micro patterns. Using a subtractive manufacturing platform enabled by ultra-short pulsed picosecond lasers, we engrave a range of macro and micro patterns onto alumina tiles, mimicking natural armor designs. The composites are then fabricated by stacking laser-engraved tiles with an interlayer of Surlyn®, a commercial monomer. The results demonstrate that the static/cyclic performance and toughening mechanisms are closely linked to the laser bioinspired surface patterns and stacking sequence. Specific macro architectures and stacking sequences led to significantly increased energy absorption (up to 85%) through mechanisms like crack deflection and plastic deformation of the soft phase. Micro patterns, on the other hand, improved the ceramic's strength (up to 140%) by influencing how the materials interact at the interface. This research not only advances our understanding of bioinspired armor but also paves the way for a new generation of ceramic composites with superior properties, targeting applications in defense (aerospace and vehicle armor) and personal protective equipment (PPE).

5.2 Introduction

Ceramics are indispensable materials in various fields due to their exceptional thermo-mechanical properties, hardness, durability, and low electrical conductivity. However, their inherent brittleness poses a significant challenge, limiting their damage tolerance [2,3,102]. Despite numerous attempts to overcome this issue through strategies such as nano-material dispersion [4] and microstructure control [5], significant improvements in impact resistance and toughness have remained elusive.

Nature provides promising solutions to address the brittleness of ceramics through inspirational motifs and unique design concepts [2,6,7,103,104]. Microstructural architectures observed in natural materials, such as cross-ply patterns found in fish scales and tooth enamel, offer reinforcement through mechanisms like crack bridging and deflection [1,105,106]. Furthermore, composites featuring lamellar and brick-and-mortar architectures demonstrate hardness and Young's modulus profiles that closely resemble those of human dentin and enamel, respectively.

These composites exhibit exceptional fracture toughness, high machinability, excellent biocompatibility, and impressive wear resistance, making them attractive for dental applications [8,107,108].

In materials like nacre, inelastic deformations within a process zone surrounding cracks dissipate significant amounts of energy, constituting the primary toughening mechanism [109–112]. Interfaces in nacre and other natural materials exhibit complex architectures that amplify their local response, leading to exceptional combinations of stiffness, strength, and toughness[13,14,113,114]. For example, the heterogeneous architecture of beetle cuticles, with helicoidal arrangements of chitin fibers, initiates localized toughening mechanisms, reducing weight while enhancing mechanical performance [115].

Recent years have witnessed attempts to integrate bioinspired architectures with ceramics, aiming to achieve an optimized balance of stiffness, strength, and toughness [10–12,116]. Conventional methods for fabricating bioinspired ceramics include techniques such as freeze-casting, 3D printing, and layer-by-layer assembly [117–119]. However, these methods often face limitations in scalability, precision, and the ability to control complex architectures, which are essential for mimicking natural designs' intricate features. For instance, freeze-casting can create aligned porosity but struggles with precise control over architectural complexity, while 3D printing offers customization but is often constrained by resolution and material selection [120].

In response to the limitations of existing bioinspired approaches, such as difficulty in achieving precise control over multiscale features, we have developed a digital manufacturing platform that offers precise control over the 3D architecture, including cut depth (micro-patterns), and cell geometry (macro-patterns). This programmable manufacturing tool addresses the limitations of existing methods by enabling scalable production of complex, bioinspired designs with high precision. Utilizing this platform, we have fabricated multilayered ceramic composites comprised of bioinspired hard building blocks supplemented with soft interlayers. Through experimental investigation, we compare the static and cyclic mechanical performance of these multilayered ceramics with and without macro- and micro-patterns, as well as different stacking sequences. This approach yields a new class of ceramics with predictable mechanical responses. Tailoring stacking sequences and bioinspired patterns allows for controlled energy absorption, strength, and stiffness, paving the way for advanced composites.

5.3 Materials and Methods

5.3.1 Design and Manufacturing

Square, high-tolerance nonporous alumina ceramic tiles (96-99.8% Al_2O_3, 3875 kg/m^3 density, fired, McMaster-Carr, No. 8462 K45) with a thickness of 635 µm serve as the hard building blocks. A 100 µm thick Surlyn® thermoplastic skin film acts as the soft polymer interface between these tiles. Inspired by nacre's brick-and-mortar structure, this design utilizes larger-scale components but maintains a similar volume fraction (~93% ceramic) as natural nacre. This approach allows us to investigate the impact of patterns on the mechanical performance while mimicking the bioinspired principles behind nacre's remarkable toughness. The ceramic tiles are circular diamond saw-cut into four beams, each measuring 25 mm wide and 114 mm long due to the pre-existing tile size. While the specimen width adheres to ASTM D790 standards (25 mm), the length deviates slightly (114 mm vs. minimum requirement of >100 mm). Laser machining was performed on the tiles before lamination, utilizing the previously established optimal process parameters for alumina laser machining [32,121–123]. An Ytterbium picosecond fiber laser (YLPP-25-3-50-R, IPG Photonics, USA), with a maximum average power of 50 W, is employed as the primary laser source within the chamber, which housed a micromachining stage comprising an electronic *xy*-linear stage (Aerotech) and a manual z-stage. The laser system generates a Gaussian spatial profile beam emitting 3 ps long pulses with an energy of 25 µJ at a wavelength of 1030 nm. It has the capability of operating at a repetition rate of up to 1.83 MHz. A Keyence IL-300 laser displacement sensor ensured accurate z-stage height measurements. A compressed conical air nozzle facilitated fume dispersion, maintaining laser efficiency, preventing beam divergence, and cooling the specimens.

A micro-pattern consisting of parallel lines oriented at a 45° angle to the longitudinal direction of the ceramic beams is applied (see Figure 5.1a). The macro-pattern features a hexagonal shape with a 5 mm side length, extending through the entire ceramic thickness (see Figure 5.1b). The micro-patterns, designed for precise surface engraving of alumina, achieve a targeted depth of 20 µm in a single laser pass. Both the kerf width and the spacing between the micro-patterns are 200 µm.

To prevent misalignment during the lamination process, high-temperature resistant tape, such as Polyimide tape, is applied to the laser-machined surfaces of the ceramic tiles. Four laminated ceramic beam types are fabricated: Face-to-face (FF), Back-to-back (BB), Side-up (SU), and Side-

down (SD). Each beams comprised two layers of ceramic tiles with same engraved hexagons pattern and a single intermediate Surlyn® layer (see Figure 5.1c). One group of the ceramic beams is fabricated with micro-patterns, while the other beams are created without micro-patterns. The components are assembled using a vacuum bag method and subjected to a 5-hour heat treatment at 146 °C to ensure proper material bonding and achieve desired properties (see Figure 5.1d). Interfacial bonding between soft (Surlyn) and hard (alumina) components is crucial in bioinspired ceramic composites. Also, the thickness of Surlyn significantly influences the interfacial and structural properties. Recognizing its importance, we have dedicated a separate study to investigate the interfacial properties of these materials [124]. To ensure precise control over the thickness, metal shims were employed during the vacuum bagging and curing process in the oven. Post-manufacturing evaluation using microscopic imaging confirmed that the Surlyn thickness was consistently around 100 μm. It is worth noting that, for each type of experiment in this study, five samples are meticulously fabricated and tested to achieve the desired level of consistency.

5.3.2 Experimental Test Configuration

All specimens undergo 3-point bending tests with a fixed span length of 80 mm (based on ASTM D790, see Figure 5.1e). In the static mode, a constant displacement control is applied at a rate of 1.3 mm/min until a predetermined deflection of 12 mm is achieved. Conversely, the cyclic mode employed a combined control strategy. During the loading phase, a displacement rate of 6 mm/min is maintained for 1 mm per cycle for a total of 12 cycles. To capture the hysteretic behavior of the specimens under cyclic loading, the control mode transitioned to load control during the unloading step. This combined approach facilitates a more comprehensive assessment of the material's response under varied loading conditions, encompassing both static and cyclic regimes.

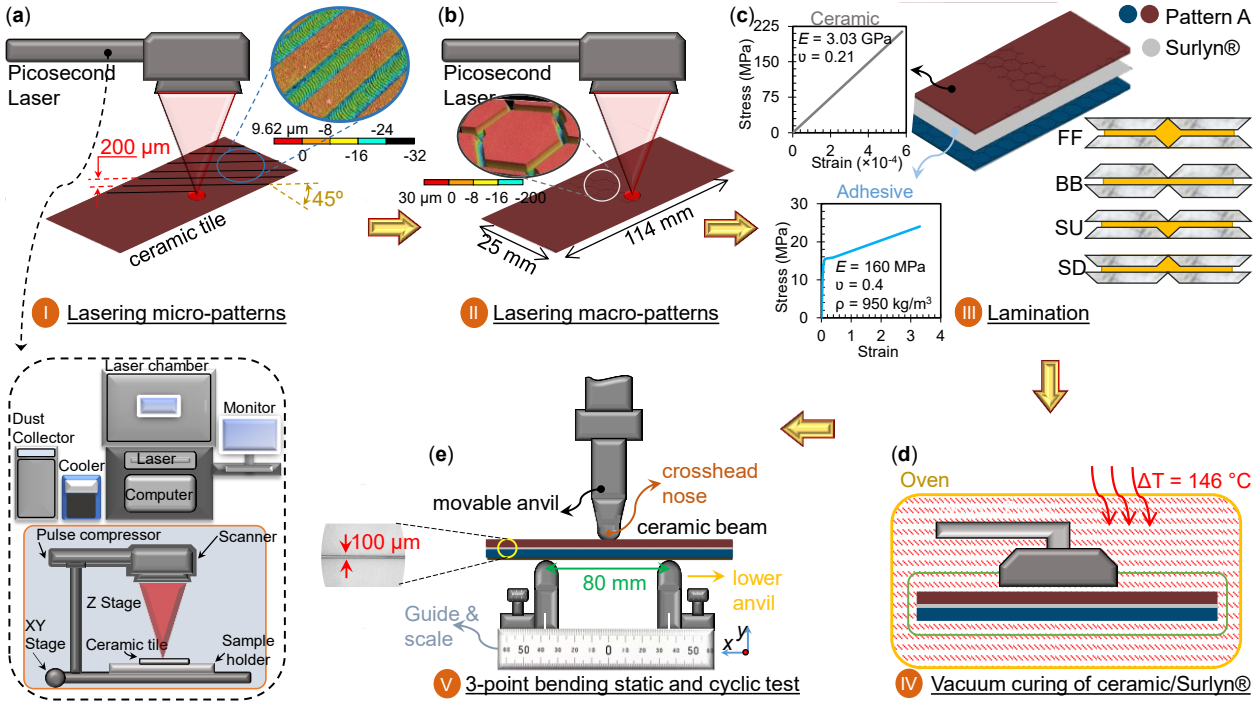

Figure 5.1. The manufacturing process of the bi-layer architectured ceramic beams: (**a**) Micro-patterning of ceramic tiles using the picosecond laser and subtractive manufacturing platform, (**b**) Macro-patterning of ceramic tiles using the picosecond laser, (**c**) Lamination of ceramic tiles and commercial monomer Surlyn with different stacking sequences (Back-to-back (BB), Side-down (SD), Side-up (SU), and Face-to-face (FF)), (**d**) Vacuum bagging and curing of ceramic composite beams, and (**e**) Configuration for static and cyclic 3-point bending tests.

5.4 Results and Discussion

While multi-layer composites offer advantages in energy absorption and failure mechanisms, this study focuses on the impact of patterns and stacking sequences (Back-to-back (BB), Side-down (SD), Side-up (SU), and Face-to-face (FF)) in bilayer ceramic structures, aligning with their primary application. Here, interfacial energy consumption dominates due to the focus on two-layer interactions. The key parameters analyzed were maximum load, flexural stiffness, and energy absorption. The area under the force-displacement curves represents the energy absorbed by the structures in the static analysis, while the loop area signifies the energy absorbed in the cyclic analysis.

5.4.1 Static Loading

The architectured ceramic beams underwent 3-point bending static load testing to assess the influence of stacking sequences as well as micro-patterns on their mechanical performance.

v. Effect of stacking sequence

Figure 5.2 illustrates the static 3-point bending mechanical performance of the architectured ceramic beams featuring different stacking sequences (BB, SD, SU, and FF) along with micro-patterns. Figure 5.2a and b depict the force-deflection curves of the architectured ceramics with varying stacking sequences, both without and with micro-patterns, respectively.

Back-to-Back (BB): The force-deflection curve for Ceramic BB exhibits a steep rise to peak load, indicating high stiffness. However, it also shows a sharp drop after peak load, suggesting a brittle failure mode.

Side-Down (SD): Ceramic SD shows a lower strength compared to BB. However, it can sustain its load longer before failing, demonstrating a more ductile behavior with increased energy absorption.

Face-to-Face (FF): Ceramic FF displays the lowest stiffness and peak load among the sequences. This indicates it is likely the weakest in terms of load-bearing capacity but exhibits prolonged deflection before failure, implying a ductile behavior.

Side-Up (SU): Ceramic SU falls between SD and FF in terms of stiffness and peak load. It shows characteristics of moderate stiffness and energy absorption, indicating an intermediate behavior between brittle and ductile.

These trends in the stacking sequences' effects on mechanical properties remain consistent when micro-patterns are introduced to the architectured ceramics.

The variation in mechanical performance among different ceramic configurations with different stacking sequences can be attributed to their structural characteristics and the sizes of the polymer-rich areas:

Ceramic FF features a larger polymer (soft) rich area compared to Ceramic BB, with stiff/soft ratios of 0.86 and 6.25, respectively. This results in Ceramic FF exhibiting polymer-like behavior characterized by lower stiffness and slower crack propagation, leading to a plateau (see Figure 5.2a and 3a). Conversely, Ceramic BB, with a smaller polymer-rich area (see Figure 5.3b), displays a

stiffer configuration and quicker degradation, indicative of a more brittle material. In the case of Ceramic BB, the hard phase primarily dictates the mechanical behavior of the composite ceramic system, whereas for Ceramic FF, the soft phase plays a more dominant role. The stiff/soft ratios (0.86 and 6.25) correlate well with their respective flexural stiffness values (2.4 to 16 N/mm). This is supported by studies showing that the ratio of soft to stiff components significantly affects the mechanical behavior of bioinspired composites [61,125].

Although these composites do not follow an exact rule of mixture due to differences interface topologies, the interaction between the alumina tiles and Surlyn varies, leading to different mechanical behaviors. As seen in Figure 5.2, the SU and SD specimens exhibit mechanical performance between that of Ceramics BB and FF due to their intermediate polymer-rich area sizes (see Figure 5.2c and 3d). Despite having the same stiff/soft ratio (1.5), Ceramic SD shows higher stiffness and more brittle behavior compared to Ceramic SU, which displays more plastic deformation. This difference is attributed to the more intense interaction between ceramic tiles in the compression zone of Ceramic SD.

vi. Effects of micro-pattern

Figure 5.2c presents the maximum load, flexural stiffness, and energy absorption of the ceramics under static load, both with and without micro-patterns. The data clearly indicate that the presence of micro-patterns significantly enhances the mechanical performance of the ceramic beams across all stacking sequences.

*Energy absorptio*n: Micro-patterns play a crucial role in enhancing energy absorption by providing pathways for crack deflection and energy dissipation. For instance, the energy absorption of Ceramic FF increases by up to 140%. This improvement can be attributed to the ability of micro-patterns to interrupt crack propagation and facilitate energy dissipation mechanisms, such as multiple crack deflections and branching. Studies have shown that similar microstructural modifications can enhance energy absorption in ceramics and composite materials [87,126].

Maximum load: The incorporation of micro-patterns results in a substantial increase in the maximum load across different stacking sequences. Specifically, Ceramics SD and FF exhibit notable enhancements in maximum load, with increases up to 140% and 130%, respectively. This can be explained by the enhanced interfacial bonding provided by the micro-patterns, which leads to a more cohesive and robust structure. These findings are in line with recent studies indicating

that micro-patterning improves load-bearing capacity by enhancing load transfer efficiency and delaying crack initiation [127,128].

Flexural stiffness: Micro-patterns also contribute to significant improvements in flexural stiffness. Ceramics FF and SD demonstrate notable increases in stiffness with the introduction of micro-patterns, up to 300% and 80%, respectively. The optimized stress distribution facilitated by the micro-patterns helps to disperse stresses more evenly, reducing the risk of localized failure and enhancing overall stiffness. This phenomenon is consistent with findings from other research, where micro-patterning has been shown to improve the mechanical properties of ceramics and composites [41,129].

Several factors contribute to the observed enhancements in mechanical properties:

Enhanced interfacial bonding: Micro-patterns promote stronger bonding between individual ceramic units. This improved bonding results in a more cohesive and robust structure, contributing to increased maximum load and energy absorption. This is supported by studies that show enhanced interfacial interactions due to patterned surfaces, leading to improved mechanical performance [101,130].

Optimized stress distribution: Specific micro-patterns optimize stress distribution within the material. By dispersing stresses more evenly, the risk of localized failure is reduced, leading to an overall improvement in strength and stiffness. This optimized stress distribution is corroborated by studies demonstrating the beneficial effects of micro-patterning on stress distribution and mechanical properties [131,132].

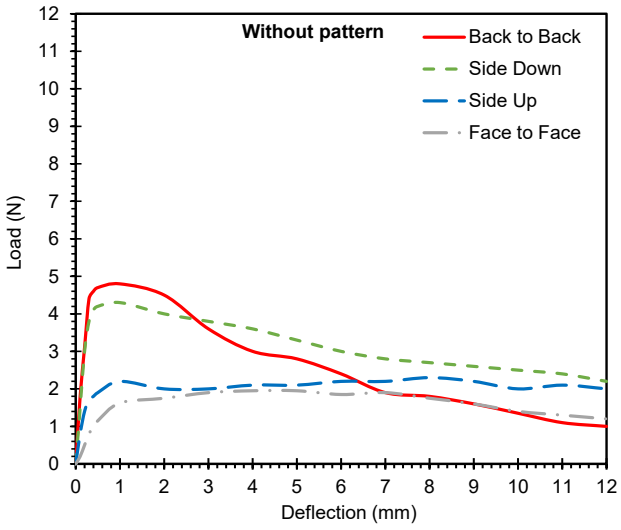

(**a**)

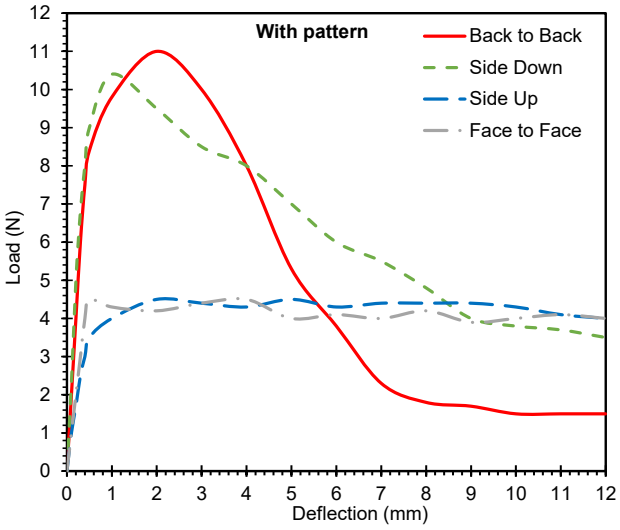

(**b**)

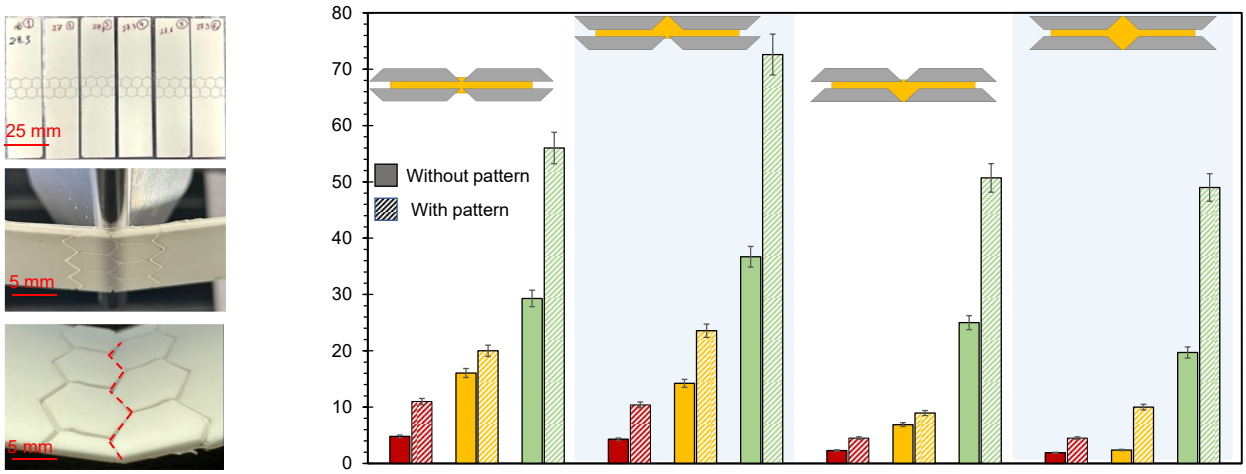

	Back to Back	Side Down	Side Up	Face to Face
Max Load (N) (non-pattern/**pattern**)	4.8 / **11**	4.3 / **10.4**	2.3 / **4.5**	1.9 / **4.5**
Flexural Stiffness (N/mm) (non-pattern/**pattern**)	16 / **20**	14.2 / **23.6**	6.9 / **8.9**	2.4 / **10**
Energy Absorption (N.mm) (non-pattern/**pattern**)	29.3 / **56**	36.7 / **72.6**	25 / **50.7**	19.7 / **49**

(**c**)

Figure 5.2. Static 3-point bending mechanical performance of the architectured ceramic beams with different stacking sequences (Back-to-back (BB), Side-down (SD), Side-up (SU), and Face-to-face (FF)) and micro-patterns: (**a**) Force-deflection curves of the ceramics with different stacking sequences without micro-patterns, (**b**) Force-deflection curves of the ceramics with different stacking sequences with micro-patterns, and (**c**) Maximum load, flexural stiffness, and energy absorption of the ceramics under static load with and without micro-patterns.

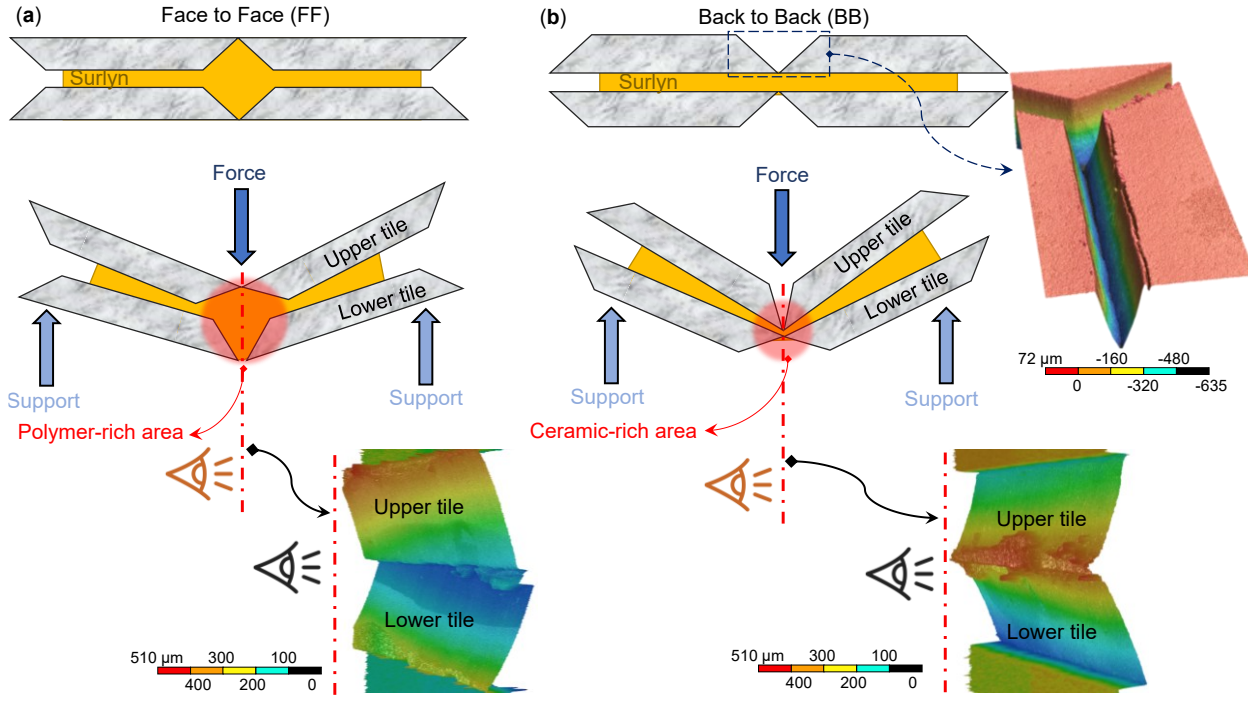

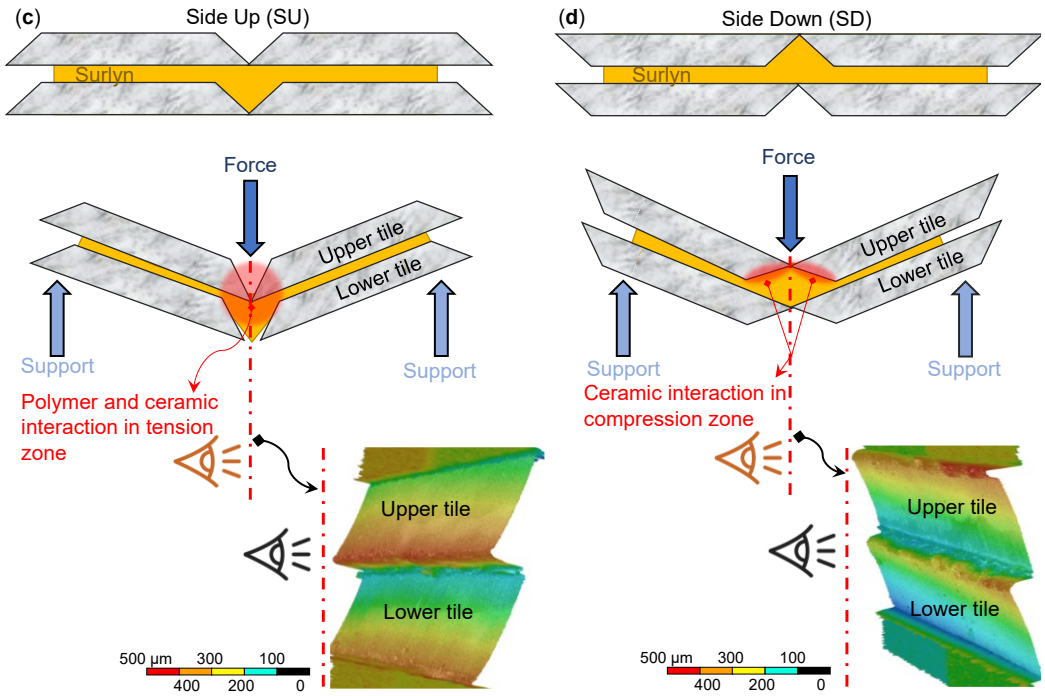

Figure 5.3. Multilayered ceramic configurations with different stacking sequences and microscopy images: (**a**) Face-to-face configuration (FF), (**b**) Back-to-back configuration (BB), (**c**) Side-up configuration (SU), and (**d**) Side-down configuration (SD).

5.4.2 Cyclic Loading

The architectured ceramic beams were subjected to 3-point bending cyclic load testing to evaluate how stacking sequences (BB, SD, SU, and FF) and micro-patterns influence their mechanical performance.

i. Effect of stacking sequence

Figure 5.4 presents the hysteresis force-deflection curves of architectured ceramic beams with different stacking sequences (BB, SD, SU, and FF) without micro-patterns. Additionally, Figure 5.4 displays the total energy absorption and flexural stiffness of each cycle within the material during the loading and unloading cycles (totaling 12 cycles). The stacking sequence appears to have a notable impact on the initial stiffness, peak force, and energy absorption of the ceramic under cyclic loading:

Initial stiffness: Ceramic BB exhibits the highest initial stiffness (indicative of its high rigidity and load-bearing capacity), followed by Ceramics SD, SU, and FF for the first cycle as shown in Figure 5.4a.

Stiffness degradation: As the cyclic progresses, all ceramic configurations experience a decrease in stiffness, except for Ceramic FF. Ceramic FF maintains a relatively consistent stiffness throughout the cycles (suggesting enhanced durability).

Cyclic behavior: By the final cycle (No. 12), the stiffness of all ceramic configurations converges to nearly the same value.

The hysteresis loops of the ceramics provide valuable insights into their energy dissipation and cyclic behavior (see Figure 5.4b):

Ceramic SD: Displays larger hysteresis loops compared to the others, indicating potentially higher energy dissipation. However, it's important to note that larger loops can also signify increased damage within the material.

Ceramic BB: Follows Ceramic SD with relatively large hysteresis loops, suggesting significant energy dissipation as well. Initially absorbs energy efficiently during the first 5 cycles (highlights its initial strength and energy absorption capacity) compared to other configurations. However, Ceramic BB loses its energy absorption ability quickly as the cycles progress indicating potential limitations in long-term energy absorption and durability.

Larger hysteresis loops in Ceramics SD and BB indicate their ability to dissipate more energy during cyclic loading. While this suggests enhanced energy absorption, it's essential to consider the trade-off with potential material damage and degradation.

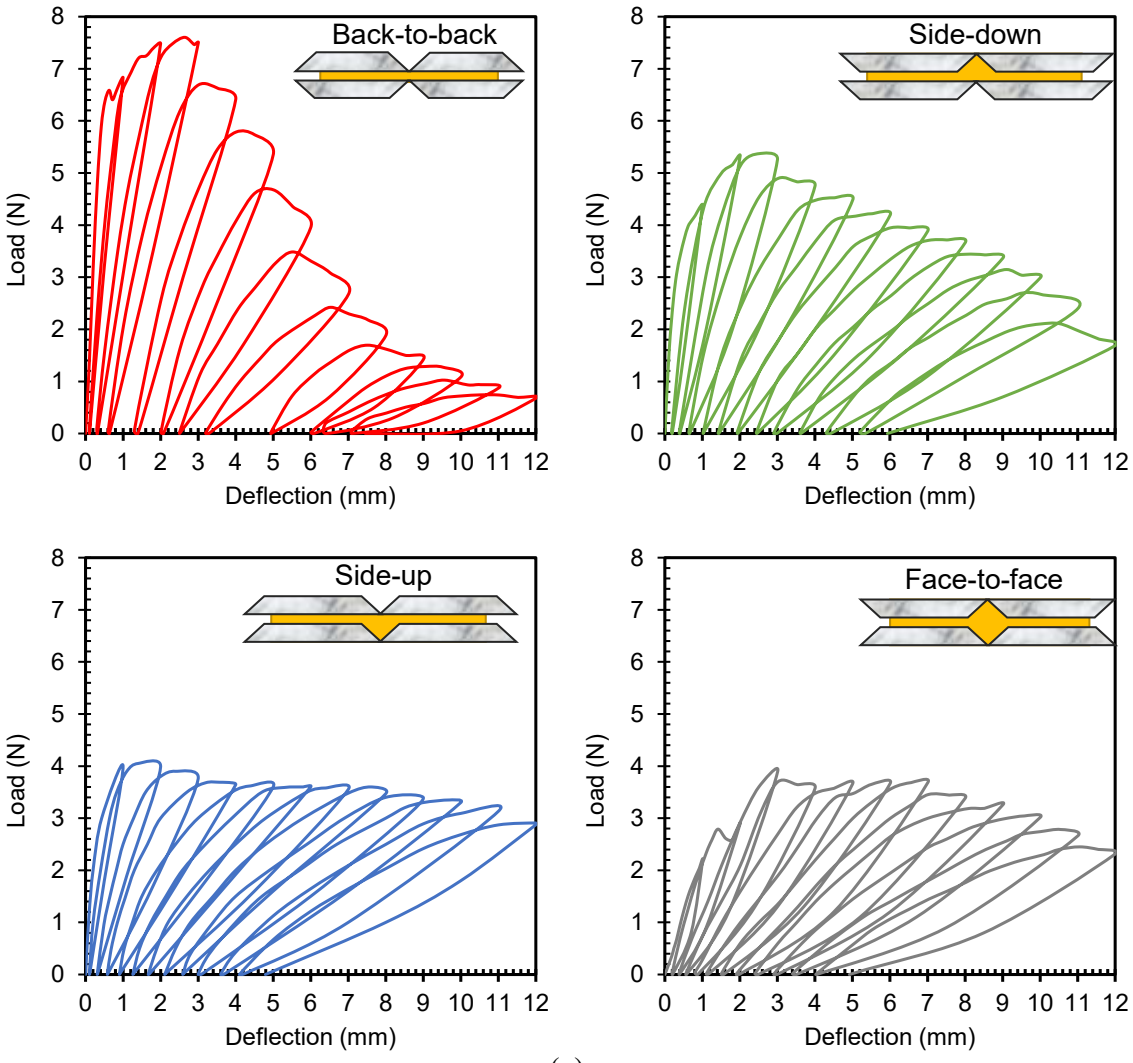
Back-to-back
Side-down
Side-up
Face-to-face
Load (N)
Deflection (mm)
0 1 2 3 4 5 6 7 8
0 1 2 3 4 5 6 7 8 9 10 11 12

(a)

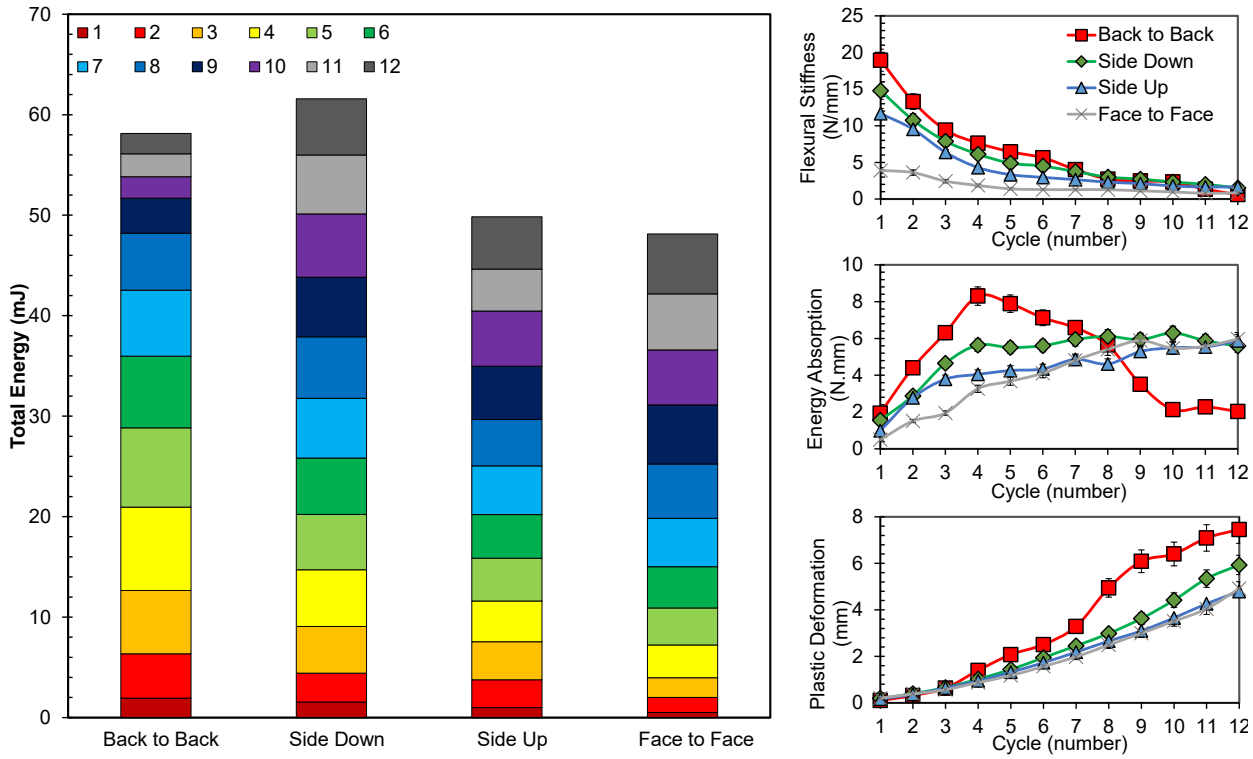

(**b**)

Figure 5.4**.** Cyclic 3-point bending mechanical performance of the architectured ceramic beams with different stacking sequences (Back-to-back (BB), Side-down (SD), Side-up (SU), and Face-to-face (FF)) without micro-patterns: (**a**) Hysteresis force-deflection curves of the ceramics with different stacking sequences, and (**b**) Total energy absorption as well as energy absorption, flexural stiffness, and plastic deformation of each cycle.

ii. Effects of micro-pattern

Figure 5.5 presents the hysteresis force-deflection curves of architectured ceramic beams with different stacking sequences (BB, SD, SU, and FF) with micro-patterns. Introducing micro-patterns on ceramic surfaces has generally enhanced the cyclic mechanical performance of the architectured multilayered ceramic beams, improving both energy absorption and stiffness. However, the extent of this improvement varies among different stacking sequences. Notably, micro-patterns had a significant impact on Ceramics FF and SU, where the mechanical characteristics were primarily influenced by Surlyn (which is mostly controlled by shear force). This accentuates their role in these enhancements. For instance, the total cyclic energy absorption for Ceramic FF increased by up to 85%, while for Ceramic BB, this improvement was only 14%, as depicted in Figure 5.5b.

There could be several reasons for the varying improvements in cyclic mechanical performance with the introduction of micro-patterns:

Interfacial bonding enhancement: Micro-patterns can promote better interfacial bonding between the ceramic units and the matrix material (Surlyn®), leading to improved load transfer and energy dissipation. This enhanced bonding is particularly beneficial for Ceramic FF, where the micro-patterns could facilitate stronger adhesion and interaction between layers (see Figure 5.5c).

Crack deflection and propagation: Certain micro-patterns, such as grooves or ridges, can act as crack arrestors, deflecting cracks and preventing their propagation [83,98]. This effect would be more pronounced in Ceramic FF, as it's configurations may benefit more from crack deflection mechanisms.

Stress redistribution: Micro-patterns can redistribute stress concentrations, preventing localized areas of high stress that could lead to premature failure [99–101]. Ceramics FF, SU, and SD, with their intricate micro-patterns, may show more significant improvements in stress redistribution compared to Ceramic BB.

Energy dissipation pathways: Micro-patterns create additional pathways for energy dissipation, allowing the material to absorb more energy before failure [98,126]. The unique patterns on Ceramic FF might offer more effective pathways for energy dissipation compared to other configurations.

Material toughening: Micro-patterns could induce toughening mechanisms within the ceramic-polymer composite, such as crack bridging or microcrack toughening [41,87,98,131]. Ceramic FF, with its specific micro-patterns, may exhibit more pronounced toughening effects, leading to increased energy absorption.

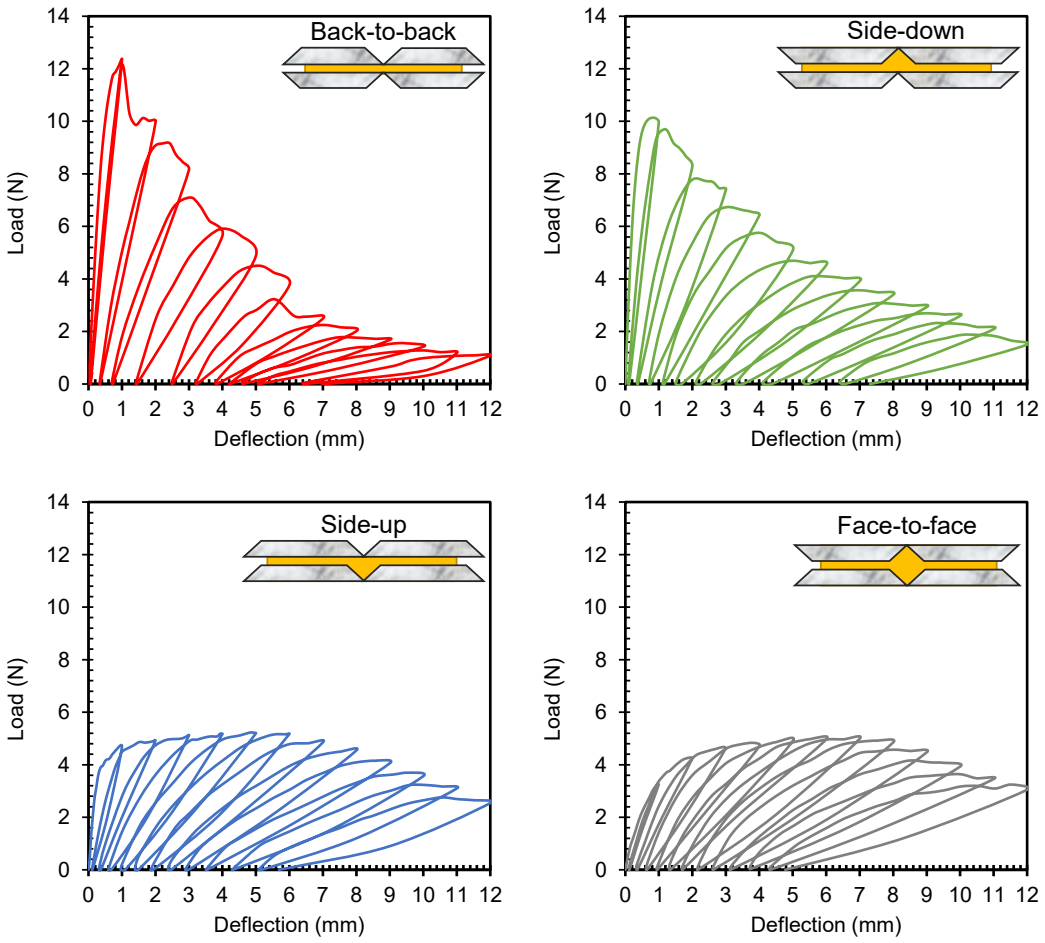
Back-to-back
Side-down
Side-up
Face-to-face
Load (N)
Deflection (mm)

(a)

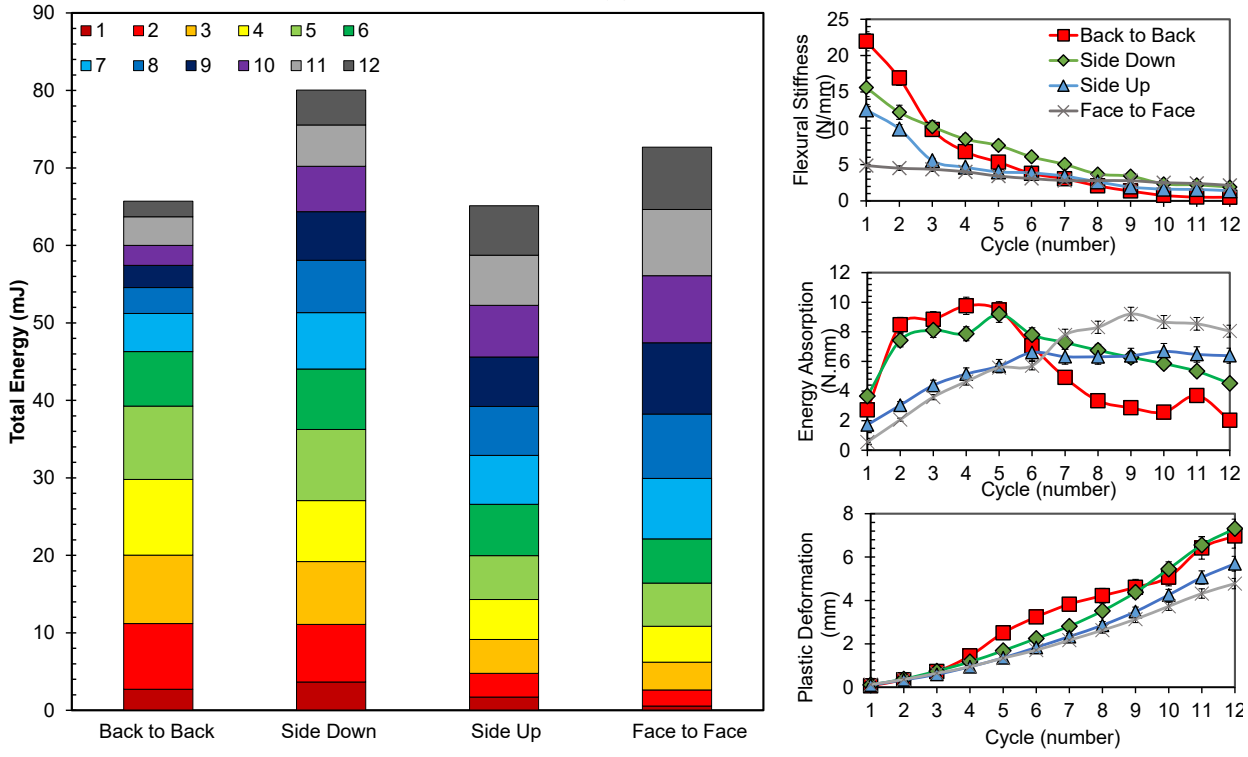
Total Energy (mJ)
1 2 3 4 5 6 7 8 9 10 11 12
Back to Back
Side Down
Side Up
Face to Face
Flexural Stiffness (N/mm)
Energy Absorption (N.mm)
Plastic Deformation (mm)
Cycle (number)

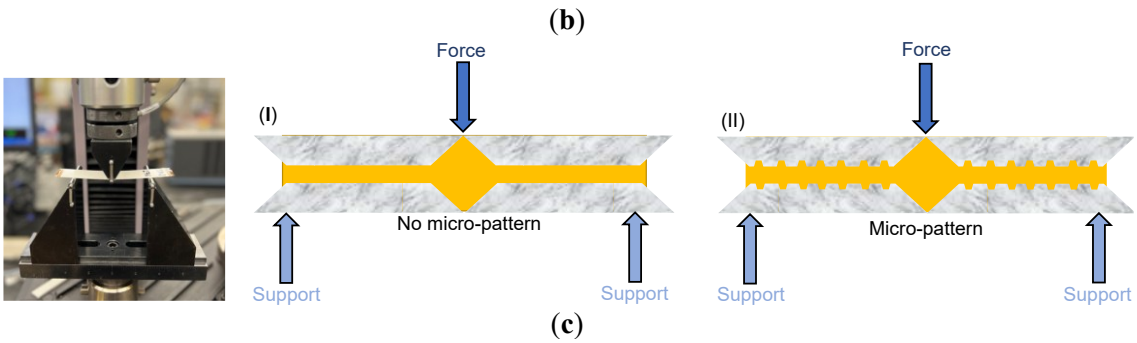

Figure 5.5. Cyclic 3-point bending mechanical performance of the architectured ceramic beams with different stacking sequences (Back-to-back (BB), Side-down (SD), Side-up (SU), and Face-to-face (FF)) with micro-patterns: (**a**) Hysteresis force-deflection curves of the ceramics with different stacking sequences, (**b**) Total energy absorption as well as energy absorption, flexural stiffness, and plastic deformation of each cycle, and (**c**) Schematic of micro-patterns in the multilayered ceramic systems: (I) No micro-patterns, and (II) With micro-patterns.

Following cyclic 3-point bending test, each ceramic system exhibited plastic deformation, quantifiable by the observed increase in residual deflection with each cycle (see Figure 5.4b and Figure 5.5b). Up to the third cycle, all ceramic groups, micro-patterned or not, displayed statistically indistinguishable levels of plastic deformation. However, beyond this point, Ceramics BB and SD underwent significantly greater plastic deformation compared to Ceramics FF and SU. This suggests enhanced energy dissipation mechanisms within Ceramics BB and SD, potentially accompanied by more pronounced damage accumulation. Conversely, Ceramics FF and SU, characterized by polymer-like mechanical behavior, exhibited higher durability and superior resistance to plastic deformation but displayed lower energy dissipation capabilities under cyclic bending. This trend persisted in the micro-patterned specimens, which displayed comparable levels of plastic deformation, but at demonstrably higher load capacities. This observation suggests an improvement in interfacial strength and stress distribution at the interface for micro-patterned specimens.

5.5 Conclusion

In this study, the static and cyclic flexural properties of bioinspired ceramic-polymer composites featuring brick-and-mortar architectures were investigated using an advanced

subtractive manufacturing platform enabled by ultra-short pulsed picosecond lasers. A range of macro and micro patterns were engraved onto alumina tiles, followed by the fabrication of ceramic-polymer composites by stacking laser-engraved tiles with interlayers of the commercial monomer Surlyn®.

The static results revealed a significant influence of macro and micro patterns as well as stacking sequences on the mechanical performance of the architectured ceramic beams (see Figure 5.6). Different stacking sequences exhibited distinct behaviors: Ceramic BB displayed high stiffness but brittle failure, Ceramic SD showed lower stiffness but prolonged load sustainability, Ceramic SU fell in between with moderate stiffness, and Ceramic FF exhibited the lowest stiffness but prolonged deflection before failure, suggesting a ductile behavior.

Introduction of micro-patterns significantly enhanced the mechanical properties of the architectured ceramic beams (see Figure 5.6). Across all stacking sequences, micro-patterns improved energy absorption, maximum load, and flexural stiffness. The enhancements were particularly pronounced in Ceramic FF, where total cyclic energy absorption increased by up to 85%. This improvement can be attributed to the pathways for crack deflection, improved interfacial bonding, optimized stress distribution, and enhanced energy dissipation provided by the micro-patterns.

The cyclic behavior of the architectured ceramic beams provided valuable insights. Ceramic FF demonstrated the most stable behavior over 12 cycles, indicating potential durability and fatigue resistance. Ceramics SD and BB exhibited larger hysteresis loops, indicating higher energy dissipation potential but also potential for increased material damage. Ceramic BB initially showed efficient energy absorption but lost this capability quickly over cycles, highlighting the need for balanced energy absorption and material durability in cyclic loading applications.

In conclusion, the findings reveal a nuanced relationship between stacking sequence and properties such as stiffness, energy absorption, and ductility. Ceramic BB exhibited high stiffness and load-bearing capacity but tended towards brittle failure, making them suitable for applications where rigidity is crucial. Ceramic SD showed enhanced energy dissipation and ductility, making them ideal for impact resistance. Ceramic FF, with lower stiffness but prolonged deflection before failure, is promising for applications prioritizing energy absorption. Ceramic SU balanced stiffness and ductility, offering versatility. The addition of micro-patterns yielded further enhanced properties, with improvements observed in energy absorption, maximum load, and interfacial

bonding across all configurations. Notably, for Ceramics FF and SU, where mechanical properties were primarily dictated by Surlyn, the micro-patterns played a more significant role in these improvements. This study highlights the potential for tailoring ceramic properties for diverse applications, from aerospace to automotive, through careful selection of stacking sequences and micro-patterns.

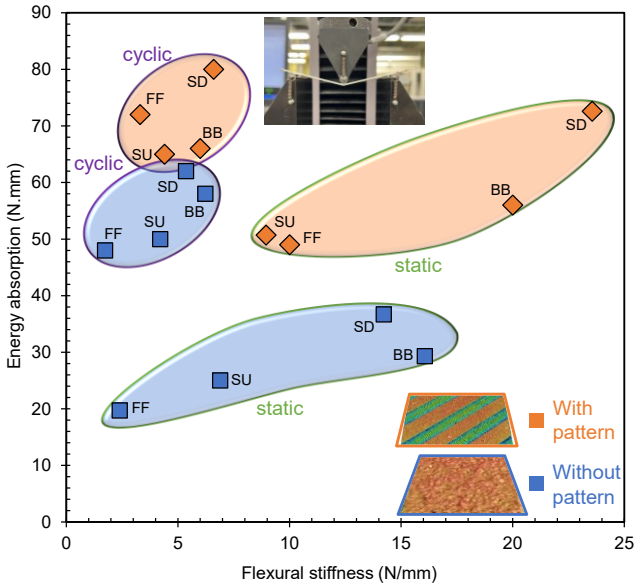

Figure 5.6. Material performance: Energy absorption versus flexural stiffness for the multilayered architectured ceramic beams under 3-point static and cyclic bending loads with and without micro-patterns and different stacking sequences (Back-to-back (BB), Side-down (SD), Side-up (SU), and Face-to-face (FF)). Energy absorption is calculated as the sum total of energy absorbed over 12 cycles, while the average stiffness is determined as the stiffness value across the cycles.

Chapter 6:

Bioinspired Programmable Multi-scale Surface Architectures for Toughening Ceramic–Polymer Composites

Throughout our research journey in the field of bioinspired ceramic composites—detailed in the previous chapters—we have gained valuable insights that enabled the development of programmable and tunable composites with customizable mechanical properties. We discovered that micro-patterning significantly enhances interfacial properties between ceramic and polymer phases by introducing additional energy absorption mechanisms. Similarly, hexagonal macro-patterns were found to markedly influence the structural behavior of the composites. Our experimental findings indicate that partially cut hexagonal configurations offer higher flexural stiffness, making them well-suited for load-bearing applications, while fully cut designs exhibit superior energy dissipation, ideal for impact-resistant structures. Additionally, in laminated bioinspired ceramics, we demonstrated that cell geometry and mechanical behavior can be tailored through the stacking sequence of the ceramic layers. For instance, the side-up (SU) configuration provided a desirable balance between stiffness and ductility, enhancing design versatility. Building on these foundations, in this chapter, we investigates the performance of various bioinspired ceramic designs under impact loading conditions. We anticipate that each design will exhibit distinct energy absorption and damage progression mechanisms, leading to diverse mechanical responses under dynamic loading.

This work has been submitted in:

Ehsan Azad, Hamidreza Yazdani Sarvestani, Meysam Rahmat, Marc Genest, Behnam Ashrafi1, Farjad Shadmehri, Mehdi Hojjati (2025), Bioinspired Programmable Multi-scale Surface Architectures for Toughening Ceramics. Materials Horizons

6.1 Abstract

Nature's protective materials, such as nacre, achieve exceptional toughness through hierarchical designs that integrate structural features and interfacial mechanisms across multiple scales. Inspired by these functional principles, we present a digitally programmable laser micromachining strategy to fabricate multi-scale surface architectures on ceramic–polymer composites. By integrating full-depth hexagonal macro-patterns with shallow diagonal micro-patterns into alumina–Surlyn® laminates, we engineer surface features that simultaneously enable crack deflection, bridging, and enhanced interfacial bonding. The combined patterned configuration absorbs nearly twice the energy of unpatterned ceramics under 20 J low-velocity impacts and exhibits superior resilience under repeated 2 J impacts. Post-impact X-ray radiography with zinc iodide and rebound-based performance analysis reveal reduced delamination and elastic recovery in patterned samples, confirming the role of multi-scale patterning in controlling crack evolution and energy dissipation. Unlike conventional bioinspired designs that replicate only macrostructural forms, this work demonstrates how scalable surface patterning can actively tailor failure pathways across interfaces and within the ceramic phase. These results establish a new pathway for toughening brittle systems through hierarchical pattern integration, offering a promising design approach for impact-resistant materials in extreme environments.

6.2 Introduction

Natural armors exhibit a fascinating array of structural strategies evolved to enhance protection. For example, the deer skull distributes impact forces across a broad area to reduce localized damage [13], the mantis shrimp's dactyl club employs a hierarchical multilayered architecture for exceptional toughness, and abalone shells rely on overlapping layers to form flexible, energy-dissipating shields [83,133–135]. Among these, nacre — also known as mother of pearl — is particularly renowned for its toughness, achieved through a hexagonal tile arrangement that promotes crack deflection and bridging, enabling efficient energy dissipation. In addition to their architecture, the interface design in these biological systems plays a critical role in their mechanical performance. Studies have highlighted that the interfaces between soft and rigid components in natural armors are often rough, wavy, or undulating, creating localized heterogeneities that improve interfacial toughness [22,89,90,93,136]. These fine-scale features are key to promoting energy absorption by encouraging plastic deformation, delaying crack

propagation, and redirecting interfacial cracks [86,95,98,137]. Such hierarchical and interfacial designs serve as valuable models for the development of engineered materials with enhanced protective properties [114,124,138].

Bioinspired ceramics are synthetic materials designed to emulate these natural strategies by incorporating the essential architectural features of natural armors into engineered systems [7,12,15]. For example, the layered brick-and-mortar structure inspired by nacre improves energy absorption and fracture resistance by mimicking the staggered, interlocking arrangement of tiles and mortar. This configuration enables effective stress transfer and restricts catastrophic failure under impact [139–141]. Similarly, hierarchical structures based on the mantis shrimp's dactyl club have been replicated to achieve high toughness and damage tolerance through multi-layered architectures that control crack paths and absorb energy efficiently. These natural strategies provide a blueprint for developing engineered ceramics with enhanced impact performance through programmable multi-scale designs (see Figure 6.1) [116,142–144].

In recent years, advanced manufacturing techniques such as tape casting, spark plasma sintering, 3D printing, and freeze casting have enabled the fabrication of complex geometries that emulate macro-scale natural designs [145]. These methods have made substantial progress in replicating the overall form and structure of biological systems. However, they still face considerable challenges in accurately reproducing multi-scale features, particularly at the micro-pattern level [146,147]. While macro-scale architectures can be manufactured with reasonable precision, fine microstructural details such as those critical to interfacial strength and crack control in biological materials, remain difficult to replicate due to limitations in resolution, tool control, and repeatability [148]. This persistent gap between macrostructural fabrication capabilities and microstructural precision highlights the need for innovative approaches that can simultaneously control multiple length scales [8,149–152].

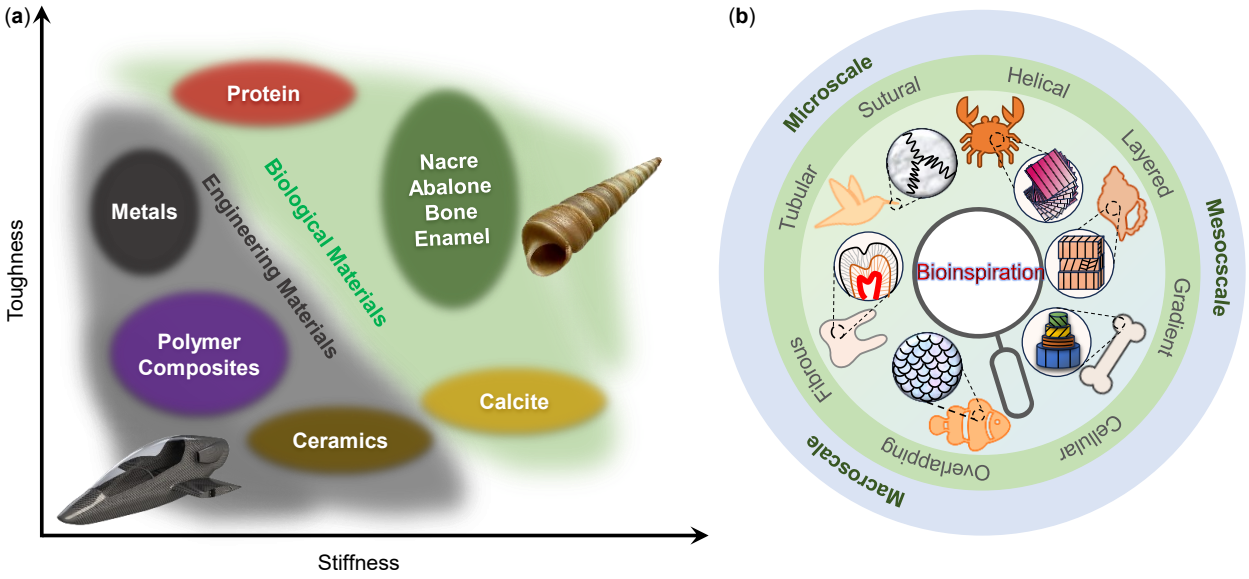

Figure 6.1. Bioinspiration in engineering and biological materials: (**a**) Engineering materials typically show reduced toughness with increasing stiffness, whereas biological materials can retain both properties; (**b**) Hierarchical architectures in biological systems inspire advanced ceramic designs, incorporating features such as hexagonal, diagonal, helical, and layered structures.

To address this challenge, we developed a programmable laser micromachining platform using high-precision picosecond pulses to fabricate multi-scale bioinspired surface architectures, including full-depth hexagonal macro-patterns and shallow diagonal micro-patterns. Applied to multilayered alumina-based ceramics with Surlyn® interlayers, this approach enables high-fidelity patterning of rigid–soft interfaces akin to those in nacre. Four laminate configurations — Plain, micro-patterned (MP), hexagonal (Hex), and combined MP-Hex — were fabricated and tested. Low-velocity impact experiments were conducted to evaluate energy absorption, failure mechanisms, and damage progression under both single-hit (20 J) and double-hit (2 J) loading. Post-impact analysis using X-ray radiography (with and without zinc iodide penetration) and 3D confocal microscopy enabled correlation of mechanical behavior with internal damage evolution. This study captures the key functional principles of nacre — namely, interfacial toughening and layered energy dissipation — without replicating its microstructure, while recognizing the differences in scale, material composition, and fabrication approach.

6.3 Materials and Methods

1.1. Design and Manufacturing

The primary rigid component in this study comprises high-precision square alumina ceramic tiles (Product No. 8462K43, McMaster-Carr) with a purity of 96–99.8% Al_2O_3 and a density of 3875 kg/m^3. Each tile measures 114 × 114 mm^2 and has a thickness of 635 µm. Alumina was selected for its high hardness, thermal stability, and wear resistance, making it suitable for applications demanding durability in extreme environments. The soft phase of the composite consists of a 100 µm thick Surlyn® thermoplastic film, chosen for its excellent impact resistance, flexibility, and strong adhesion to ceramic surfaces. A recent study has shown that monomer Surlyn® is particularly effective as an interface material in ceramic–polymer systems [10,144]. Surlyn® is an ionomer and a transparent thermoplastic resin that adheres well to ceramics and undergoes large-strain failure via ligament formation — a mechanism similar to protein behavior in nacre. It exhibits an elastomeric response with strain stiffening at the interface, which delays fracture localization and promotes distributed deformation. These properties are critical for enhancing toughness, energy absorption, and interfacial performance under flexural and impact loading.

To fabricate the multi-scale surface patterns, an Ytterbium picosecond fiber laser (YLPP-25-3-50-R, IPG Photonics, USA) was used to engrave both micro- and macro-scale features onto the ceramic tiles. This high-precision system prevents thermal damage and enables intricate patterning. The micromachining process was conducted in a controlled environment using an Aerotech electronic XY linear stage for precise movement and a manual Z stage for depth control. A Keyence IL-300 laser displacement sensor ensured accurate height calibration, while a compressed conical air nozzle was used to clear debris and cool the surface, enhancing both machining precision and safety (see Figure 2a). Building on previous research [86,124,153], a parametric study was conducted to determine the optimal laser settings for both the hexagonal macro-patterns and diagonal micro-patterns. The hexagonal macro-pattern consisted of 5 mm side-length hexagons engraved through the full thickness of the ceramic tiles. This geometry was selected based on both biological and engineering considerations: hexagonal tiling mimics the mineral architecture of nacre, where tile-like domains enhance toughness via crack deflection. Our prior optimization studies [10,15] showed that this shape and size provided the best balance between stress redistribution, mechanical segmentation, and manufacturability. Full-depth patterning was chosen

over partial-depth alternatives (e.g., 50% thickness) to ensure consistent segmentation of the ceramic layer and to fully engage tile-level energy dissipation mechanisms. Preliminary trials indicated that partial-depth cuts had limited influence, as they did not consistently redirect cracks or enable the interlayer bridging behavior observed with through-thickness patterns. In contrast, full-depth cuts formed well-defined weak planes that facilitated controlled crack deflection, enhanced interlayer interaction, and led to more reproducible mechanical responses under impact. The micro-patterns were designed to enhance interfacial bonding and promote mechanical interlocking, thereby improving energy absorption through crack deflection and distributed stress transfer at the interface. To disrupt crack continuity across layers, the micro-patterns were oriented at +45° in one layer and –45° in the adjacent layer, forming a 90° rotational offset reminiscent of Bouligand-like architectures (see Figure 2a). As shown in the inset of Figure 2a, cross-sectional microscopy confirmed that the Surlyn® thermoplastic successfully infiltrates the laser-engraved micro-patterns, further enhancing interfacial adhesion through mechanical interlocking and contributing to the improved mechanical performance observed during impact testing. Multilayered ceramics were assembled via vacuum bagging — a method known for producing uniform and void-free laminates. A total of four alternating layers of alumina tiles and Surlyn® films were stacked, sealed, and heat-treated at up to 146 °C for five hours to ensure strong bonding between layers. For the 4-layer ceramic system, two lasered tiles with the same engraved pattern but offset alignment — referred to as Pattern A and Pattern B — were stacked in an ABAB sequence to enhance interlayer interaction and avoid direct pattern overlap. To systematically investigate the effect of surface architecture on mechanical behavior, four distinct sample configurations were fabricated as follows:

(i) **Plain**: Four layers of unpatterned alumina tiles (no surface features).

(ii) **MP (Micro-Patterned)**: Four layers of alumina tiles engraved with shallow diagonal micro-patterns designed to enhance interfacial bonding.

(iii) **Hex (Hexagonal Macro-Patterned)**: Four layers of alumina tiles engraved with full-depth hexagonal macro-patterns intended to promote crack deflection and bridging.

(iv) **MP-Hex (Combined Micro- and Macro-Patterned)**: Four layers combining both shallow micro-patterns and full-depth hexagonal macro-patterns to leverage the advantages of both designs.

6.3.1 Experimental Test Configuration

For each configuration, six identical samples were tested to ensure statistical reliability. The low-velocity impact (LVI) behavior of multilayered ceramics is influenced by several parameters, including impactor size, boundary conditions, laminate thickness, and impact energy [154,155]. In this study, two types of LVI tests were conducted: high-energy single impacts and low-energy double-hit impacts, to comprehensively evaluate the mechanical performance and damage evolution of the ceramics. The high-energy LVI tests were performed according to the ASTM D7136 [156] standard using an Instron 9340 drop tower equipped with a 22 kN load cell. Each specimen was clamped using a 76 mm pneumatic fixture and impacted at its center by a 16 mm diameter hemispherical impactor with an energy of 20 J. A photogate sensor detected the impactor's motion just before contact, triggering the data acquisition system for precise recording. The collected data were used to determine the impactor's velocity, displacement, and energy throughout the test. The double-hit impact tests were carried out in accordance with ASTM D3763 [157] using a drop-weight impact testing machine. A 4.061 kg impactor with a 16 mm semi-spherical tip was employed. Unlike the high-energy setup, the specimens were unsupported, placed over a fixture featuring a 76 mm diameter hole aligned with the impactor's trajectory. Two separate impact events, each at 2 J, were performed at opposite diagonal points on the tile, each positioned 38.1 mm from the edges, to evaluate progressive damage (see Figure 6.2b). Load data were captured via a 22 kN piezoelectric load cell, and the impactor's velocity was measured using a photodetector-based velocity system.

6.3.2 Non-destructive Evaluation Techniques

Two non-destructive evaluation (NDE) methods were employed to investigate crack formation, delamination, and overall damage evolution in the multilayered bioinspired and plain ceramic samples following impact: X-ray radiography and X-ray radiography with zinc iodide penetrant.

X-ray Radiography: X-ray imaging was performed using a computed radiography system (CRx Vision) equipped with a high-resolution imaging plate. Scanning was conducted at a current of 4 mA, voltage of 80 kV, and an exposure time of 18 seconds. Radiographs were captured after

each impact event to detect internal cracks and delamination zones. This method provided baseline damage visualization in all sample configurations.

X-ray radiography with zinc iodide: To enhance the visibility of fine cracks and interfacial delamination, a zinc-based radiopaque penetrant was used in combination with X-ray inspection. The solution, consisting of zinc iodide, distilled water, and isopropyl alcohol, was applied dropwise to the impacted area and left for 10 minutes at room temperature to allow infiltration into damaged regions. Excess penetrant was carefully removed from the surface before imaging. This technique increased the contrast between fractured zones and intact material, revealing otherwise undetectable interfacial failures and highlighting the extent of delamination more clearly than the standard X-ray alone.

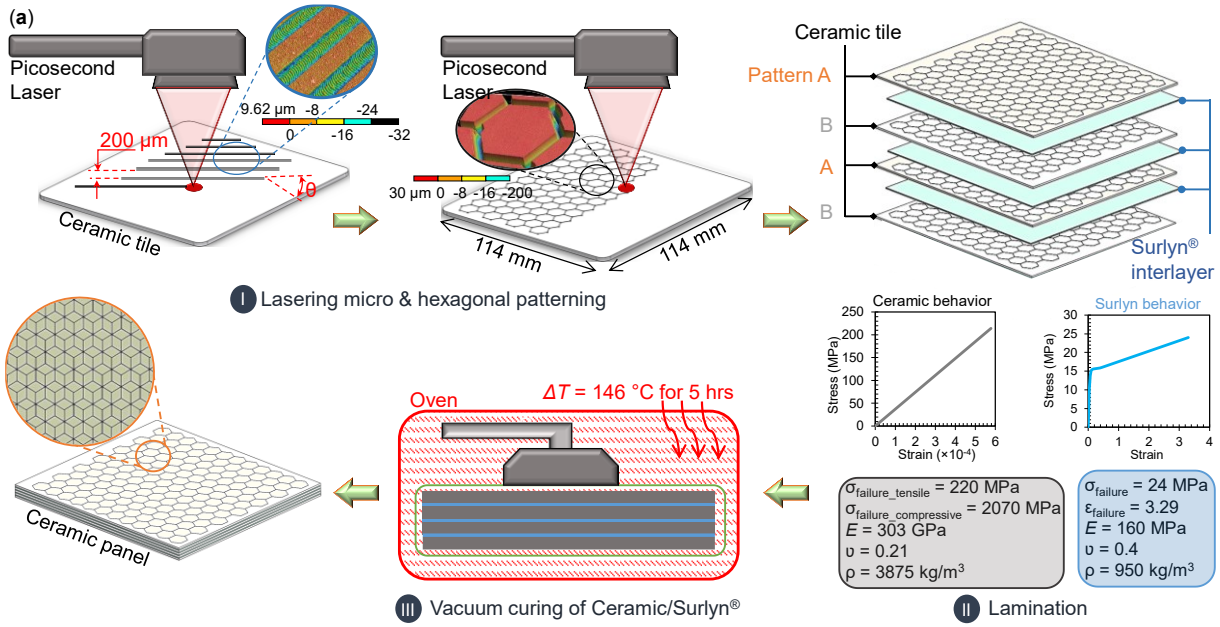

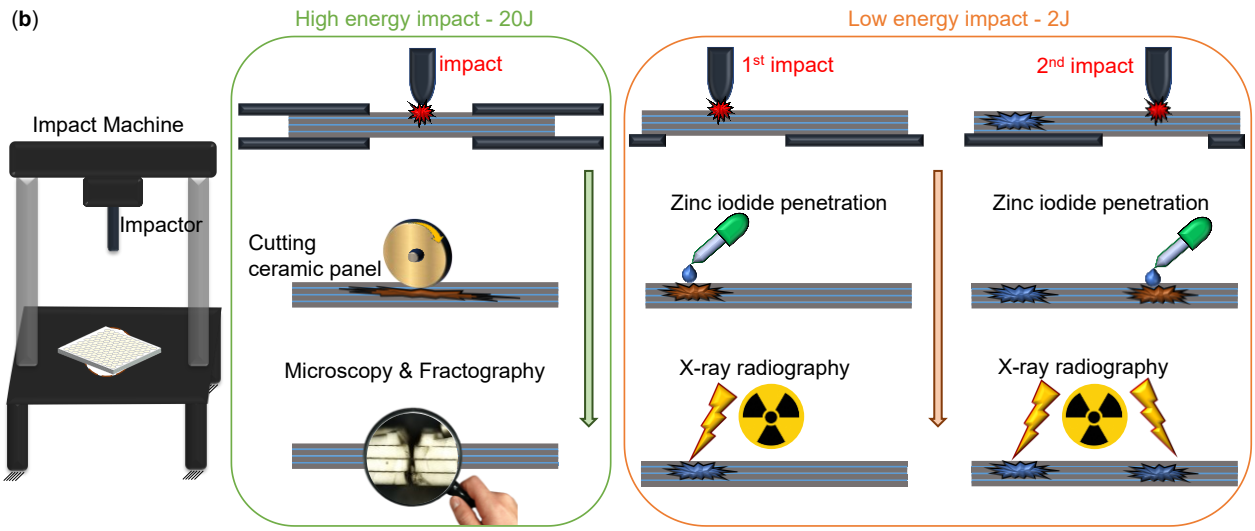

Figure 6.2. Experimental setup and manufacturing process of the bioinspired ceramics: (a) Fabrication process including hexagonal and micro-patterning of ceramic tiles using picosecond laser micromachining, followed by lamination with Surlyn® film, vacuum bagging, and heat curing; (b) Test configuration for high-energy and double-hit low-velocity impact tests, along with post-impact sample preparation steps for zinc iodide penetration and confocal microscopy analysis.

6.4 Results and Discussion

This section presents the experimental results analysis obtained from bioinspired ceramic laminates incorporating various surface architectures — specifically hexagonal macro-patterns, micro-patterns, and their combined configurations. The influence of each patterning strategy on mechanical performance, energy absorption, damage progression, and failure mechanisms under low-velocity impact is discussed in detail, with supporting insights from microscopy and radiographic evaluations.

6.4.1 Analysis of Patterns Engraving

Optimizing laser micromachining parameters is essential for achieving high-quality, functional micro-patterns on ceramic surfaces [32,123]. Several laser parameters — including power, scan speed, number of passes, pulse frequency, and wobble characteristics (shape, amplitude, and frequency) — were systematically calibrated to produce consistent patterns without causing thermal damage or microfractures in the alumina tiles [121,122]. The final parameters for both micro- and hexagonal patterns are summarized in Table 6.1. For the hexagonal pattern, a relatively high laser power of 50 W and 25 passes at a low scan speed (17 mm/s) were necessary

to achieve full-depth cuts (635 μm), penetrating through the entire tile thickness. The wobble amplitude of 0.3 mm at 800 Hz helped maintain smooth curve edges, ensuring clean pattern borders that promote effective crack deflection and interlocking during loading. In contrast, the micro-pattern required only a single pass with 24 W laser power and a higher scan speed (20 mm/s), resulting in shallow grooves, ~20 μm deep and 200 μm wide. These surface features were designed to enhance interfacial bonding by increasing the contact area and introducing mechanical interlocks at the alumina–Surlyn® interface.

Figure 6.3 shows the 3D laser scanning microscopy images obtained from a Keyence VK-X200 laser profiler, capturing the fine topography and surface profile of both pattern types. The hexagonal pattern exhibits a consistent channel width and full penetration through the tile, with clean vertical edges that are critical for effective layer separation during impact and crack bridging mechanisms. The micro-pattern, on the other hand, shows evenly spaced shallow grooves with smooth contours and no visible chipping or heat-affected zones, indicating excellent machining control. The difference in depth and geometry between the two patterns is not merely a fabrication outcome but a deliberate design strategy: while the hexagonal cuts promote controlled macrocrack propagation and energy dissipation via tile movement and bridging, the micro-pattern strengthens the interface and shifts failure from interfacial delamination to in-plane crack propagation within the tiles. Together, these results validate the precision of the laser micromachining setup and demonstrate how carefully tuned process parameters directly influence pattern integrity and function — laying the groundwork for improved mechanical behavior in the tested configurations.

Table 6.1. Optimized laser micromachining parameters for engraving micro- and hexagonal patterns on alumina tiles, including power, speed, number of passes, pulse frequency, and wobble characteristics.

Pattern Type	Laser power (W)	Linear speed (mm/s)	Number of passes	Pulse frequency (Hz)	Wobble pattern shape	Wobble amplitude (mm)	Wobble frequency (Hz)
Micro	24	20	1	1000	Circle	0.2	800
Hexagonal	50	17	25	1000	Circle	0.3	800

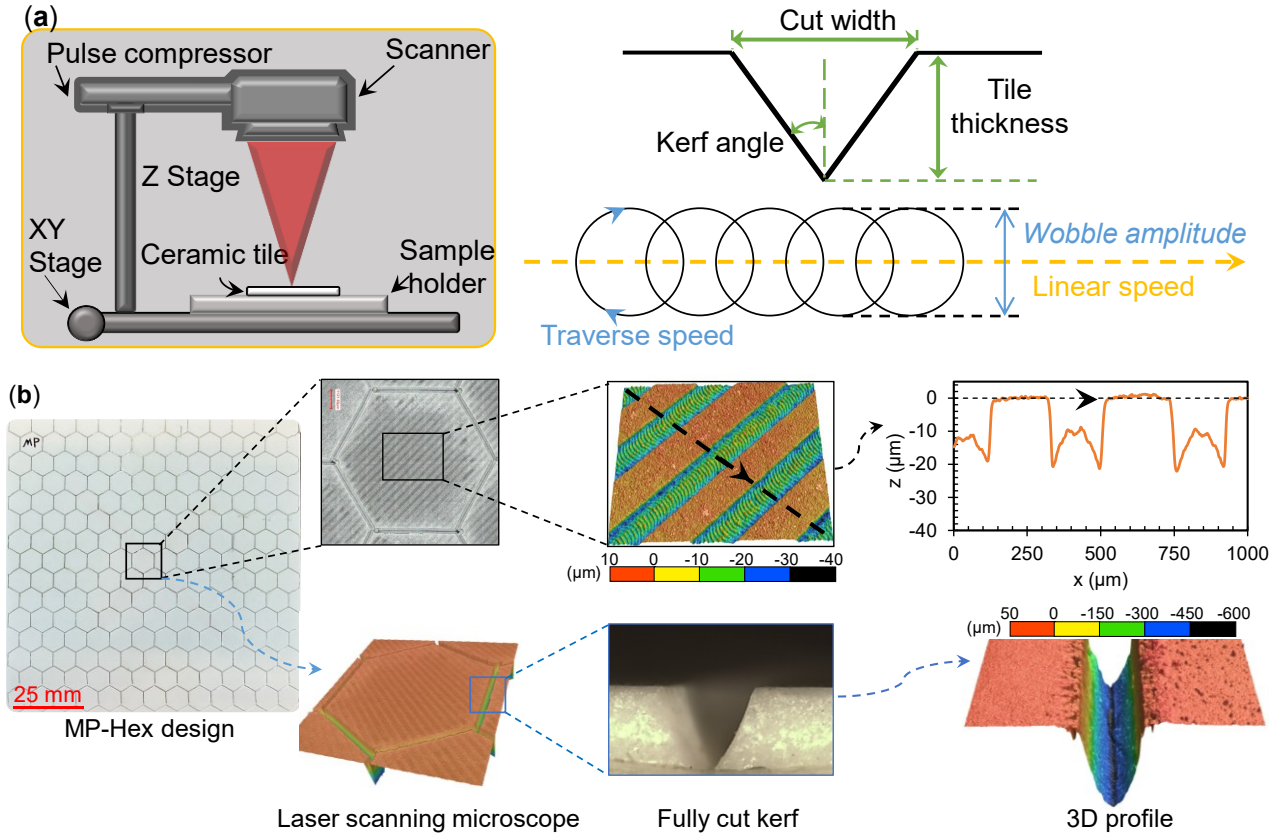

Figure 6.3. Fabrication and characterization of patterned ceramic tiles: (**a**) Schematic of the laser micromachining setup used to engrave macro- and micro-scale features, highlighting key processing parameters; (**b**) 3D laser scanning microscopy images and depth profiles of engraved patterns, including full-thickness hexagonal cuts and uniform shallow micro-grooves on the ceramic surface.

6.4.2 Pattern Influence on Mechanical Behavior

Low-velocity impact (LVI) testing at 20 J revealed distinct differences in the mechanical response of the four ceramic configurations: Plain, MP (micro-patterned), Hex (hexagonal-patterned), and MP-Hex (integrated patterns). The force–displacement curves (see Figure 6.4a) highlight the influence of surface architecture on stiffness, load-bearing capacity, and deformation prior to failure. The introduction of hexagonal patterns led to a substantial reduction in initial stiffness. While both the Plain and MP samples exhibited stiffness values of ~1050 N/mm, the Hex and MP-Hex samples dropped to ~610 N/mm — a ~42% reduction. This reduction is attributed to the full-depth hexagonal cuts that segment the ceramic layers and allow early localized

deformation. In contrast, the surface-confined micro-patterns preserved structural integrity and bulk stiffness, indicating that performance can be enhanced without sacrificing rigidity.

All patterned samples also showed a ~22% reduction in peak reaction force compared to the Plain sample (which reached 1894 N). While this reflects slightly lower maximum load capacity, it is outweighed by the marked improvements in energy absorption and damage tolerance. Differences were most evident in the deformation before perforation and total absorbed energy (Figure 6.4b). The MP sample exhibited the highest displacement (19 mm), nearly triple that of the Plain sample. The MP-Hex and Hex samples reached 15.8 mm and 12.3 mm, respectively. In terms of energy absorption, the MP-Hex sample absorbed the most energy (12.5 J), followed by MP (11 J) and Hex (10 J), all significantly higher than the Plain configuration. These results confirm that micro- and macro-patterns each contribute distinct benefits to impact performance, and their combination offers a synergistic advantage.

Post-impact analysis, supported by microscopy and visual inspection (Figure 4c–g), revealed key differences in damage morphology and failure mechanisms. In the Plain configuration, a localized circular hole developed at the impact site. Fractography showed two distinct brittle crack types, marked by numbered arrows in Figure 4: (1) vertical microcracks (Figure 4d) resulting from bending-induced tensile stresses on the bottom surface, and (2) diagonal cracks (Figure 4d) caused by in-plane shear stresses radiating from the impact site. In the Hex configuration, similar impact features were observed, but additional (3) crack-bridging mechanisms emerged (Figure 4g), where interlayer cracks connected ceramic layers along hexagonal boundaries. These bridging pathways delayed catastrophic failure by distributing crack propagation and enhancing energy dissipation.

The MP samples displayed a distinct failure mode, characterized by extensive macrocrack propagation and tile fragmentation. The damage spread widely across the sample, suggesting effective load transfer and interfacial strength. Microscopy confirmed that crack propagation occurred primarily around the kerfs of the micro-patterns, with both vertical and diagonal fracture paths forming. This distributed damage behavior is linked to the improved interfacial bonding facilitated by the micro-patterns, which increased contact area and mechanical interlocking with the Surlyn® layer. As a result, the entire tile network participated in resisting the impact, leading to substantially improved energy absorption.

In the MP-Hex configuration, both patterning strategies worked in concert. The micro-patterns enhanced interfacial adhesion and enabled macrocracks to extend throughout the tile network,

while the hexagonal grooves redirected microcracks and enabled crack bridging between layers. These simultaneous mechanisms created the most energy-efficient and mechanically compliant response, allowing greater deformation while resisting structural failure. The combination of surface-level bonding and through-thickness crack redirection highlights the synergistic nature of multi-scale patterning, which improves both interfacial and structural failure resistance.

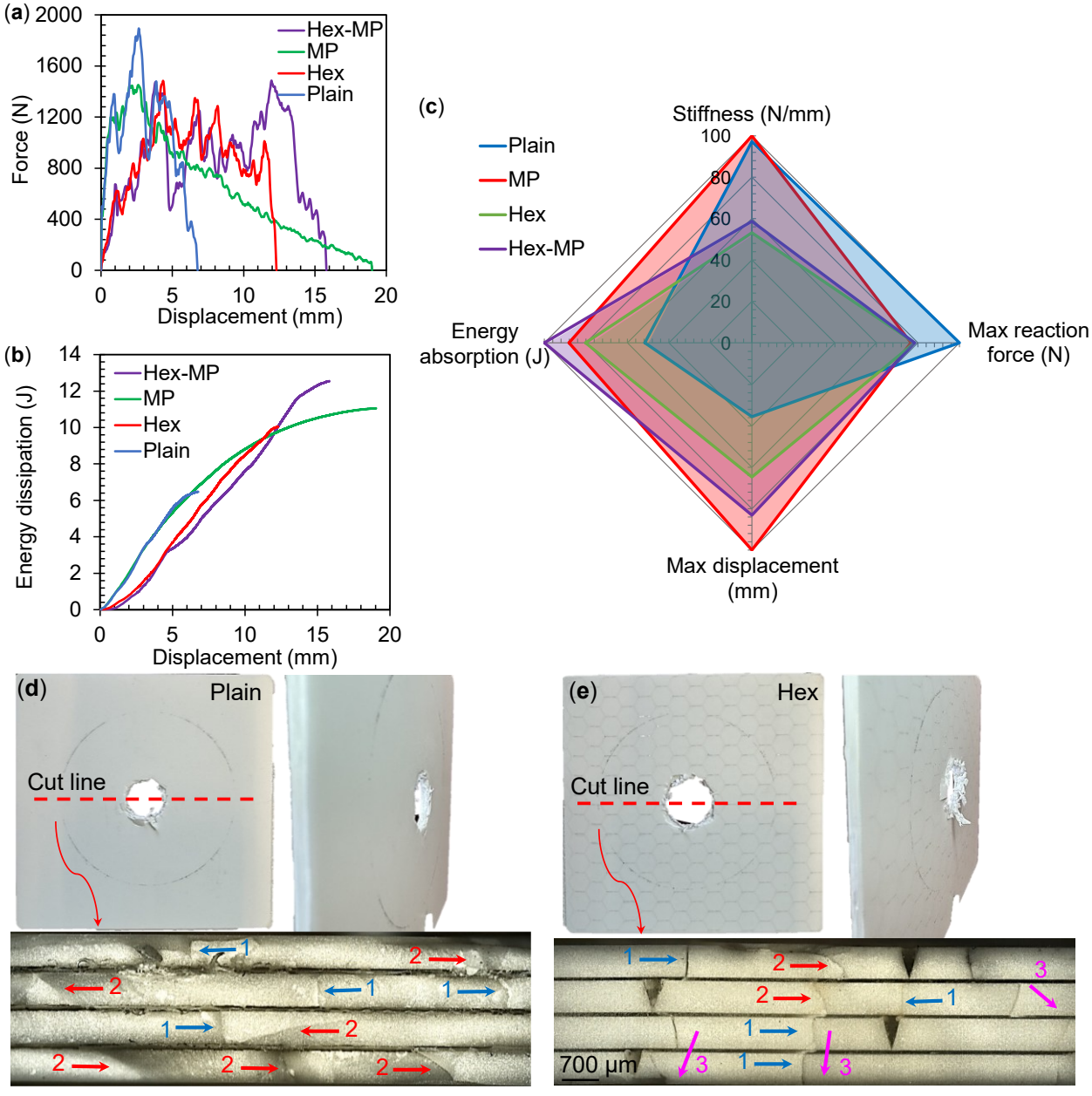

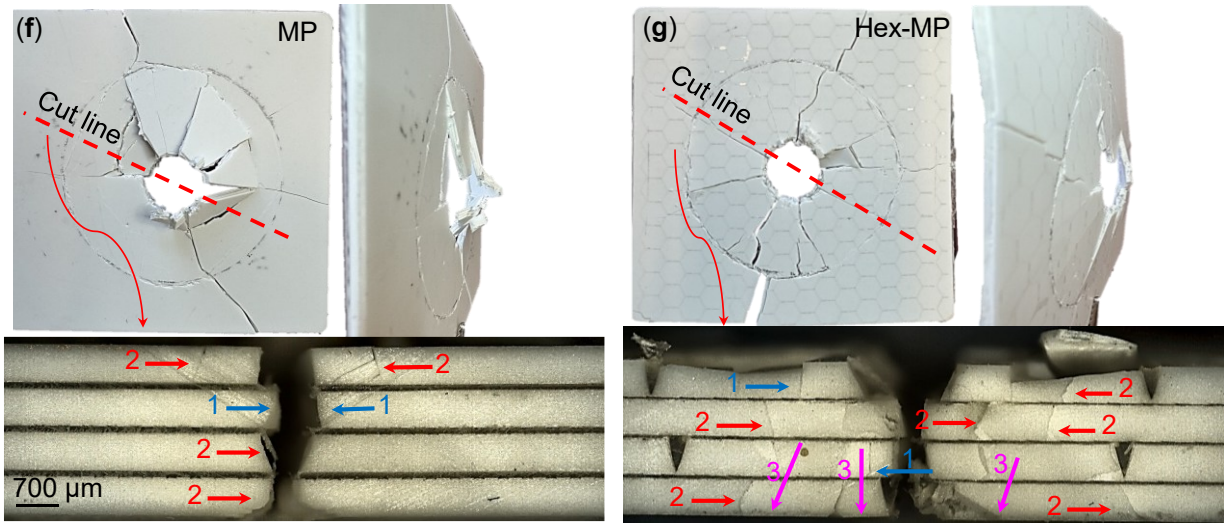

Figure 6.4. Influence of surface patterning on the mechanical behavior of bioinspired ceramic designs: (a) Force–displacement curves under 20 J low-velocity impact for all sample types; (b) Absorbed energy as a function of displacement; (c) Comparative performance summary of Plain, Hex, MP, and MP-Hex samples; (d–g) Post-impact surface morphology and microscopy images of (d) Plain, (e) Hex, (f) MP, and (g) MP-Hex samples, illustrating fracture patterns and failure mechanisms. Numbered arrows in the images indicate representative crack types: (1) Vertical microcracks from bending-induced tensile stress; (2) Diagonal microcracks from in-plane shear; (3) Interlayer crack bridging across ceramic layers. Results are based on six repeated tests per configuration; standard deviation was less than 5%.

6.4.3 Pattern Influence on Damage Propagation

All samples experienced perforation under the initial 20 J low-velocity impact, which, while useful for evaluating peak performance, limited the ability to observe progressive damage mechanisms. To overcome this and allow for a more detailed assessment of damage evolution, the impact energy was reduced to 2 J, enabling repeated low-energy impacts without immediate failure. As shown in Figure 6.5, all sample types exhibited visible damage following the first 2 J impact. However, the extent of rebound displacement observed in the force-displacement curves (see Figure 6.5a) and summarized in Figure 6.5c provides further insight into their relative structural resilience. Rebound percentage is defined as the ratio of the final displacement after unloading to the peak displacement during impact:

$$\text{Rebound Percentage} = \left(\frac{\Delta_{max}-\Delta_{final}}{\Delta_{max}}\right)\times 100\% \qquad \text{Equation 6.1}$$

Here, Δ_{max} represents the maximum displacement of the impactor during loading, while Δ_{final} is the residual displacement after unloading, measured at the end of the rebound phase. Although not a standardized metric in ASTM protocols, this parameter is introduced here as a comparative tool to evaluate elastic recovery and interfacial compliance in multilayered ceramic systems. Higher rebound percentages suggest that the Surlyn® interlayer governs the response, allowing the structure to absorb and release impact energy elastically. Conversely, lower rebound values reflect brittle, ceramic-dominated behavior, where energy is dissipated primarily through irreversible damage such as fracture and delamination. Similar rebound-based metrics have been adopted in composite materials research to assess damage tolerance and energy return under repeated impacts [154]. The Plain sample demonstrated minimal rebound, suggesting that it suffered more severe internal damage and lost its ability to restore energy elastically. In contrast, samples with patterned designs — especially those with micro-patterns — exhibited higher rebound values, indicating partial retention of structural integrity and more distributed load transfer.

The force-displacement response from the first impact (see Figure 6.5a) further supports these observations. The Plain sample recorded the highest peak force (~1400 N), reflecting its high initial stiffness, but its low rebound and large damage area are indicative of brittle failure and limited damage tolerance. Patterned samples, particularly those incorporating micro-patterns, displayed more favorable energy dissipation profiles, with full rebound and more gradual force decay, signaling controlled deformation and higher ductility. During the second 2 J impact (Figure 6.5b), damage progression became more pronounced. The Plain sample's maximum reaction force dropped by ~40%, and its stiffness was reduced by nearly half, confirming that it had sustained critical internal degradation. The Hex sample also experienced a marked drop in performance, failing catastrophically after the second impact despite its improved performance during the first. These trends are clearly reflected in Figure 6.5c, which shows significant reductions in both stiffness and peak force for the Plain and Hex configurations between the first and second impacts. In contrast, the MP and MP-Hex samples maintained consistent mechanical performance across both impacts. Their stiffness and maximum reaction force values remained relatively stable, with less than 15% reduction overall. These results demonstrate the benefits of the hierarchical design: micro-patterning strengthens the ceramic–polymer interface, while hexagonal cuts enhance energy dissipation through tile movement and crack bridging. Among all configurations, the MP-Hex design exhibited the highest rebound, minimal stiffness loss, and the most stable force response —

confirming its superior resistance to cumulative damage and validating the synergistic effect of combining micro- and macro-architectures in bioinspired ceramics.

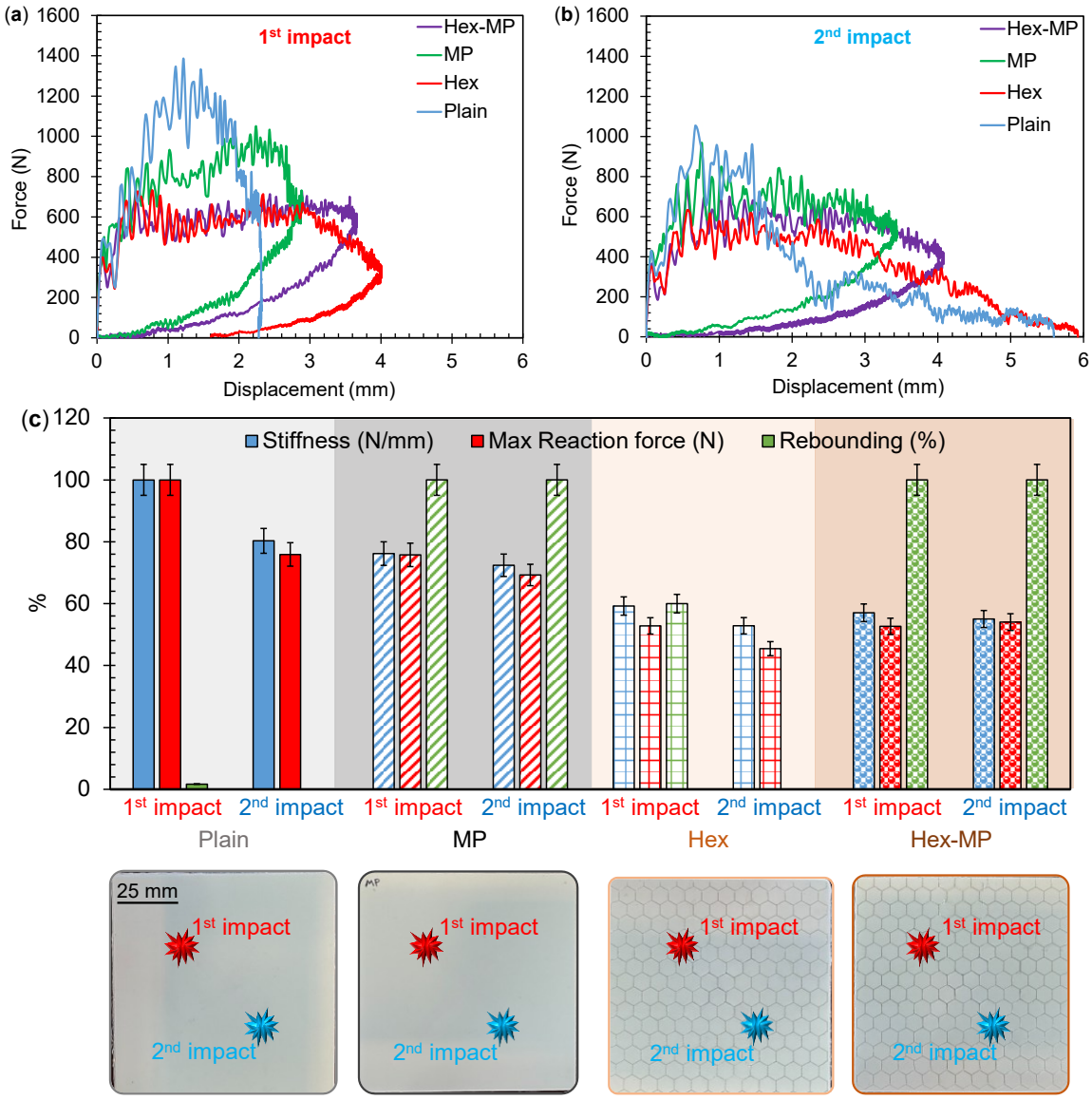

Figure 6.5. Impact response of bioinspired ceramics under repeated low-velocity impacts: (**a**) Force-displacement curves for the first 2 J impact; (**b**) Force-displacement curves for the second 2 J impact; (**c**) Comparative performance summary for all sample configurations under the first and second impacts. Stiffness and maximum reaction force values are normalized to the highest value observed across all samples, while rebound percentage is shown as a unitless ratio (final displacement divided by maximum displacement). All samples absorbed the entire 2 J of input energy during the second impact. As a result, no meaningful differences in energy absorption were observed, and energy plots were not included for this impact stage. Results are based on six repeated tests per configuration; standard deviation was less than 5%.

To further investigate internal damage and delamination, X-ray radiography with zinc iodide penetration was employed. This method enhances damage visibility by allowing the radiopaque

zinc iodide solution to infiltrate debonded regions and cracks, which appear as lighter areas in the radiographic images. Figure 6.6 provides a comparative view of internal damage evolution across different ceramic systems, using both standard X-ray and zinc-enhanced radiography. The initial radiographs captured after the first impact (Figure 6.6b) show partial internal damage, although cracks are difficult to discern in the Plain sample due to limited image contrast. This limitation was overcome through zinc iodide penetration (Figure 6.6c), which significantly improved the visualization of fracture networks and delaminated interfaces. Macro-crack propagation was observed in all samples, radiating from the impact site toward the tile edges. In the Plain and Hex samples, these cracks were accompanied by extensive delamination, as evidenced by widespread zinc infiltration near the crack kerfs. The larger affected area in the Plain sample suggests lower interfacial toughness and a greater tendency for separation of layers under impact loading. In contrast, the MP and MP-Hex samples exhibited substantially smaller regions of zinc iodide penetration, with damage largely confined to a narrow zone around the impact site. This confirms that micro-patterning strengthens interfacial bonding, thereby limiting crack propagation and reducing internal damage. The enhanced adhesion likely promotes more uniform stress distribution and minimizes the concentration of shear stresses at the ceramic–polymer interface. Among all designs, the MP-Hex sample demonstrated the smallest delamination area, confirming the synergy between macro-scale crack deflection and micro-scale bonding enhancement. The internal damage in this sample remained highly localized, and no through-thickness cracks were detected, even after repeated impacts.

Figure 6.6d further illustrates the evolution of damage following the second impact. The Plain and Hex samples exhibited a marked increase in delamination and layer separation, consistent with brittle and uncontrolled failure. In contrast, the MP and MP-Hex configurations showed more gradual and contained damage growth, indicative of a progressive failure mode commonly associated with toughened systems. The zinc-enhanced radiographs (see Figure 6.6d) visually confirm this trend — bright regions representing delamination were significantly more confined in patterned samples. It should be noted that not all white areas in the zinc-enhanced images represent delamination; some may result from excess surface zinc that was not fully removed. However, the consistent reduction in affected areas across the MP and MP-Hex samples provides strong qualitative evidence of superior interfacial strength, damage resistance, and multi-hit durability in the bioinspired designs.

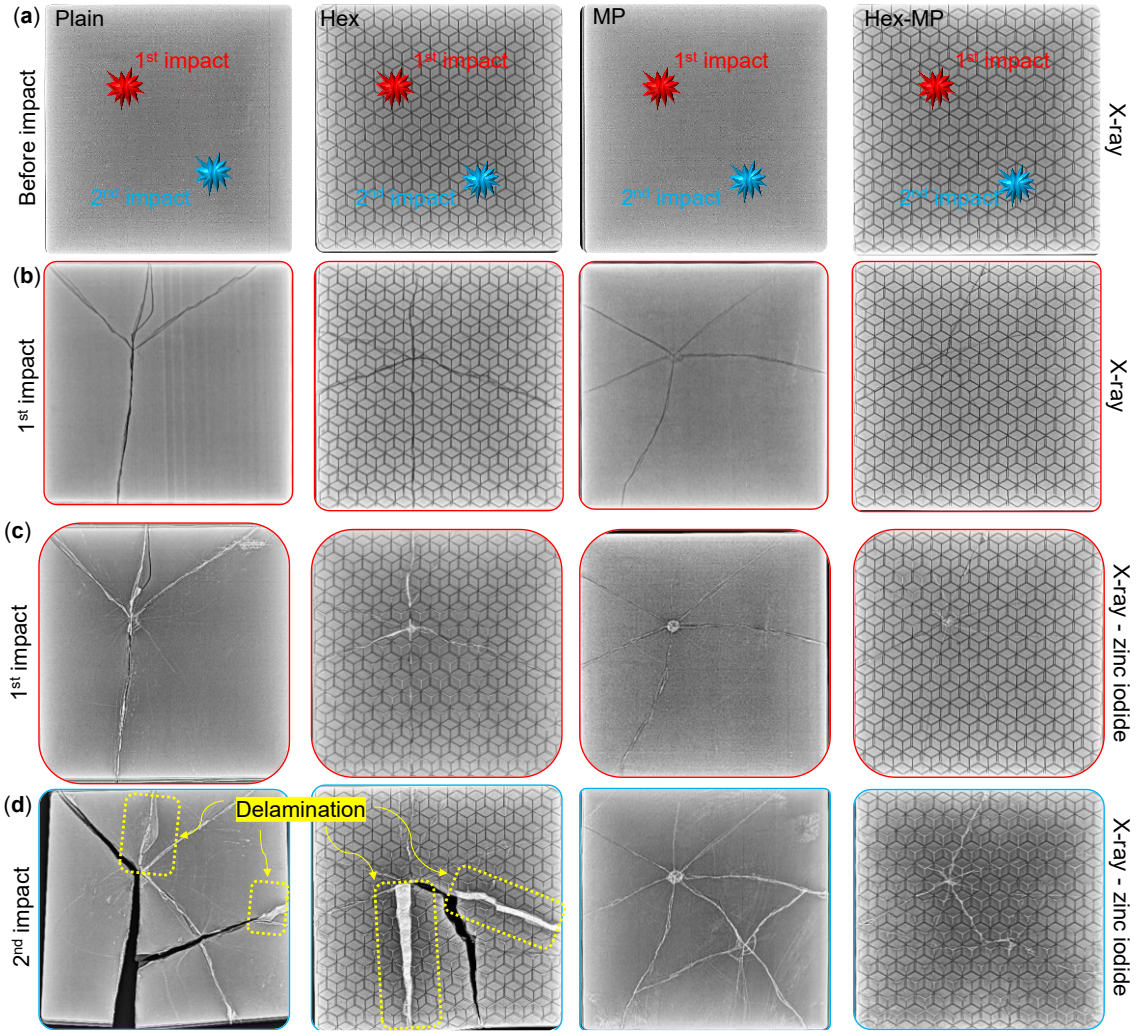

Figure 6.6. (**a**) Schematic showing the locations of the first and second impacts on each sample; (**b**) Damage visualization following the first impact using X-ray radiography; (**c**) Damage visualization following the first impact using X-ray radiography with zinc iodide penetration; (**d**) Damage progression and delamination after the second impact using X-ray radiography with zinc iodide penetration, highlighting the extent of internal damage across different ceramic systems.

6.4.4 Crack Evolution and Energy Dissipation

To support the experimental findings and provide a theoretical understanding of the observed mechanical behavior, an analytical framework was developed to investigate the influence of multi-scale patterning on stress distribution, crack propagation, and energy dissipation in the bioinspired multilayered ceramics. The patterned ceramics consist of alternating layers of stiff alumina tiles and soft Surlyn® interlayers. The total energy absorbed U_{total} under impact can be decomposed into elastic deformation, tile cracking, and interfacial delamination [158]:

$$U_{total} = U_{elastic} + U_{crack} + U_{delam} \qquad \text{Equation 6.2}$$

where $U_{elastic} = ½\ k\Delta_f^2$ represents the elastic energy stored up to failure, with k as the effective stiffness and Δ_f as the failure displacement, defined as the strain at failure multiplied by the laminate thickness, $U_{crack} = A_{crack}G_c$ accounts for the energy consumed by tile cracking, with A_{crack} representing the total crack surface area and G_c the fracture energy (J/m^2), and $U_{delam} = A_{int}G_{int}$ represents the interfacial energy dissipation, dependent on delaminated area A_{int} and interfacial fracture energy G_{int}.

Micro-patterning enhances interfacial bonding by increasing the contact area and introducing mechanical interlocks, which can raise the effective interfacial fracture toughness G_{int} by resisting crack initiation and growth. Simultaneously, it promotes more uniform stress transfer across layers and shifts failure modes from interfacial delamination to distributed macrocrack propagation within the ceramic tiles, as supported by rebound behavior and damage morphology.

Hexagonal macro-patterning introduces predefined paths that redirect crack propagation along tile boundaries. This increases the effective crack path length and contributes to energy dissipation through tile rotation, frictional sliding, and crack deflection. The effective crack length can be approximated as [158,159]:

$$a_{eff}^{hex} \approx a(1 + \alpha \frac{P}{L_{hex}}) \qquad \text{Equation 6.3}$$

where P is the tile perimeter, L_{hex} is the hexagon side length, and α is a geometric factor reflecting crack tortuosity. When combined in the MP-Hex configuration, these mechanisms act synergistically. Micro-patterns enhance interfacial toughness by improving bonding and anchoring at the ceramic–polymer interface, effectively shifting failure away from delamination. Microscopy (see Figure 2a inset) and post-impact analysis confirmed that Surlyn® successfully infiltrates the micro-patterns, enabling mechanical interlocking. This interlocking resists crack initiation, promotes stress redistribution, and contributes to the suppression of interfacial debonding, as evidenced by smaller delaminated areas in X-ray images. Hexagonal macro-cuts, while not improving interfacial adhesion directly, increase crack path complexity and promote energy dissipation through tile segmentation, crack deflection, and frictional sliding. These predefined weak planes enable cracks to redirect and arrest along tile boundaries, increasing energy dissipation per unit length of fracture. Together, the micro-patterns control failure at the interface, while the macro-patterns control failure within the structure. This dual mechanism leads to higher energy absorption and stiffness retention under repeated impacts, as confirmed by the rebound percentages

and load-displacement data. The MP-Hex configuration exhibited the most distributed failure mode, enabling more extensive macrocrack formation while maintaining laminate integrity, which explains its superior performance.

Table 6.2**.** Summary of dominant energy dissipation mechanisms for each configuration, presented relative to the Plain design. Ratings reflect qualitative trends in interfacial toughness, crack path length, stress uniformity, and energy absorption based on experimental results.

Configuration	Interfacial Toughness	Crack Path Length	Stress Uniformity	Energy Absorption
Plain	Low	Straight	Poor	Low
MP	Moderate–High	Slightly Increased	Improved	Moderate–High
Hex	High	Greatly Increased	Poor (like Plain)	High
MP-Hex	Very High	Most Increased	Highest	Highest

A summary of the dominant energy dissipation mechanisms for each design is provided in Table 2. All qualitative ratings are expressed relative to the Plain configuration, which serves as the reference baseline. Table 2 highlights the influence of each patterning strategy — micro-patterning, hexagonal macro-patterning, and their combination — on key performance attributes including interfacial toughness, crack path complexity, stress distribution, and energy absorption. This analytical interpretation complements the experimental observations and reinforces how multi-scale surface patterning improves the mechanical performance and damage tolerance of ceramic laminates by addressing both interfacial and structural failure mechanisms.

6.5 Conclusion

This study investigated the impact behavior and damage evolution of architectured ceramics enhanced with hexagonal macro-patterns (Hex) and diagonal micro-patterns (MP), inspired by natural armors such as nacre. High-precision picosecond laser micromachining was used to engrave full-depth hexagonal cuts and shallow surface patterns onto alumina tiles. A combined configuration, MP-Hex, integrated both pattern types into a multi-scale design. The results demonstrate that hierarchical surface patterning significantly improves mechanical performance, energy absorption, and damage tolerance under low-velocity impacts. The MP configuration directly enhanced interfacial adhesion between ceramic and polymer layers, promoting uniform

stress distribution and macrocrack-driven energy absorption. In contrast, Hex contributed indirectly by enabling crack path redirection, segmentation, and bridging, which collectively increased energy dissipation. Their integration in the MP-Hex configuration produced a synergistic effect, combining efficient stress redistribution with improved interfacial retention. The MP-Hex samples absorbed nearly twice as much energy as the unpatterned control (up to 12.5 J) and exhibited the highest deformation before perforation. They also maintained superior performance under repeated impacts, with minimal loss in stiffness and maximum reaction force. Rebound analysis indicated that higher rebound ratios in patterned samples were due to the Surlyn® interface absorbing and releasing energy elastically, whereas lower rebound in Plain and Hex-only designs signaled brittle, ceramic-dominated failure. X-ray radiography with zinc iodide penetration further validated the mechanical findings. Plain and Hex-only samples exhibited widespread delamination, while MP and MP-Hex samples showed localized damage and significantly smaller delaminated areas, confirming enhanced interfacial toughness and resistance to progressive failure. These findings validate multi-scale surface patterning — particularly the integration of micro- and macro-architectures — as an effective strategy for enhancing toughness, energy absorption, and durability in ceramic systems. The MP-Hex design emerged as the most robust, offering a balanced combination of stiffness retention, energy dissipation, and multi-hit resilience. This functionally bioinspired approach reflects key design principles found in natural materials such as nacre and abalone, and holds strong potential for protective systems in extreme environments. The conclusions drawn are supported by statistically repeatable experiments, with variations less than 5% across six repeated tests for each configuration. In addition to impact testing, complementary evaluations such as three-point bending and interfacial shear tests have been reported in our prior works [86,124], further validating the role of surface patterning in enhancing toughness and structural integrity across different failure modes. From a practical standpoint, laser micromachining offers a scalable and digitally programmable method compatible with various ceramic geometries. While the initial equipment investment may be high, the technique minimizes material waste and post-processing time. Its modularity also enables tuning of mechanical properties for specific applications, supporting the broader manufacturability and cost-effectiveness of patterned ceramics in aerospace, defense, and high-performance protective systems.

Chapter 7:

Conclusion and Future Work

7.1 Conclusions

This thesis offers an in-depth exploration of the design, fabrication, and mechanical performance of bioinspired ceramic composites, with a particular focus on how interfacial architecture governs their toughening behavior. Motivated by structural strategies found in nature—particularly in materials like nacre, conch shell, and the mantis shrimp's dactyl club—this work bridges biological inspiration with advanced materials engineering. Through a combination of experimental analysis, high-precision laser processing, and numerical modeling, the research introduces scalable, design-driven solutions to overcome the inherent brittleness of ceramics.

Chapter 1 outlined the research motivation, emphasizing the limitations of weak interfacial bonding in bioinspired ceramic–polymer composites. It highlighted how poor adhesion at the ceramic–polymer interface hinders effective load transfer and limits energy absorption, ultimately reducing the toughness and performance of the system.

Chapter 2 provided a comprehensive background on natural structural armors and reviewed relevant literature on bioinspired ceramic composites. It explored how biological architectures inform material design and examined current strategies for enhancing mechanical performance through microstructural engineering.

Chapter 3 investigates the effect of mortar volume fraction on the interfacial mechanics of bioinspired ceramic composites using cohesive zone modeling validated by single lap joint (SLJ) tests. Results show that higher mortar content enhances plastic deformation and energy dissipation, while lower volumes improve stiffness but trigger earlier crack initiation. Compared to MMV, LMV increased stiffness by 5% and reduced SERR by 26%, while HMV reduced stiffness by 4% and raised SERR by 29%. These findings underscore the importance of optimizing mortar volume to balance stiffness and toughness in nacre-inspired ceramic systems.

Chapter 4 introduces a dual-scale architectural approach, combining ±45° micro-patterning with hexagonal macro-tiles to significantly enhance mechanical resilience. Laser micromachining enabled precise integration of these features into alumina–Surlyn® composites. The synergistic interaction between micro- and macro-patterns led to improved interfacial adhesion, enhanced load

transfer, and up to 107% increase in energy dissipation—closely mimicking the layered, energy-absorbing mechanisms of natural armors.

Chapter 5 builds upon previous findings by evaluating the static and cyclic flexural performance of bioinspired ceramic composites with various stacking configurations. Architectural designs ranging from brittle, high-stiffness to ductile, energy-absorbing systems were systematically assessed. The Ceramic FF configuration demonstrated the most nacre-like behavior, offering superior ductility and fatigue resistance. Macro-architectures and stacking sequences enhanced energy absorption by up to 85% through mechanisms such as crack deflection and plastic deformation of the soft phase, while micro-patterns increased flexural strength by up to 140% by improving interfacial interactions.

Chapter 6 investigates the impact resistance of the bioinspired composites, emphasizing the effectiveness of the combined micro-patterned and hexagonal (MP-Hex) architecture. This multiscale design nearly doubled energy absorption under low-velocity impacts (up to 12.5 J) compared to unpatterned ceramics, significantly delaying crack propagation, reducing delamination, and preserving structural stiffness under repeated loading. The MP-Hex configuration exhibited the highest deformation before perforation, outperforming all other patterns and demonstrating the potential of multiscale surface architectures to produce robust, damage-tolerant ceramic systems.

Overall, this work demonstrates how principles observed in nature can be translated into practical engineering solutions using modern manufacturing technologies. The integration of programmable laser machining with biologically informed design enables the development of ceramic composites with tailored mechanical responses—balancing strength, ductility, and durability. These findings pave the way for next-generation structural materials ideally suited for aerospace, defense, and advanced protective applications, where reliability and performance under extreme conditions are paramount.

7.2 Future works

Several future research directions have been planned or identified as promising areas for further investigation. These directions are categorized into three main groups, as outlined below:

7.2.1 Bioinspiration

The most significant contribution of this study lies in the use of micro-patterning, a common strategy observed in natural armors, to enhance interfacial bonding between structural components. As scientific exploration of nature and biological systems continues, new insights are regularly uncovered, while many mechanisms remain unknown. For instance, the discovery of an impact-resistant coating composed of densely packed nanoparticles was not reported until 2020 [20]. Similarly, the interlocking suture-like patterns found in the crania of white-tailed deer and the exoskeletons of the diabolical ironclad beetle were only identified and brought to the attention of the engineering community after 2023 [160]. These examples highlight how nature holds a wealth of design strategies that can inform and inspire research, development, and engineering innovation (Figure 7.1).

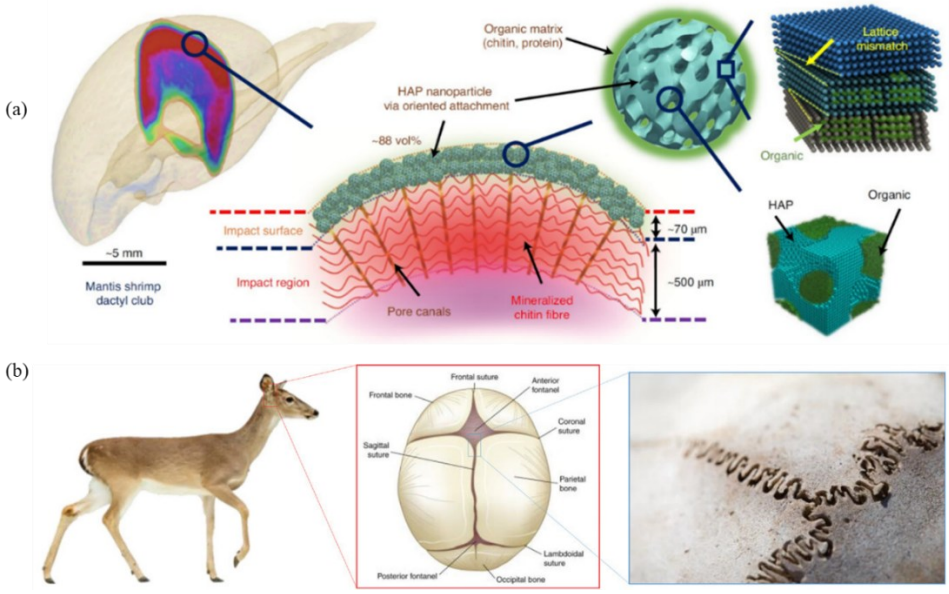

Figure 7.1. (a) White-tailed deer (Odocoileus virginianus) skull exhibiting cranial sutures, (b) Schematic representation of the mantis shrimp's (Odontodactylus scyllarus) dactyl club, highlighting the impact surface and illustrating its hierarchical architecture. The outermost layer comprises a densely packed coating of ~65

nm hydroxyapatite nanoparticles integrated within an organic matrix, contributing to its exceptional impact resistance [20,160].

7.2.2 Material and Method

The primary materials used in this study were limited to Surlyn and alumina, serving as the soft and hard components, respectively. However, a wide range of alternative materials can be explored to tailor the properties of bioinspired ceramic composites for specific applications. For instance, replacing Surlyn with pressure-sensitive adhesive (PSA) foam layers enables the development of flexible, multilayered bioinspired ceramics suitable for personal protective equipment (PPE) (Figure 7.2a).

The programmable and digital manufacturing process developed in this study was primarily based on laser machining, a subtractive technique that comes with inherent limitations. One of the most significant constraints is its 2.5D control over ceramic micromachining, which restricts the fabrication of complex geometries. To overcome this, advanced manufacturing methods such as 3D printing and other additive manufacturing techniques can be employed to enable the production of more intricate designs (Figure 7.2b).

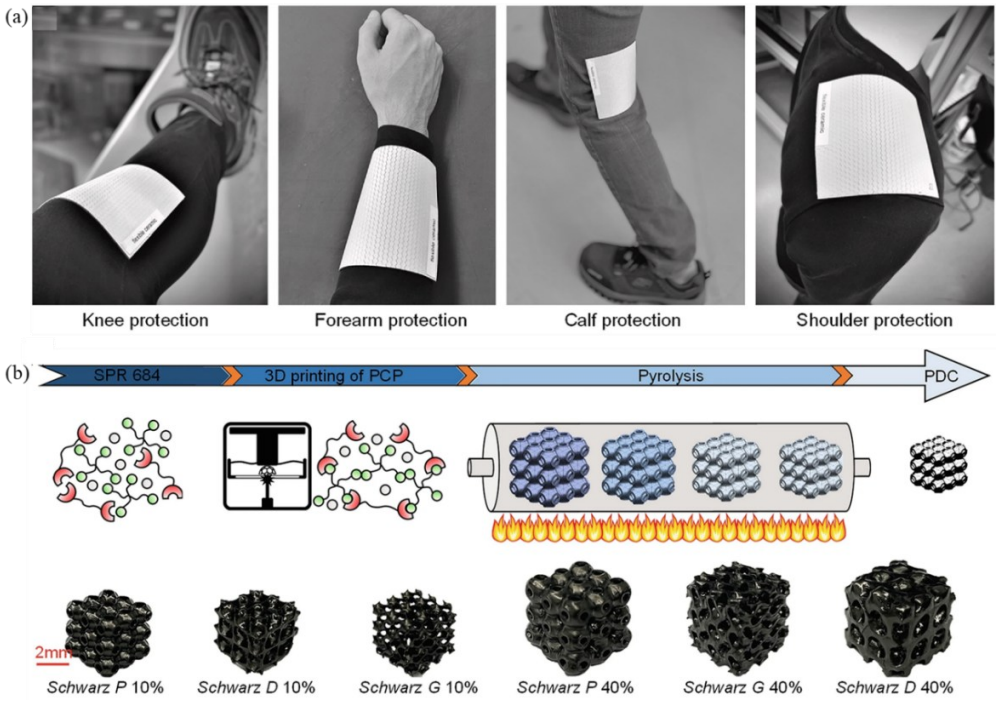

Figure 7.2. PPE equipment applications of soft 3-layer ceramic, including knee protection, forearm protection, calf protection, and shoulder protection. Its combination of flexibility and impact resistance makes it suitable for ergonomic designs that safeguard critical areas while maintaining mobility and comfort, and (b) Process of creating PDCs from a PCP (with or without filler particles), 3D printing, pyrolysis, and testing [138,161].

7.2.3 Design and Engineering

The investigations presented in this study were primarily conducted through experimental approaches. However, to further validate the findings regarding the role of mortar volume fraction in the interfacial properties of brick-and-mortar structures, a three-dimensional finite element analysis (FEA) was performed using ABAQUS with a cohesive zone model (CZM). Looking forward, we propose that multiscale simulations could provide valuable insights into how micro-patterns influence interfacial properties and, consequently, affect the overall structural behavior of bioinspired ceramic composites. In the initial phase of this proposed direction, we developed a 3D model leveraging our prior experience with cohesive zone elements. The adherents were meshed using reduced integration eight-node linear brick elements (C3D8R), while the adhesive layer was modeled with a single layer of eight-node three-dimensional cohesive elements (COH3D8), ensuring compatibility with the C3D8R elements.

Building upon established interface failure criteria, this model employed the Quadratic Nominal Stress Criterion (QUADS) to simulate damage initiation and utilized the damage variable parameter (D) to represent damage propagation within the interface, consistent with the methodology described in Section 3.3.3. The correlation between experimental results and FEA outcomes, as presented in the Figure 7.3, indicates that the implemented cohesive elements are suitable candidates for higher-scale modeling, such as simulating laminated ceramics under impact conditions. Multiscale modeling holds the potential to predict the behavior of bioinspired ceramic composites across various designs, including micro-patterns, macro-patterns, and cell geometries, thereby informing the development of advanced materials with tailored properties.

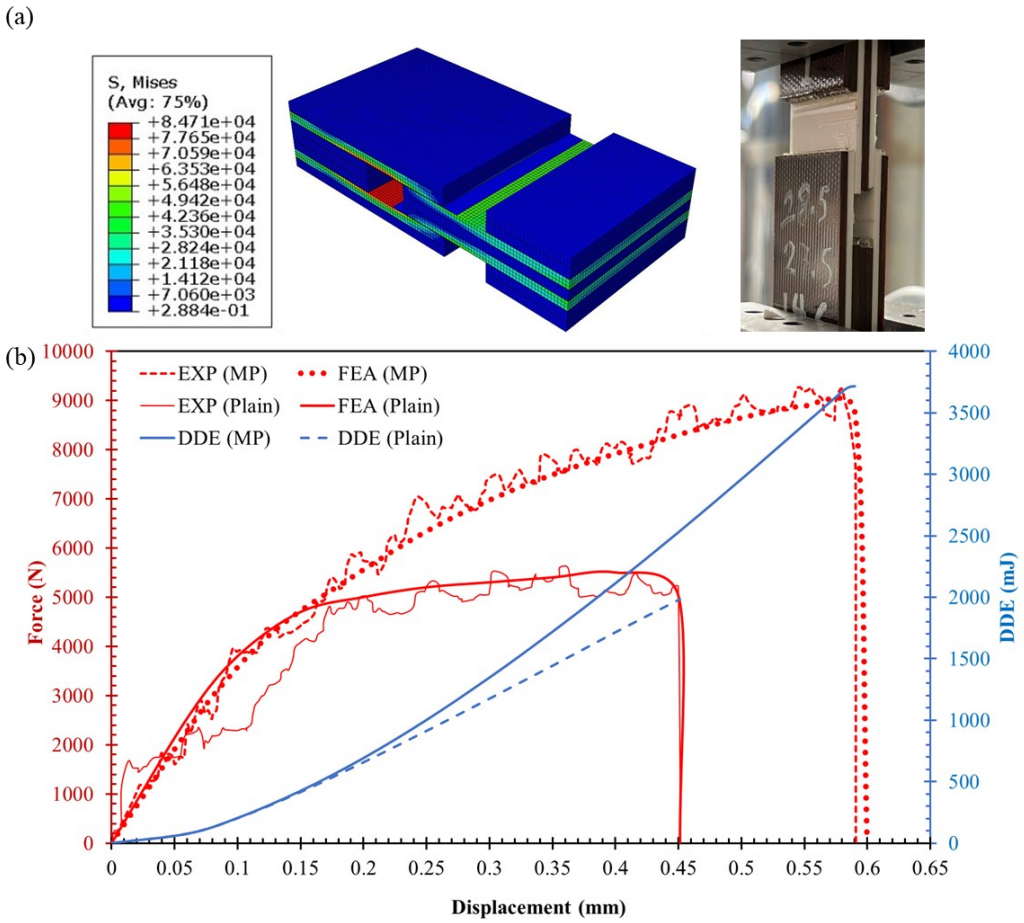

Figure 7.3. (a) 3D Model and boundary conditions used for doube lap joint (DLJ) test, (b) Comparison of experimental and FEA force-displacement results for the plain and micro-patterned samples and DDE graph for the specimens, showing distinct energy dissipation behaviors.

References

[1] Kamat S, Kessler H, Ballarini R, Nassirou M, Heuer ArthurH. Fracture mechanisms of the Strombus gigas conch shell: II-micromechanics analyses of multiple cracking and large-scale crack bridging. Acta Mater 2004;52:2395–406. https://doi.org/10.1016/j.actamat.2004.01.030.

[2] Evans AG. Perspective on the Development of High-Toughness Ceramics. Journal of the American Ceramic Society 1990;73:187–206. https://doi.org/10.1111/j.1151-2916.1990.tb06493.x.

[3] Ayode Otitoju T, Ugochukwu Okoye P, Chen G, Li Y, Onyeka Okoye M, Li S. Advanced ceramic components: Materials, fabrication, and applications. Journal of Industrial and Engineering Chemistry 2020;85:34–65. https://doi.org/10.1016/j.jiec.2020.02.002.

[4] Liu Y, Jiang X, Shi J, Luo Y, Tang Y, Wu Q, et al. Research on the interface properties and strengthening–toughening mechanism of nanocarbon-toughened ceramic matrix composites. Nanotechnol Rev 2020;9:190–208. https://doi.org/10.1515/ntrev-2020-0017.

[5] Sun J, Zhao J, Chen Y, Wang L, Yun X, Huang Z. Macro-micro-nano multistage toughening in nano-laminated graphene ceramic composites. Materials Today Physics 2022;22:100595. https://doi.org/10.1016/j.mtphys.2021.100595.

[6] Bouville F, Maire E, Meille S, Van de Moortèle B, Stevenson AJ, Deville S. Strong, tough and stiff bioinspired ceramics from brittle constituents. Nat Mater 2014;13:508–14. https://doi.org/10.1038/nmat3915.

[7] Yazdani Sarvestani H, Aranguren van Egmond D, Esmail I, Genest M, Paquet C, Ashrafi B. Bioinspired Stochastic Design: Tough and Stiff Ceramic Systems. Adv Funct Mater 2022;32:2108492. https://doi.org/10.1002/adfm.202108492.

[8] Sun H, Gao K, Yi Z, Han C, Liu Z, Wang Q, et al. Cytotoxicity and Bonding Property of Bioinspired Nacre-like Ceramic-Polymer Composites. Front Bioeng Biotechnol 2022;10. https://doi.org/10.3389/fbioe.2022.913899.

[9] Barthelat F. Architectured materials in engineering and biology: fabrication, structure, mechanics and performance. International Materials Reviews 2015;60:413–30. https://doi.org/10.1179/1743280415Y.0000000008.

[10] Rahimizadeh A, Yazdani Sarvestani H, Li L, Barroeta Robles J, Backman D, Lessard L, et al. Engineering toughening mechanisms in architectured ceramic-based bioinspired materials. Mater Des 2021;198. https://doi.org/10.1016/j.matdes.2020.109375.

[11] Yazdani Sarvestani H, Mirkhalaf M, Akbarzadeh AH, Backman D, Genest M, Ashrafi B. Multilayered architectured ceramic panels with weak interfaces: energy absorption and multi-hit capabilities. Mater Des 2019;167. https://doi.org/10.1016/j.matdes.2019.107627.

[12] Yazdani Sarvestani H, Beausoleil C, Genest M, Ashrafi B. Architectured ceramics with tunable toughness and stiffness. Extreme Mech Lett 2020;39:100844. https://doi.org/10.1016/j.eml.2020.100844.

[13] BARTHELAT F, TANG H, ZAVATTIERI P, LI C, ESPINOSA H. On the mechanics of mother-of-pearl: A key feature in the material hierarchical structure. J Mech Phys Solids 2007;55:306–37. https://doi.org/10.1016/j.jmps.2006.07.007.

[14] Barthelat F, Yin Z, Buehler MJ. Structure and mechanics of interfaces in biological materials. Nat Rev Mater 2016;1:16007. https://doi.org/10.1038/natrevmats.2016.7.

[15] Yazdani Sarvestani H, Mirkhalaf M, Akbarzadeh AH, Backman D, Genest M, Ashrafi B. Multilayered architectured ceramic panels with weak interfaces: energy absorption and multi-hit capabilities. Mater Des 2019;167:107627. https://doi.org/10.1016/j.matdes.2019.107627.

[16] Callister W, Rethwisch D. Materials science and engineering: an introduction. 2018.

[17] Libonati F, Buehler MJ. Advanced Structural Materials by Bioinspiration . Adv Eng Mater 2017;19. https://doi.org/10.1002/adem.201600787.

[18] Gu GX, Takaffoli M, Buehler MJ. Hierarchically Enhanced Impact Resistance of Bioinspired Composites. Advanced Materials 2017;29. https://doi.org/10.1002/adma.201700060.

[19] Häsä R, Pinho ST. Failure mechanisms of biological crossed-lamellar microstructures applied to synthetic high-performance fibre-reinforced composites. J Mech Phys Solids 2019;125:53–73. https://doi.org/10.1016/j.jmps.2018.12.008.

[20] Huang W, Shishehbor M, Guarín-Zapata N, Kirchhofer ND, Li J, Cruz L, et al. A natural impact-resistant bicontinuous composite nanoparticle coating. Nat Mater 2020;19:1236–43. https://doi.org/10.1038/s41563-020-0768-7.

[21] Mathaudhu PS. Biomimetic Designs for Impact-Resistant Composite Materials Inspired by the Heavily Armored Mantis Shrimp A Dissertation submitted in partial satisfaction of the requirements for the degree of Doctor of Philosophy in Materials Sci 2018.

[22] Behera RP, Le Ferrand H. Impact-resistant materials inspired by the mantis shrimp's dactyl club. Matter 2021;4:2831–49. https://doi.org/10.1016/j.matt.2021.07.012.

[23] Suksangpanya N, Yaraghi NA, Pipes RB, Kisailus D, Zavattieri P. International Journal of Solids and Structures Crack twisting and toughening strategies in Bouligand architectures. Int J Solids Struct 2018;150:83–106. https://doi.org/10.1016/j.ijsolstr.2018.06.004.

[24] Yaraghi NA, Guarín-zapata N, Grunenfelder LK, Hintsala E, Bhowmick S, Hiller JM, et al. A Sinusoidally Architected Helicoidal Biocomposite 2016:1–10. https://doi.org/10.1002/adma.201600786.

[25] Islam MK, Hazell PJ, Escobedo JP, Wang H. Biomimetic armour design strategies for additive manufacturing: A review. Mater Des 2021;205:109730. https://doi.org/10.1016/j.matdes.2021.109730.

[26] Mencattelli L, Narducci F, Pinho S. Learning from nature : Bio-inspiration for damage-tolerant high-performance fibre-reinforced composites 2021;208.

[27] Steen WM. Laser Surface Treatment. Laser Material Processing, London: Springer London; 2003, p. 227–78. https://doi.org/10.1007/978-1-4471-3752-8_7.

[28] Poprawe R, editor. Tailored Light 2. Berlin, Heidelberg: Springer Berlin Heidelberg; 2011. https://doi.org/10.1007/978-3-642-01237-2.

[29] Dutta Majumdar J, Manna I. Laser processing of materials. Sadhana 2003 28:3 2003;28:495–562. https://doi.org/10.1007/BF02706446.

[30] Chryssolouris G. Laser machining: theory and practice. 2013.

[31] Ready JF. Industrial Applications of Lasers. , Academic Press: New York 1998.

[32] Beausoleil C, Yazdani Sarvestani H, Katz Z, Gholipour J, Ashrafi B. Deep and high precision cutting of alumina ceramics by picosecond laser. Ceram Int 2020;46:15285–96. https://doi.org/10.1016/j.ceramint.2020.03.069.

[33] Siddique SH, Hazell PJ, Wang H, Escobedo JP, Ameri AAH. Lessons from nature: 3D printed bio-inspired porous structures for impact energy absorption – A review. Addit Manuf 2022;58:103051. https://doi.org/10.1016/j.addma.2022.103051.

[34] Yin BB, Sun WK, Zhang XY, Liew KM. Deciphering structural biological materials: Viewing from the mechanics perspective and their prospects. Compos B Eng 2022;245:110213. https://doi.org/10.1016/j.compositesb.2022.110213.

[35] Ghazlan A, Ngo TD, Tran P. Influence of interfacial geometry on the energy absorption capacity and load sharing mechanisms of nacreous composite shells. Compos Struct 2015;132:299–309. https://doi.org/10.1016/j.compstruct.2015.05.045.

[36] Plocher J, Mencattelli L, Narducci F, Pinho S. Learning from nature: Bio-inspiration for damage-tolerant high-performance fibre-reinforced composites. Compos Sci Technol 2021;208:108669. https://doi.org/10.1016/j.compscitech.2021.108669.

[37] C. Barry Carter MGN. Ceramic materials: science and engineering. Vol 716. New York: Springer; 2007.

[38] Meyers MA, Chen P-Y, Lin AY-M, Seki Y. Biological materials: Structure and mechanical properties. Prog Mater Sci 2008;53:1–206. https://doi.org/10.1016/j.pmatsci.2007.05.002.

[39] Cui Z, Zhang M, Wang Y, Chen Y, Hu R, Zhang C. Failure progression and toughening mechanism of 3D-printed nacre-like structures under in-plane compression. J Mech Behav Biomed Mater 2023;138:105653. https://doi.org/10.1016/j.jmbbm.2023.105653.

[40] Ha NS, Lu G. A review of recent research on bio-inspired structures and materials for energy absorption applications. Compos B Eng 2020;181:107496. https://doi.org/10.1016/j.compositesb.2019.107496.

[41] Huang W, Restrepo D, Jung J, Su FY, Liu Z, Ritchie RO, et al. Multiscale Toughening Mechanisms in Biological Materials and Bioinspired Designs. Advanced Materials 2019;31:1901561. https://doi.org/10.1002/adma.201901561.

[42] Wang B, Yang W, Sherman VR, Meyers MA. Pangolin armor: Overlapping, structure, and mechanical properties of the keratinous scales. Acta Biomater 2016;41:60–74. https://doi.org/10.1016/j.actbio.2016.05.028.

[43] Harris CM. Illustrated dictionary of historic architecture. Courier Corporation; 1983.

[44] Fratzl P, Kolednik O, Fischer FD, Dean MN. The mechanics of tessellations – bioinspired strategies for fracture resistance. Chem Soc Rev 2016;45:252–67. https://doi.org/10.1039/C5CS00598A.

[45] Sherman VR, Quan H, Yang W, Ritchie RO, Meyers MA. A comparative study of piscine defense: The scales of Arapaima gigas, Latimeria chalumnae and Atractosteus spatula. J Mech Behav Biomed Mater 2017;73:1–16. https://doi.org/10.1016/j.jmbbm.2016.10.001.

[46] Duro-Royo J, Zolotovsky K, Mogas-Soldevila L, Varshney S, Oxman N, Boyce MC, et al. MetaMesh: A hierarchical computational model for design and fabrication of biomimetic

armored surfaces. Computer-Aided Design 2015;60:14–27. https://doi.org/10.1016/j.cad.2014.05.005.

[47] Rawat P, Zhu D, Rahman MZ, Barthelat F. Structural and mechanical properties of fish scales for the bio-inspired design of flexible body armors: A review. Acta Biomater 2021;121:41–67. https://doi.org/10.1016/j.actbio.2020.12.003.

[48] Bouaziz O, Bréchet Y, Embury JD. Heterogeneous and Architectured Materials: A Possible Strategy for Design of Structural Materials. Adv Eng Mater 2008;10:24–36. https://doi.org/10.1002/adem.200700289.

[49] Mirkhalaf M, Zhou T, Barthelat F. Simultaneous improvements of strength and toughness in topologically interlocked ceramics. Proceedings of the National Academy of Sciences 2018;115:9128–33. https://doi.org/10.1073/pnas.1807272115.

[50] Mirkhalaf M, Sunesara A, Ashrafi B, Barthelat F. Toughness by segmentation: Fabrication, testing and micromechanics of architectured ceramic panels for impact applications. Int J Solids Struct 2019;158:52–65. https://doi.org/10.1016/j.ijsolstr.2018.08.025.

[51] Magrini J. Ethical Responses to Nature's Call. Routledge; 2019. https://doi.org/10.4324/9780429429569.

[52] Zhu H, Cao H, Liu X, Wang M, Meng X, Zhou Q, et al. Nacre-like composite films with a conductive interconnected network consisting of graphene oxide, polyvinyl alcohol and single-walled carbon nanotubes. Mater Des 2019;175:107783. https://doi.org/10.1016/j.matdes.2019.107783.

[53] Ashby * MF. Hybrids to fill holes in material property space. Philosophical Magazine 2005;85:3235–57. https://doi.org/10.1080/14786430500079892.

[54] Li Y-Y, Liang S-M, Ji H-M, Li X-W. Distinctive Impact of Heat Treatment on the Mechanical Behavior of Nacreous and Crossed-Lamellar Structures in Biological Shells: Critical Role of Organic Matrix. ACS Biomater Sci Eng 2022;8:1143–55. https://doi.org/10.1021/acsbiomaterials.1c01538.

[55] Askarinejad S, Choshali HA, Flavin C, Rahbar N. Effects of tablet waviness on the mechanical response of architected multilayered materials: Modeling and experiment. Compos Struct 2018;195:118–25. https://doi.org/10.1016/j.compstruct.2018.04.047.

[56] Wan H, Leung N, Algharaibeh S, Sui T, Liu Q, Peng H-X, et al. Cost-effective fabrication of bio-inspired nacre-like composite materials with high strength and toughness. Compos B Eng 2020;202:108414. https://doi.org/10.1016/j.compositesb.2020.108414.

[57] Begley MR, Philips NR, Compton BG, Wilbrink D V., Ritchie RO, Utz M. Micromechanical models to guide the development of synthetic 'brick and mortar' composites. J Mech Phys Solids 2012;60:1545–60. https://doi.org/10.1016/j.jmps.2012.03.002.

[58] Bekah S, Rabiei R, Barthelat F. The micromechanics of biological and biomimetic staggered composites. J Bionic Eng 2012;9:446–56. https://doi.org/10.1016/S1672-6529(11)60145-5.

[59] Grossman M, Pivovarov D, Bouville F, Dransfeld C, Masania K, Studart AR. Hierarchical Toughening of Nacre-Like Composites. Adv Funct Mater 2019;29:1806800. https://doi.org/10.1002/adfm.201806800.

[60] Liang SM, Ji HM, Li XW. A high-strength and high-toughness nacreous structure in a deep-sea Nautilus shell: Critical role of platelet geometry and organic matrix. J Mater Sci Technol 2021;88:189–202. https://doi.org/10.1016/j.jmst.2021.01.082.

[61] Barthelat F. Designing nacre-like materials for simultaneous stiffness, strength and toughness: Optimum materials, composition, microstructure and size. J Mech Phys Solids 2014;73:22–37. https://doi.org/10.1016/j.jmps.2014.08.008.

[62] Lopez MI, Meza Martinez PE, Meyers MA. Organic interlamellar layers, mesolayers and mineral nanobridges: Contribution to strength in abalone (Haliotis rufescence) nacre. Acta Biomater 2014;10:2056–64. https://doi.org/10.1016/j.actbio.2013.12.016.

[63] Huang Z, Pan Z, Li H, Wei Q, Li X. Hidden energy dissipation mechanism in nacre. J Mater Res 2014;29:1573–8. https://doi.org/10.1557/jmr.2014.179.

[64] Askarinejad S, Rahbar N. Mechanics of bioinspired lamellar structured ceramic/polymer composites: Experiments and models. Int J Plast 2018;107:122–49. https://doi.org/10.1016/j.ijplas.2018.04.001.

[65] Maghsoudi-Ganjeh M, Lin L, Yang X, Zeng X. Computational modeling and simulation of bioinspired nacre-like composites. J Mater Res 2021;36:2651–61. https://doi.org/10.1557/s43578-021-00124-6.

[66] ASTM D3165-07. Standard test method for strength properties of adhesives in shear by tension loading of single-lap-joint laminated assemblies. Ann Book ASTM Stand 6 (2014): 15.; n.d.

[67] Ramalho LDC, Campilho RDSG, Belinha J, da Silva LFM. Static strength prediction of adhesive joints: A review. Int J Adhes Adhes 2020;96. https://doi.org/10.1016/j.ijadhadh.2019.102451.

[68] Álvarez D, Blackman BRK, Guild FJ, Kinloch AJ. Mode I fracture in adhesively-bonded joints: A mesh-size independent modelling approach using cohesive elements. Eng Fract Mech 2014;115:73–95. https://doi.org/10.1016/j.engfracmech.2013.10.005.

[69] Campilho RDSG, Banea MD, Pinto AMG, da Silva LFM, de Jesus AMP. Strength prediction of single- and double-lap joints by standard and extended finite element modelling. Int J Adhes Adhes 2011;31:363–72. https://doi.org/10.1016/j.ijadhadh.2010.09.008.

[70] ASTM D5528. Standard Test Method for Mode I Interlaminar Fracture Toughness of Unidirectional Fiber-Reinforced Polymer Matrix Composites. n.d.

[71] ASTM D7905. Standard Test Method for Determination of the Mode II Interlaminar Fracture Toughness of Unidirectional Fiber-Reinforced Polymer Matrix Composites. n.d.

[72] ASTM D4896. Standard Guide for Use of Adhesive-Bonded Single Lap-Joint Specimen Test Results. n.d.

[73] de Morais AB. Evaluation of a trilinear traction-separation law for mode II delamination using the effective crack method. Compos Part A Appl Sci Manuf 2019;121:74–83. https://doi.org/10.1016/j.compositesa.2019.03.010.

[74] Sadeghi MZ, Gabener A, Zimmermann J, Saravana K, Weiland J, Reisgen U, et al. Failure load prediction of adhesively bonded single lap joints by using various FEM techniques. Int J Adhes Adhes 2020;97. https://doi.org/10.1016/j.ijadhadh.2019.102493.

[75] Michael Smith. ABAQUS/Standard User's Manual, Version 6.9 2009.

[76] Liu X, Sun T, Wu Z, He H. Mode II interlaminar fracture toughness of unidirectional fiber-reinforced polymer matrix composites with synthetic boehmite nanosheets at room temperature and low temperature. J Compos Mater 2018;52:945–52. https://doi.org/10.1177/0021998317716529.

[77] Li X, Guo Z, Huang Q, Yuan C. Research and application of biomimetic modified ceramics and ceramic composites: A review. Journal of the American Ceramic Society 2024;107:663–97. https://doi.org/10.1111/jace.19490.

[78] Nazari K, Tran P, Tan P, Ghazlan A, Ngo TD, Xie YM. Advanced manufacturing methods for ceramic and bioinspired ceramic composites: A review. Open Ceramics 2023;15:100399. https://doi.org/10.1016/j.oceram.2023.100399.

[79] Tishkevich DI, Vorobjova AI, Shimanovich DL, Vinnik DA, Zubar TI, Kozlovskiy AL, et al. Formation and corrosion properties of Ni-based composite material in the anodic alumina porous matrix. J Alloys Compd 2019;804:139–46. https://doi.org/10.1016/j.jallcom.2019.07.001.

[80] Azad E, Sarvestani HY, Ashrafi B, Shadmehri F, Hojjati M. From Nature to Engineering: Impact of Mortar Volume on Interfacial Properties of Bioinspired Ceramics. n.d.

[81] Zhang Z, Gao H, Wen S, Pang J, Zhang S, Cui C, et al. Scalable Manufacturing of Mechanical Robust Bioinspired Ceramic–Resin Composites with Locally Tunable Heterogeneous Structures. Advanced Materials 2023;35. https://doi.org/10.1002/adma.202209510.

[82] Wang A, Wang S, Yin H, Bai R, Liu J, Zhang Z, et al. Structural effects in 'brick-and-mortar' architecture: Bio-inspired ceramic matrix composites developed through a new method. Ceram Int 2023;49:5042–8. https://doi.org/10.1016/j.ceramint.2022.10.017.

[83] Ghazlan A, Ngo T, Tan P, Xie YM, Tran P, Donough M. Inspiration from Nature's body armours – A review of biological and bioinspired composites. Compos B Eng 2021;205:108513. https://doi.org/10.1016/j.compositesb.2020.108513.

[84] Liang SM, Ji HM, Li XW. Thickness-dependent mechanical properties of nacre in Cristaria plicata shell: Critical role of interfaces. J Mater Sci Technol 2020;44:1–8. https://doi.org/10.1016/j.jmst.2019.10.039.

[85] Mirkhalaf M, Zreiqat H. Fabrication and Mechanics of Bioinspired Materials with Dense Architectures: Current Status and Future Perspectives. JOM 2020;72:1458–76. https://doi.org/10.1007/s11837-019-03986-8.

[86] Azad E, Yazdani Sarvestani H, Ashrafi B, Shadmehri F, Hojjati M. From macro to micro: Bioinspired designs for tougher ceramics. Journal of Materials Research and Technology 2024;31:3310–9. https://doi.org/10.1016/j.jmrt.2024.07.019.

[87] Amorim L, Santos A, Nunes JP, Viana JC. Bioinspired approaches for toughening of fibre reinforced polymer composites. Mater Des 2021;199:109336. https://doi.org/10.1016/j.matdes.2020.109336.

[88] Cui S, Lu Z, Yang Z. Effect of interlocking structure on mechanical properties of bio-inspired nacreous composites. Compos Struct 2019;226. https://doi.org/10.1016/j.compstruct.2019.111260.

[89] Wegst UGK, Bai H, Saiz E, Tomsia AP, Ritchie RO. Bioinspired structural materials. Nat Mater 2015;14:23–36. https://doi.org/10.1038/nmat4089.

[90] Huang W, Yaraghi NA, Yang W, Velazquez-Olivera A, Li Z, Ritchie RO, et al. A natural energy absorbent polymer composite: The equine hoof wall. Acta Biomater 2019;90:267–77. https://doi.org/10.1016/j.actbio.2019.04.003.

[91] Ha NS, Lu G, Xiang X. Energy absorption of a bio-inspired honeycomb sandwich panel. J Mater Sci 2019;54:6286–300. https://doi.org/10.1007/s10853-018-3163-x.

[92] Biomimetic Designs for Impact-Resistant Composite Materials Inspired by the Heavily Armored Mantis Shrimp n.d.

[93] Wang Y, Zheng G, Jiang N, Ying G, Li Y, Cai X, et al. Nature-inspired micropatterns. Nature Reviews Methods Primers 2023;3. https://doi.org/10.1038/s43586-023-00251-w.

[94] Grunenfelder LK, De Obaldia EE, Wang Q, Li D, Weden B, Salinas C, et al. Stress and damage mitigation from oriented nanostructures within the radular teeth of cryptochiton stelleri. Adv Funct Mater 2014;24:6093–104. https://doi.org/10.1002/adfm.201401091.

[95] Espinosa HD, Rim JE, Barthelat F, Buehler MJ. Merger of structure and material in nacre and bone – Perspectives on de novo biomimetic materials. Prog Mater Sci 2009;54:1059–100. https://doi.org/10.1016/j.pmatsci.2009.05.001.

[96] Rice C, Tan KT. Horse hoof inspired biomimetic structure for improved damage tolerance and crack diversion. Compos Struct 2019;220:362–70. https://doi.org/10.1016/j.compstruct.2019.04.009.

[97] Ha NS, Lu G. A review of recent research on bio-inspired structures and materials for energy absorption applications. Compos B Eng 2020;181:107496. https://doi.org/10.1016/j.compositesb.2019.107496.

[98] Sun F, Pruncu CI, Penchev P, Jiang J, Dimov S, Blackman BRK. Influence of surface micropatterns on the mode I fracture toughness of adhesively bonded joints. Int J Adhes Adhes 2020;103:102718. https://doi.org/10.1016/j.ijadhadh.2020.102718.

[99] Naat N, Boutar Y, Naïmi S, Mezlini S, da Silva LFM, Bashiri AH. Influence of bio-inspired surface texture of additively manufactured 17-4 PH stainless steel adherends on the strength of adhesively bonded joints. Int J Adhes Adhes 2023;126:103478. https://doi.org/10.1016/j.ijadhadh.2023.103478.

[100] Yin H, Liu J, Xia H, Guo L, Ao X, Luo J, et al. Effect of combination of microstructure and surface treatment on shear strength of precision bonded joints. J Adhes 2023:1–18. https://doi.org/10.1080/00218464.2023.2246389.

[101] Monteiro EC, Ávila AF. Improving single-lap joint load bearing by bioinspired interlocking patterns on substrates. Int J Adhes Adhes 2022;113:103043. https://doi.org/10.1016/j.ijadhadh.2021.103043.

[102] Porz L, Klomp AJ, Fang X, Li N, Yildirim C, Detlefs C, et al. Dislocation-toughened ceramics. Mater Horiz 2021;8:1528–37. https://doi.org/10.1039/D0MH02033H.

[103] Ritchie RO. The conflicts between strength and toughness. Nat Mater 2011;10:817–22. https://doi.org/10.1038/nmat3115.

[104] Mirkhalaf M, Dastjerdi AK, Barthelat F. Overcoming the brittleness of glass through bio-inspiration and micro-architecture. Nat Commun 2014;5:3166. https://doi.org/10.1038/ncomms4166.

[105] Yahyazadehfar M, Ivancik J, Majd H, An B, Zhang D, Arola D. On the Mechanics of Fatigue and Fracture in Teeth. Appl Mech Rev 2014;66. https://doi.org/10.1115/1.4027431.

[106] Yang W, Sherman VR, Gludovatz B, Mackey M, Zimmermann EA, Chang EH, et al. Protective role of Arapaima gigas fish scales: Structure and mechanical behavior. Acta Biomater 2014;10:3599–614. https://doi.org/10.1016/j.actbio.2014.04.009.

[107] Gao K, Guan J, Sun H, Han C, Tan G, Liu Z, et al. Friction and wear behavior of bioinspired composites with nacre-like lamellar and brick-and-mortar architectures against human enamel. J Mater Sci Technol 2022;128:133–41. https://doi.org/10.1016/j.jmst.2022.04.027.

[108] Boccaccini AR. Machinability and brittleness of glass-ceramics. J Mater Process Technol 1997;65:302–4. https://doi.org/10.1016/S0924-0136(96)02275-3.

[109] Barthelat F, Rabiei R. Toughness amplification in natural composites. J Mech Phys Solids 2011;59:829–40. https://doi.org/10.1016/j.jmps.2011.01.001.

[110] Le Ferrand H, Goh BT, Teoh S-H. Nacre-like ceramic composites: Properties, functions and fabrication in the context of dental restorations. Acta Biomater 2024;173:66–79. https://doi.org/10.1016/j.actbio.2023.11.036.

[111] Poloni E, Bouville F, Dreimol CH, Niebel TP, Weber T, Biedermann AR, et al. Tough metal-ceramic composites with multifunctional nacre-like architecture. Sci Rep 2021;11:1621. https://doi.org/10.1038/s41598-021-81068-z.

[112] Kakisawa H, Sumitomo T. The toughening mechanism of nacre and structural materials inspired by nacre. Sci Technol Adv Mater 2011;12:064710. https://doi.org/10.1088/1468-6996/12/6/064710.

[113] Fatehi E, Yazdani Sarvestani H, Ashrafi B, Akbarzadeh AH. Accelerated design of architectured ceramics with tunable thermal resistance via a hybrid machine learning and finite element approach. Mater Des 2021;210:110056. https://doi.org/10.1016/j.matdes.2021.110056.

[114] Katz Z, Yazdani Sarvestani H, Gholipour J, Ashrafi B. Bioinspired Hierarchical Ceramic Sutures for Multi-Modal Performance. Adv Mater Interfaces 2023;10. https://doi.org/10.1002/admi.202300098.

[115] Asgari M, Alderete NA, Lin Z, Benavides R, Espinosa HD. A matter of size? Material, structural and mechanical strategies for size adaptation in the elytra of Cetoniinae beetles. Acta Biomater 2021;122:236–48. https://doi.org/10.1016/j.actbio.2020.12.039.

[116] Yazdani Sarvestani H, Esmail I, Katz Z, Jain S, Sa JH, Backman D, et al. Interlocking design, programmable laser manufacturing and testing for architectured ceramics. Sci Rep 2022;12:17330. https://doi.org/10.1038/s41598-022-22250-9.

[117] Heimann RB. Classic and advanced ceramics: from fundamentals to applications. John Wiley & Sons; 2010.

[118] Pogorelov E, Tushtev K, Arnebold A, Koschek K, Hartwig A, Rezwan K. Strong and super tough: Layered ceramic-polymer composites with bio-inspired morphology. Journal of the American Ceramic Society 2018;101:4732–42. https://doi.org/10.1111/jace.15717.

[119] Harmal A, Khouchani O, El-Korchi T, Tao M, Walker HW. Bioinspired brick-and-mortar geopolymer composites with ultra-high toughness. Cem Concr Compos 2023;137:104944. https://doi.org/10.1016/j.cemconcomp.2023.104944.

[120] Dai H, Dai W, Hu Z, Zhang W, Zhang G, Guo R. Advanced Composites Inspired by Biological Structures and Functions in Nature: Architecture Design, Strengthening Mechanisms, and Mechanical-Functional Responses. Advanced Science 2023;10. https://doi.org/10.1002/advs.202207192.

[121] Esmail I, Yazdani Sarvestani H, Gholipour J, Ashrafi B. Engineered net shaping of alumina ceramics using picosecond laser. Opt Laser Technol 2021;135:106669. https://doi.org/10.1016/j.optlastec.2020.106669.

[122] Amsellem W, Yazdani Sarvestani H, Pankov V, Martinez-Rubi Y, Gholipour J, Ashrafi B. Deep precision machining of SiC ceramics by picosecond laser ablation. Ceram Int 2023;49:9592–606. https://doi.org/10.1016/j.ceramint.2022.11.129.

[123] Behbahani R, Yazdani Sarvestani H, Fatehi E, Kiyani E, Ashrafi B, Karttunen M, et al. Machine learning-driven process of alumina ceramics laser machining. Phys Scr 2023;98:015834. https://doi.org/10.1088/1402-4896/aca3da.

[124] Azad E, Sarvestani HY, Ashrafi B, Shadmehri F, Hojjati M. From Nature to Engineering: Impact of Mortar Volume on Interfacial Properties of Bioinspired Ceramics. n.d.

[125] Ghimire A, Chen PY. Mechanical properties of additively manufactured multi-material stiff-soft interfaces: Guidelines to manufacture complex interface composites with tunable properties. Mater Des 2024;238. https://doi.org/10.1016/j.matdes.2024.112677.

[126] Chan XY, Chua C, Tan S, Le Ferrand H. Energy dissipation in composites with hybrid nacre-like helicoidal microstructures. Compos B Eng 2022;232:109608. https://doi.org/10.1016/j.compositesb.2021.109608.

[127] Andarabi AA, Shelesh-Nezhad K, Chakherlou TN. The effect of laser surface structuring patterns on the interfacial resistance of aluminum joints bonded with epoxy adhesive. Int J Adhes Adhes 2022;114:103101. https://doi.org/10.1016/j.ijadhadh.2022.103101.

[128] Sun F, Penchev P, Pruncu CI, Wang J, Pargeter C, Wang Y, et al. On enhancement of fracture resistance of adhesive joints by surface micropatterning using a femtosecond laser. J Mater Process Technol 2023;315:117904. https://doi.org/10.1016/j.jmatprotec.2023.117904.

[129] Huang B, Sun L, Li L, Zhang L, Lin Y, Che J. Experimental investigation of the strength of polymer-steel direct adhesion (PSDA) joints with micro-structures ablated by laser. J Mater Process Technol 2017;249:407–14. https://doi.org/10.1016/j.jmatprotec.2017.06.031.

[130] Musiari F, Moroni F, Lutey AHA. Enhanced mechanical interlocking of adhesive-bonded joints via tailored serrated patterns manufactured with laser ablation. J Adhes 2025;101:56–90. https://doi.org/10.1080/00218464.2023.2285431.

[131] Hamilton A, Xu Y, Kartal ME, Gadegaard N, Mulvihill DM. Enhancing strength and toughness of adhesive joints via micro-structured mechanical interlocking. Int J Adhes Adhes 2021;105:102775. https://doi.org/10.1016/j.ijadhadh.2020.102775.

[132] Naat N, Boutar Y, Naïmi S, Mezlini S, Da Silva LFM. Effect of surface texture on the mechanical performance of bonded joints: a review. J Adhes 2023;99:166–258. https://doi.org/10.1080/00218464.2021.2008370.

[133] Hosseini MS, Cordisco FA, Zavattieri PD. Analysis of bioinspired non-interlocking geometrically patterned interfaces under predominant mode I loading. J Mech Behav Biomed Mater 2019;96:244–60. https://doi.org/10.1016/j.jmbbm.2019.04.047.

[134] Du F, Alghamdi S, Yang J, Huston D, Tan T. Interfacial Mechanical Behavior in Nacre of Red Abalone and Other Shells: A Review. ACS Biomater Sci Eng 2023;9:3843–59. https://doi.org/10.1021/acsbiomaterials.2c00080.

[135] Yang W, Chen IH, Gludovatz B, Zimmermann EA, Ritchie RO, Meyers MA. Natural flexible dermal armor. Advanced Materials 2013;25:31–48. https://doi.org/10.1002/adma.201202713.

[136] Amini S, Tadayon M, Loke JJ, Kumar A, Kanagavel D, Le Ferrand H, et al. A diecast mineralization process forms the tough mantis shrimp dactyl club. Proceedings of the National Academy of Sciences 2019;116:8685–92. https://doi.org/10.1073/pnas.1816835116.

[137] Yazdani Sarvestani H, Patel J, Shashoua A, Ravanbakhsh H, Taheri S, Gholipour J, et al. Digital precision in engineered ceramics: Tailoring toughness and flexibility through interlocking strategies. J Eur Ceram Soc 2024;44:6000–12. https://doi.org/10.1016/j.jeurceramsoc.2024.03.035.

[138] Yazdani Sarvestani H, Patel J, Azad E, Ashrafi B. Flexible multilayered ceramics: Engineering strength and resilience. Journal of Science: Advanced Materials and Devices 2025;10:100874. https://doi.org/10.1016/j.jsamd.2025.100874.

[139] Xiong X, Wang Z, Zhang Z, Li Q, Shen C, Fan F, et al. Simulation and Experiment on the Low-Velocity Impact Response of Flax Fabric Reinforced Composites. Materials 2023;16:3489. https://doi.org/10.3390/ma16093489.

[140] Naveen J, Jawaid M, Goh KL, Reddy DM, Muthukumar C, Loganathan TM, et al. Advancement in Graphene-Based Materials and Their Nacre Inspired Composites for Armour Applications—A Review. Nanomaterials 2021;11:1239. https://doi.org/10.3390/nano11051239.

[141] Tan G, Zhang J, Zheng L, Jiao D, Liu Z, Zhang Z, et al. Nature-Inspired Nacre-Like Composites Combining Human Tooth-Matching Elasticity and Hardness with Exceptional Damage Tolerance. Advanced Materials 2019;31. https://doi.org/10.1002/adma.201904603.

[142] Chua JQI, Srinivasan DV, Idapalapati S, Miserez A. Fracture toughness of the stomatopod dactyl club is enhanced by plastic dissipation: A fracture micromechanics study. Acta Biomater 2021;126:339–49. https://doi.org/10.1016/j.actbio.2021.03.025.

[143] Natarajan B, Gilman JW. Bioinspired Bouligand cellulose nanocrystal composites: a review of mechanical properties. Philosophical Transactions of the Royal Society A: Mathematical, Physical and Engineering Sciences 2018;376:20170050. https://doi.org/10.1098/rsta.2017.0050.

[144] Chen R, Liu J, Yang C, Weitz DA, He H, Li D, et al. Transparent Impact-Resistant Composite Films with Bioinspired Hierarchical Structure. ACS Appl Mater Interfaces 2019;11:23616–22. https://doi.org/10.1021/acsami.9b06500.

[145] Treccani L. Processing Methods for Advanced Ceramics. Surface-Functionalized Ceramics, Wiley; 2023, p. 47–84. https://doi.org/10.1002/9783527698042.ch2.

[146] Yang G, Tetik H, Weker JN, Xiao X, Lei S, Lin D. *In situ* imaging of three dimensional freeze printing process using rapid x-ray synchrotron radiography. Review of Scientific Instruments 2022;93. https://doi.org/10.1063/5.0077141.

[147] Ma S, Bai W, Xiong D, Shan G, Zhao Z, Yi W, et al. Additive Manufacturing of Micro-Architected Copper based on an Ion-Exchangeable Hydrogel. Angewandte Chemie International Edition 2024;63. https://doi.org/10.1002/anie.202405135.

[148] Wirth DM, Li CC, Pokorski JK, Taylor HK, Shusteff M. Fundamental scaling relationships in additive manufacturing and their implications for future manufacturing and bio-manufacturing systems. Addit Manuf 2024;84:104081. https://doi.org/10.1016/j.addma.2024.104081.

[149] Algharaibeh S, Wan H, Al-Fodeh R, Ireland AJ, Zhang D, Su B. Fabrication and mechanical properties of biomimetic nacre-like ceramic/polymer composites for chairside CAD/CAM dental restorations. Dental Materials 2022;38:121–32. https://doi.org/10.1016/j.dental.2021.10.016.

[150] Yang Y, Li X, Chu M, Sun H, Jin J, Yu K, et al. Electrically assisted 3D printing of nacre-inspired structures with self-sensing capability. Sci Adv 2019;5. https://doi.org/10.1126/sciadv.aau9490.

[151] Liu J, Xu Y, Yang H, Liu Y, Yarlagadda PKDV, Yan C. Investigation of failure mechanisms of nacre at macro and nano scales. J Mech Behav Biomed Mater 2020;112:104018. https://doi.org/10.1016/j.jmbbm.2020.104018.

[152] Woigk W, Poloni E, Grossman M, Bouville F, Masania K, Studart AR. Nacre-like composites with superior specific damping performance. Proceedings of the National Academy of Sciences 2022;119. https://doi.org/10.1073/pnas.2118868119.

[153] Azad E, Sarvestani HY, Ashrafi B, Shadmehri F, Hojjati M. Enhancing Ceramic Structural and Interfacial Properties via Micro-Patterning and Macro-Architectural Integration. n.d.

[154] Shah SZH, Karuppanan S, Megat-Yusoff PSM, Sajid Z. Impact resistance and damage tolerance of fiber reinforced composites: A review. Compos Struct 2019;217:100–21. https://doi.org/10.1016/j.compstruct.2019.03.021.

[155] Evci C, Gülgeç M. Effective damage mechanisms and performance evaluation of ceramic composite armors subjected to impact loading. J Compos Mater 2014;48:3215–36. https://doi.org/10.1177/0021998313508594.

[156] Standard test method for measuring the damage resistance of a fiber-reinforced polymer matrix composite to a drop-weight impact event. ASTM D7136/D7136M West Conshohocken, PA: American Society for Testing and Materials (2015) n.d.

[157] Standard Test Method for High Speed Puncture Properties of Plastics Using Load and Displacement Sensors. 2002: ASTM International n.d.

[158] Barthelat F, Espinosa HD. An Experimental Investigation of Deformation and Fracture of Nacre–Mother of Pearl. Exp Mech 2007;47:311–24. https://doi.org/10.1007/s11340-007-9040-1.

[159] Gao H, Ji B, Jäger IL, Arzt E, Fratzl P. Materials become insensitive to flaws at nanoscale: Lessons from nature. Proceedings of the National Academy of Sciences 2003;100:5597–600. https://doi.org/10.1073/pnas.0631609100.

[160] Katz Z, Yazdani Sarvestani H, Gholipour J, Ashrafi B. Bioinspired Hierarchical Ceramic Sutures for Multi-Modal Performance. Adv Mater Interfaces 2023;10. https://doi.org/10.1002/admi.202300098.

[161] Yazdani Sarvestani H, Lacelle T, Sohrabi-Kashani A, Shashoua A, Karamzadeh V, Ravanbakhsh H, et al. 3D-printed polymer-derived ceramics with tunable cellular architectures. Appl Mater Today 2024;39:102327. https://doi.org/10.1016/j.apmt.2024.102327.